Deep-Water Seismic Bright Spot Reflections in the Southern Canary Basin

Dissertation
zur Erlangung des Doktorgrades
der Mathematisch-Naturwissenschaftlichen Fakultät
der Christian-Albrechts-Universität
zu Kiel

vorgelegt von
Christian Müller

Kiel
2001

Abstract

Fluids are recognized by the pervasive thermal and chemical alteration of rocks deep in the Earth's crust. They are intensively studied for hydrocarbon exploration in sedimentary basins and continental margins to ensure today's and future energy supply. Methane-rich fluids associated with the formation of gas hydrates are supposed to play an important role as a future energy source as well as powerful greenhouse gas and potential environmental hazards. Geophysical evidence of large deep-water fluid reservoirs in the Southern Canary Basin is presented in this thesis. A number of pronounced seismic bright spots in the sedimentary column are interpreted as reflections from the top of these reservoirs based on a combined vertical-incidence and wide-angle reflection seismic study. First indications for large magmatic or hydrocarbon reservoirs in the vicinity of an active volcanic environment at water depths beyond today's exploration frontier are presented.

A dense grid of multichannel seimic (MCS) profiles provide clear structural information. Seismic bright spots are imaged in Middle Miocene-age sediments at 300-800 m below the seafloor. Bright spots show areal extents between 25 and 100 km^2. Strong negative acoustic impedance contrasts, associated with normal incidence reflection coefficients of about -0.4 are calculated from amplitude mapping on single-channel sections and reversed polarity bright spot reflections in prestack MCS shotrecords. Bright spot amplitudes are calibrated at the seafloor reflection coefficient, derived from water column multiples and ODP site 956 southwest of Gran Canaria. The occurence of mud diapirs in the immediate vicinity of the bright spots indicate the presence of overpressured muds and outline vertical gas-charged sediment mobility. The seismic bright spot reflections show continuous high-amplitude and reversed polarity reflections, thus distinguishing them from reflection events related to debris deposits, volcanic basement, and stratigraphic sequences.

MCS surveys approaching deep-water commonly lack sufficient wide-angle reflections. In this study, wide-angle reflections have been imaged on Ocean-Bottom-Hydrophone (OBH) records deployed at the seafloor (3800 m water depth) to constrain the seismic origin of the bright spots. The strong direct water wave, generally masking shallow primary reflections in OBH records, has successfully been suppressed adopting median filter technique, commonly applied in vertical seismic profiling, and thus enabling the application of semblance based velocity analysis. Results provide a velocity-depth model at bright spot locations. The amplitude-versus-offset (AVO) response of the bright spot reflection shows typical features associated with reflections from a layer of reduced acoustic impedance, i.e., absence of a refracted arrival, critical angle and associated phase change. Incidence angles of more than 80° at the target reflector strengthen the interpretation. To quantify the internal properties of the bright spots, full waveform inversion is applied to wide-aperture OBH data. Inversion results yield a bright spot reflection produced by a thin ($\sim$50 m) low-velocity gradient zone with a low P-wave velocity of about 1.0 km/s. The top of the reservoir (seal) is represented by a thin high-velocity layer.

The origin of the prominent bright spots, however, remains unresolved. Circumstantial evidence such as the occurrence of bright spots within the hydrate-stabilty-zone and the existence of large magma volumes in the lower crust and upper mantle, point towards methane and/or carbon dioxide-rich fluids being trapped in the sedimentary sequence.

Zusammenfassung

Die Existenz von Fluiden und Fluidbewegungen innerhalb der Erdkruste kann anhand der thermischen und chemischen Alteration der Gesteine nachgewiesen werden. Fluide werden im Rahmen der Kohlenwasserstoffexploration in sedimentären Becken und an Kontinentalrändern intensiv studiert, um die heutige und zukünftige Energieversorgung zu sichern. Methanhaltigen Fluiden wird im Rahmen der Bildung von Gashydraten eine wichtige Rolle als zukünftige Energiequelle, aber auch als starkes Treibhausgas und damit potentielle Gefahr für die Umwelt, zugeordnet. Geophysikalische Indizien für gigantische Fluidreservoirs im Tiefwasserbereich des südlichen Kanarischen Beckens werden im Rahmen der vorliegenden Arbeit präsentiert. Ausgeprägte seismische Bright Spots in der Sedimentsäule werden als Reflexionen von der Oberkante dieser Reservoirs, auf Basis einer kombinierten steilwinkel- und weitwinkelseismischen Untersuchung, interpretiert. Hierbei könnte es sich um die erste direkte Beobachtung von submarinen magmatischen Fluidlagerstätten oder klassischen Kohlenwasserstofflagerstätten im Bereich vulkanischer Inseln jenseits heutiger Erkundungstiefen handeln.

Untergrundstrukturen wurden auf einem dichten Netz mehrkanaliger reflexionsseismischer Profile kartiert. Die seismischen Bright Spots wurden dabei in sedimentären Formationen, die dem mittleren Miozän zugeordnet werden, in 300 bis 800 m unterhalb des Meeresbodens, abgebildet. Die Bright Spots zeigen dabei flächenhafte Ausdehnungen zwischen 25 und 100 km^2. Negative akustische Impedanzkontraste mit Reflexionskoeffizienten von bis zu -0.4 sind anhand von Kartierungen der seismischen Amplitude in Einkanal-Sektionen und aus der Phasenumkehr der Bright Spot Reflexion in den Mehrkanalregistrierungen belegt. Die Amplituden wurden an dem Reflexionskoeffizienten des Meeresbodens kalibriert, der aus der ersten Wassermultiplen und aus Geschwindigkeits- und Dichtelogs der ODP-Bohrung 956, südwestlich von Gran Canaria, bestimmt wurde. Das Auftreten von Diapiren in unmittelbarer Nähe zu den Bright Spots deutet ebenfalls auf gasgesättigte Sedimente und vertikale Sedimentmobilität hin. Die seismischen Bright Spots in den Sektionen zeigen Stetigkeit in den hohen Amplituden und der Phasenumkehr, was sie deutlich zu vulkaniklastischen Ablagerungen, dem vulkanischen Basement und stratigraphischen Sequenzen, abgrenzt.

Die seismische Weitwinkelreflexionsantwort liefert über die Scherwellengeschwindigkeit ein weiteres Indiz zum Nachweis negativer Impedanzkontraste. Genügend große Einfallswinkel wurden hier mit Hilfe von am Meeresboden abgesetzten Ozean-Boden-Hydrophonen aufgezeichnet, um den akustischen Impedanzkontrast als auch das Poisson-Verhältnis an den Bright Spot Reflexionen weiter einzugrenzen. Die starke direkte Wasserwelle, die in den OBH-Sektionen oft die Reflexionen von meeresbodennahen Horizonten überprägt, konnte erfolgreich durch die Anpassung eines aus der Bohrlochgeophysik bekannten Verfahrens unterdrückt werden. Dadurch wurde eine Stapelgeschwindigkeitsanalyse ermöglicht. Die Ergebnisse liefern eine lokale P-wellengeschwindigkeitsfunktion im Bereich der Bright Spots. Die Untersuchung der Amplitudenvariation mit dem Einfallswinkel zeigt deutliche Merkmale, die typischerweise mit einer Zone erniedrigter Impedanz assoziiert sind, wie das Fehlen einer refraktierten Welle, eines

kritschen Winkels und entsprechender Phasenveränderung oberhalb dieses Winkels. Einfallswinkel von mehr als 80° an den Bright Spot Horizonten erlauben diesbezüglich gesicherte Aussagen. Die Geschwindigkeitsfeinstruktur der Bright Spot Reflexionen wurde durch Anwendung seismischer Inversionsmethoden auf OBH-Weitwinkeldaten untersucht. Das daraus hervorgegangene Untergrundmodel besteht aus einer etwa 50 m mächtigen Gradientenschicht mit P-Wellengeschwindigkeiten von etwa 1.0 km/s. Die Oberkante des Reservoirs zeichnet sich als dünne Schicht erhöhter P-Wellengeschwindigkeit ab.

Eine eindeutige Klassifizierung bezüglich der Herkunft der Fluide kann auf der Basis der vorliegenden geophysikalischen Studie nicht vorgenommen werden. Die Lage der Bright Spots innerhalb des Stabilitätsbereichs von Gashydraten und die Existenz riesiger Magmavolumen in der unteren ozeanischen Kruste und im oberen Erdmantel lassen auf methan- oder kohlendioxidreiche Fluide in den sedimentären Formationen des südlichen Kanarischen Beckens schließen.

Contents

Chapter 1

Introduction

Fluids play an important role in the interaction of transport processes in and between the Earth's lithosphere, hydrosphere, and atmosphere. The direct detection of fluids in the Earth's igneous crust and overlying sedimentary sequences, along with providing structural information, has been a long-standing goal of subsurface imaging using geophysical and particularly reflection seimic methods. Fluids directly affect petrophysical parameters. For example, the lowering of the acoustic impedance against embedding sequences produces strong seismic reflection amplitudes. These amplitudes often exceed those emerging from lithologic boundaries, e.g., in sedimentary rocks. A wide range of confirmed and potential fluid accumulations in the subsurface of various origin, commonly associated with pronounced reflection seismic anomalies, have been studied.

Strong reflection events in Precambrian crystalline rocks were observed on deep seismic reflection lines from the Siljan Ring area, a Devonian meteorite impact crater in central Sweden (Juhlin, 1990). Cracks and fissures have been imaged in the sections, that would allow fluids to migrate upwards, along with a series of dense layers providing potential cap rocks. The almost complete absence of sedimentary rocks suggests at least in part abiogenic origin of these fluids, probably from the Earth's mantle, as suggested by Gold (1999). Nonetheless, drilling of this structure only provided traces of natural gas (methane) and minor amounts of oil, not enough to make it a commercial venture.

Within the framework of COCORP (Consortium for Continental Reflection Profiling) a number of anomalously strong reflectors, typically near-horizontal and at depths of about 20 km in the continental crust, have been imaged on reflection seismic profiles (Oliver, 1990). Geological and geophysical data proposed mid-crustal magma bodies and/or fluids associated with reflectors in the crust beneath the Rio Grande Rift, New Mexico and Death Valley, California. The nature of these fluids are uncertain at present. In this context, fluids expelled tectonically from sediments buried in orogenic belts and migrating into rocks of adjacent parts of the continental crust are discussed. Rapid dewatering of underthrust sediments has been studied beneath the deformed frontal sedimentary wedge at the Costa Rica subduction complex, which is associated with fluids of seawater geochemistry moving along the decollement. Origin of these fluids at maximum depths between 10 and 15 km, and distances of 40-60 km landward of the trench have been proposed (Silver *et al.*, 2000).

Fluids also play an important role in the vicinity of intraplate active volcanic environments. Transportion systems of magma and associated fluids have been studied at Kilauea volcano, located on the south-eastern shield of Mauna Loa, Hawaii. During upward transportation of magma from depths of ~ 40 km, CO_2-rich fluids, probably the most important volatiles in the magma according to quantity, are primarily separated from the parental magma, and subsequently stored or discharged in the summit region and adjacent rifts (Gerlach & Graeber, 1985). Similar observations of strong CO_2-degassing have been made in the region of the Eifel volcanism (Schmincke, 1986). Particularly, the storage of these fluids in the subsurface, and hence not accessible for direct observation, might bias the estimation of the overall volatile budget. However, no relevant reflection seismic observations of magmatic gas reservoirs have yet been presented.

In contrast, strong seismic reflections, generally characterized by negative polarity, have been observed in polar regions associated with permafrost, and in sediments of outer continental margins. These reflections, appearing as anomalous bottom simulating reflections (BSR), coincide with the base of the gas hydrate stability zone (Shipley et al., 1979). Gas hydrates have gained increasing interest in recent years because of their potential as a fossil fuel resource, their role as a submarine geohazard, and their effects on global climate change (Kvenvolden, 1993). Enormous amounts of methane are required for gas hydrate formation, which is supposed to be generated microbially at depths below the hydrate stability zone. Subsequently, gas hydrates are generated through the removal of methane from rising fluids (Hyndman & Davis, 1992). The presence of small amounts of free gas beneath the hydrate stability zone has been sucessfully verified during ODP Leg 146 and 164 (Mackay et al., 1994; Dickens et al., 1997). Additionally, stacking velocity analysis (Andreassen et al., 1990) and waveform inversion (Singh, 1993; Singh & Minshull, 1994) of reflection seismic data verified a pronounced reduction of compressional wave velocity indicating the presence of free gas.

The direct detection of hydrocarbon oil and gas reservoirs in Tertiary sedimentary basins using reflection seismic techniques have been established in the exploration industry in the late sixties (Khattri et al., 1979). In the early stages of exploration, the detection of amplitude anomalies, commonly called bright spots, in the seismic sections was used as the sole qualitative tool for identifying hydrocarbon reservoirs (Sengbush, 1983). The oil boom in the seventies and early eighties led to the development of further characteristics of the reflection response from reservoirs, e.g., polarity reversal, shadow zones, and time sag anomalies (Sheriff, 1974). More sophisticated techniques routinely used today are based on acquisition of wide-aperture reflections from the reservoirs using long hydrophone streamers in marine surveys. This method enables the extraction of further petrophysical properties of the potential reservoirs such as Poisson's ratio to better estimate the reservoir's commercial value. Numerous examples of bright spots associated with gas reservoirs in the Gulf of Mexico outer continental shelf (Fig. 1.1, top) have been presented in literature (Sengbush, 1983; Sheriff & Geldart, 1982). Recently, hydrocarbon exploration and production are moving towards increasing water depths, where seismic acquisition techniques hardly provide sufficient source-receiver offsets, and thus increase ambiguity in interpretation.
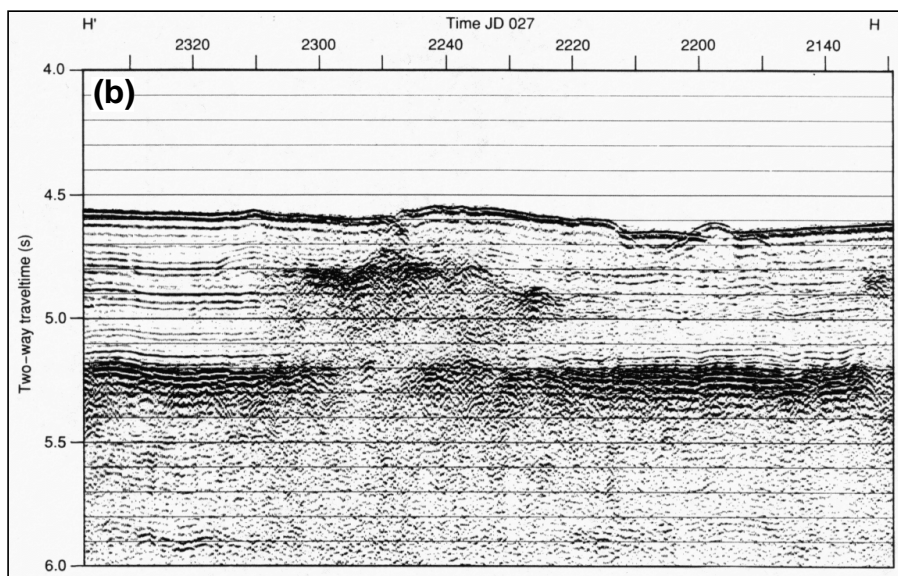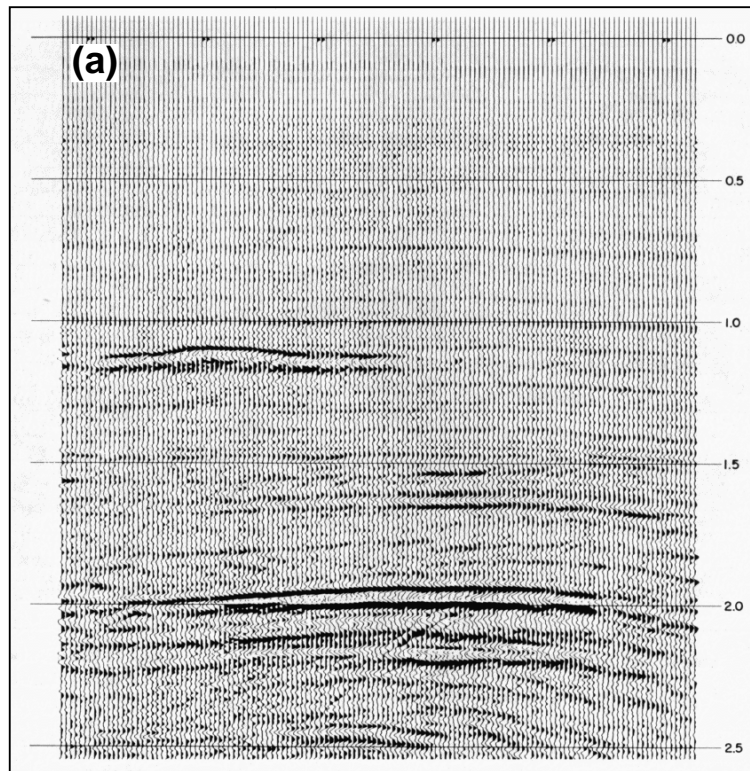
Figure 1.1: *Pronounced seismic reflectors in marine sediments can have various origins. (a) bright spot reflection from a Gulf of Mexico gas-reservoir (Sengbush, 1983). (b) basaltic sill in the Nauru Basin of the west Pacific (Hagen, 1991).*

Nevertheless, the bright spot method in exploration was found to have limitations in that factors other than gas can cause bright reflections. Dry holes drilled into bright spots found igneous intrusions, carbonate or hard streaks, lignites, or wet sands. An example of a bright reflection anomaly associated with a basaltic sill in the west Pacific is given in Fig. 1.1 (bottom).

In the deep-water Southern Canary Basin a number of pronounced seismic bright spots have been imaged on steep-angle reflection and wide-angle reflection and refraction seimic sections during two cruises of R/V *Poseidon* in 1997 and 1999. No evidence for gas reservoirs in the sedimentary basins adjacent to the Canary Islands has yet been reported in literature. The aim of this thesis is to determine the seismic origin of these bright spots. In order to address the question, whether these reflection anomalies originate from positive or negative acoustic impedance contrasts, and possibly indicate enormous deep-water gas reservoirs of biogenic or magmatic origin, several geophysical processing and interpretation techniques have been applied.

The geological setting of the Canary Islands with emphasis on the survey area in the Southern Canary Basin is described in Chapter Two, followed by specification of the available reflection seismic data material and presentation of the methods applied to these data in Chapter Three and Four. 2-D reflection seismic lines are processed preserving true relative amplitudes in order to image the bright spots and their distribution in the Southern Canary Basin. A dense grid of 2-D seismic lines at two bright spot locations provides an image of the areal extent of these structures in Chapter Five. Detailed investigations of pre-stack MCS shotrecords focusing on the phase of the bright spot reflection and mapping of the inline amplitude variation of the bright spot reflection on near-trace sections emphasize the bright spot reflection strength in Chapter Six. A new technique for suppression of the bubble pulse sequence in OBH records is proposed in order to enhance shallow sedimentary reflections. Subsequently, semblance based velocity analysis has been carried out. Finally, results are presented from amplitude-versus-offset analysis and full waveform inversion applied to wide-aperture ocean-bottom-hydrophone data.

Chapter 2

Geological Setting

The Canarian Archipelago located off the Northwest African continental margin consists of seven major islands: Lanzarote and Fuerteventura to the east, Gran Canaria, Tenerife and La Gomera in the center and La Palma and El Hierro in the west (Fig. 2.1). The archipelago is underlain by several presently active melting areas and extends between 115 and 600 km west of the African coast and 100-200 km from north to south. The island chain is flanked by two basins, one north of the chain and one south.

2.1   The Canary Mantle Plume

In his paper on the origin of the Hawaiian Islands, Wilson (1963) proposed that the Canary Islands were formed by an upwelling mantle plume. The hot mantle rises owing to its low density and therefore increased buoyancy. The surface expression of a mantle plume is the hot spot, usually characterised by high heat-flow, intense volcanic activity and a broad crustal and topographic swell (Charvis & Danobeitia, 1999). However, the Canary Islands show several features which are inconsistent with the classic mantle plume model developed for Hawaii, e.g., a long subaerial volcanic history of the Canary island chain and individual islands (e.g., about 20 Ma on the islands of Fuerteventura and Lanzarote), multiple cycles of volcanism, and the absence of a broad topographic swell, which is observed as clear seafloor elevation at the Hawaiian Islands and the Cape Verde Islands (Hoernle & Schmincke, 1993; Schmincke, 1998). Hoernle & Schmincke (1993) proposed a 'blob-model', where decompression melting of discrete blobs of plume material explain the multi-cycle evolution of the Canary volcanoes. Canales and Danobeitia (1998) observed a noticable depth anomaly in the basement west of the Canaries and concluded from coherence analysis of bathymetry and gravity data, that the swell might be masked by a thick sedimentary cover and the influence of the Canarian volcanism. Ranero et al. (1995) estimated the magnitude of a topographic swell and lithospheric thinning in the oceanic basin west of the Canary Islands based on gravity modelling and deep reflection seismic data. A lithospheric uplift of about 20 km beneath the Canarian Archipelago was suggested to explain observed gravity anomalies. Furthermore, low spreading rates of about 10 mm/y for the last 60 million years (Minster & Jordan, 1978) can contribute to the longlived history of individual volcanoes.
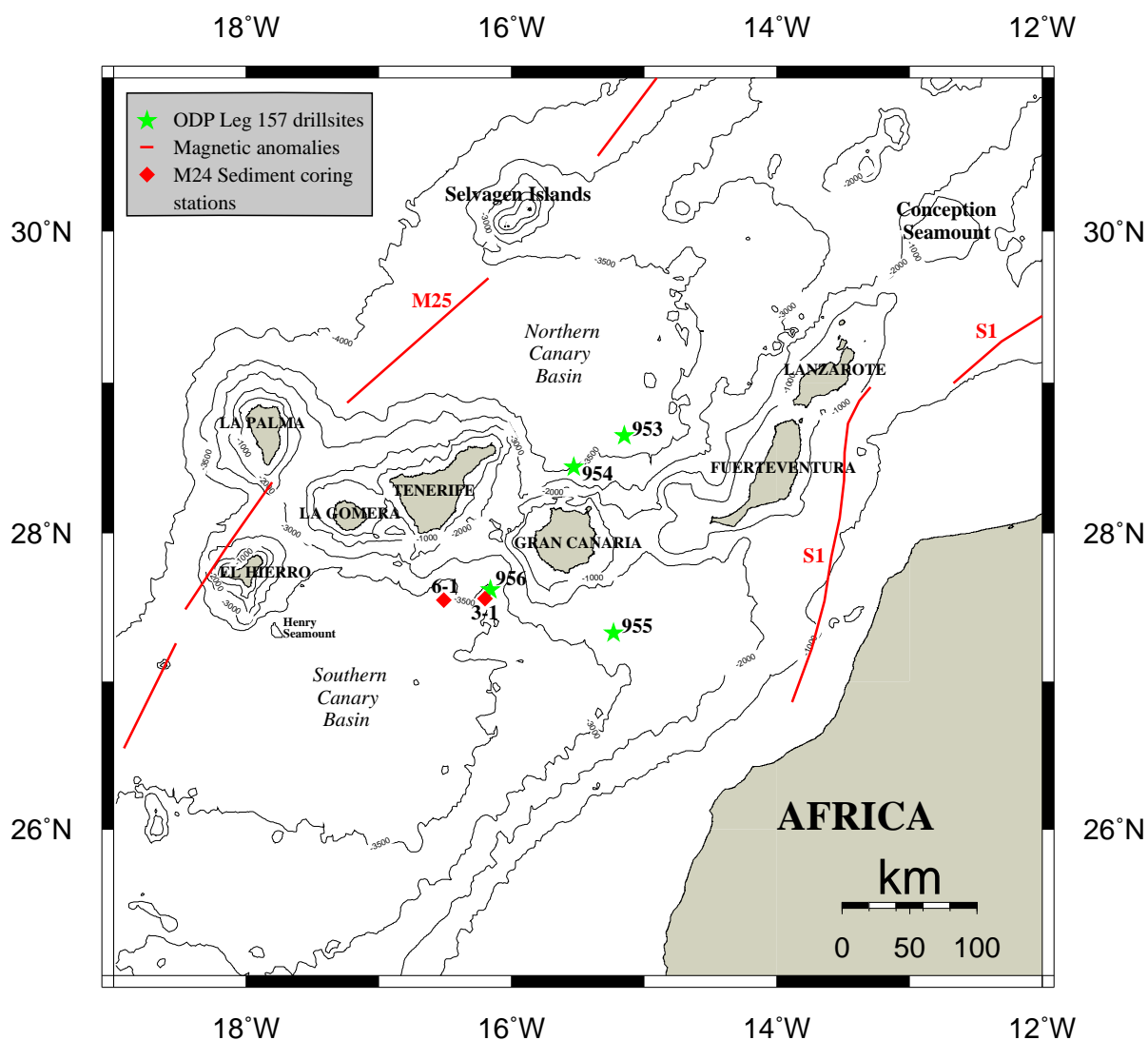
Figure 2.1: *Location map of the Canarian Archipelago off the northwest African continental margin, plotted together with bathymetry and magnetic anomalies M25 (156 Ma) after Klitgord and Schouten (1986), and S1 (175 Ma) after Roeser (1982). ODP-Leg 157 drillsites are plotted after Schmincke et al. (1995) and sediment sampling stations from METEOR Cruise M24-4 (Schmincke & Rihm, 1994).*

2.2 Mesozoic oceanic crust

The occurence of MORB fragments on Lanzarote provide definite evidence that oceanic crust beneath the Canarian Archipelago continues at least as far east as the eastern Canary Islands. Age-dating confirms a Jurassic age for the oceanic crust in this region (Schmincke *et al.*, 1998). There is present consensus that the boundary between oceanic and continental crust is situated east of the Canary Ridge, seaward of a zone of salt diapirs that parallels the African coast (Wissmann, 1979; Hinz *et al.*, 1982). This boundary coincides with magnetic anomaly S1 (Fig. 2.1) about halfway between

Fuerteventura and Africa (Roeser, 1982), which is interpreted as true oceanic with an age of 175 Ma (Roest *et al.*, 1992; Klitgord & Schouten, 1986). The Jurassic magnetic quiet zone extends throughout the Canarian Archipelago until anomaly M25 (156 Ma) at the westernmost islands of El Hierro and La Palma.

The most recent and detailed seismic data indicate that the base of the oceanic crust is at about 15-16 km beneath Gran Canaria. The igneous oceanic crust in the northern and southern Canary Basin is about 7 km thick, showing only little variation on reflection seismic profiles (Ye *et al.*, 1999; Ranero *et al.*, 1995). The thickness of the lithosphere in the vicinity of the Canary Islands may be around 100 km (Schmincke *et al.*, 1995).

2.3   The Canary Islands

The structure of the Canary Islands as well as most intraplate oceanic islands is divided into a subaerial part whose volume generally is less than 5% of the total volume, and a submarine part with an intrusive core and the volcanic apron (Schmincke, 1998). The Canaries show a general, but slightly diffuse westward age progression of the shield phase. Individual islands in the Canarian Archipelago, as well as islands in the Hawaiian Archipelago, show two main stages of growth, separated by periods of eruptive gaps. Accordingly, they are separated into three groups: (1) the islands of Fuerteventura, Lanzarote, and Gran Canaria, at present in the post-erosional stage of development, (2) the island of La Gomera, in the repose (gap) stage, and (3) the islands of Tenerife, La Palma and El Hierro, in the shield stage of growth (Carracedo, 1994). The well-studied volcanic edifice of Gran Canaria is generally characterized by high P-wave velocities exceeding 6 km/s and a heterogeneous structure with large velocity variations. The massive volcanic island flank, thinning away from the central edifice, can be correlated 30 to 60 km offshore. Large landslides imaged on seismic, bathymetric and drilling data significantly contribute to the destruction of the island and the growth of the submarine volcanic apron (Funk & Schmincke, 1998). The island flank of Gran Canaria is covered by volcaniclastic and hemipelagic sediments of up to 1 km thickness and is underlain by ~3 km prevolcanic Neogene-Jurassic sediments, estimated from tomographic inversion (Krastel, 1999). Emergence of the Canary Islands and especially Gran Canaria caused a significant flexural deformation of the lithosphere, observed and modelled from gravity anomalies (Weddeling, 1996).

2.4   Sedimentary basins

The Northern and Southern Canary Basin developed during the emergence of the island chain. The northern basin is bound to the east by the north-northeast striking Canary Ridge which consists of the Miocene islands of Fuerteventura and Lanzarote and Conception Seamount at its northeastern continuation. To the north, the basin is bound between Selvagen Islands and Conception Seamount by submarine ridges and seamounts. The basin is open to the west. The depth of the northern basin ranges from about 3000 m in the northeast to about 4000 m north of La Palma and steepens rapidly to 4600 m west of La Palma and then more gently to the Madeira Abyssal

Plain (5300 m) 1000 km to the west (Schmincke *et al.*, 1995). The southern basin is flanked to the east and southeast by the African continental margin. It deepens from about 2000 m south of Fuerteventura to 3800 m south of El Hierro and is open to the west as well.

There is a pronounced difference in volcanic and nonvolcanic sedimentation between the two basins. The long East Canary Ridge forms a major morphological barrier, so that the sediment supply from Africa was and is almost completely restricted to the apron south of the islands and the southern basin. Sediments in the southern basin are more enriched in organic matter than average deep-sea sediments due to a strong contribution of marine organic matter caused by upwelling along the southeastern coast of Tenerife. Furthermore, hemipelagic and turbiditic sediments drilled in the southern basin indicate a significant contribution of sediments from the African continental margin. Organic-rich sediments are almost absent in the Northern Canary Basin, which is dominated by pelagic sedimentation and volcaniclastic sediment deposits from the islands (Schmincke & Sumita, 1998).

2.5   Results from ODP-Leg 157

The Volcanic Island Clastic Apron Project (VICAP, ODP-Leg 157) was designed to monitor the submarine and subaerial temporal, compositional, volcanic, and chemical growth and mass wasting evolution of a well studied ocean island system by drilling through its peripheral clastic apron and through the edge of the submarine shield phase deposits. Gran Canaria was chosen because it has a very long history with magmas of greatly contrasting compositions and because the temporal, volcanic, and compositional evolution of this island has been studied in detail (Schmincke *et al.*, 1995). Because of significant differences in the geologic history of the northern and southern Gran Canaria (Schmincke, 1998), two drilling sites (Sites 953 and 954) were placed on the volcanic apron in the northern basin and two sites (Site 955 and 956) on the apron in the southern basin.

The main pre-site survey for the VICAP-part of ODP-Leg 157 was conducted during Meteor Cruise M24 (Schmincke & Rihm, 1994). The extension of the submarine flanks of Gran Canaria were mapped on high-resolution reflection seismic profiles, and it was found that the edges of the flank of Gran Canaria extends 30 to 60 km away from the shoreline. Meteor Cruise M16-4 (Wefer *et al.*, 1992) completed the M24 data set with reflection seismic lines south of Gran Canaria and Tenerife. Some of the proposed VICAP drillsites were additionally surveyed during Charles Darwin Cruise 82 (Watts *et al.*, 1993). During the VICAP-Cruise, a single reflection seismic profile ($\sim$18 km) was acquired at Site 956 to supplement the existing profiles. The lateral extent and termination of sequences down to the acoustic basement at $\sim$1 s TWT are well resolved.

Detailed scientific drilling results are described in Schmincke et al. (1995) and Schmincke and Sumita (1998). Because of the proximity of Site 956 to the survey area of this study, the main results from this site are briefly repeated here.

2.5.1 Site 956

ODP Site 956, located on the southern volcanic apron of Gran Canaria in the Southern Canary Basin, 60 km southwest of Gran Canaria, was drilled at a water depth of 3453 mbsl. Drilling penetrated 704 m of sediments and sedimentary rocks, where ages range from Holocene to Middle Miocene. Sedimentation was influenced by major volcanic events such as (1) large explosive eruptions that resulted in widespread ash flows and ash falls, (2) the basaltic shield phase of Gran Canaria, and (3) Pleistocene tephra layers from Tenerife. Hence, sediment supply from three sources apart from background sedimentation has been identified at Site 956: The African continental margin, Gran Canaria, and Tenerife.

The supply of volcaniclastic material by sediment gravity flows (i.e., debris flows and turbidites) and fallout from both Gran Canaria and Tenerife have played a fundamental role in determining the lithostratigraphy of Site 956. The sedimentary succession has therefore been subdivided into five lithostratigraphic units based mainly on the abundance and composition of volcaniclastic deposits that correspond broadly in time and composition to the Miocene magmatic phases of Gran Canaria and Pleistocene volcanism on Tenerife. Fig. 2.2 shows the lithologic summary with the main lithologic units identified by age.

The oldest sedimentary sequence (Unit V) recovered at Site 956 is of Middle Miocene age and consists of basaltic breccia and hyaloclastite tuff, which mark the beginning of the voluminous Mogan stage ($\sim$14 Ma) of explosive volcanism on Gran Canaria. This material was primarily deposited as debris flows. The $\sim$130 m thick sequence is characterized by high P-wave velocities up to 5 km/s, densities about 2.5 g/cm^3, and porosities about 30% (Fig. 2.3). In seismic sections, this sequence downlaps onto the acoustic basement about four kilometers seaward from this site. Above this sequence (Subunit IVa, IVb), a more trachyphonlithic composition of volcaniclastic material is correlated with the transition from Mogan Group to Fataga Group volcanism, which occured at $\sim$13 Ma on Gran Canaria. These sediments were also deposited as debris flows. This $\sim$200 m thick sequence is characterized by a decrease in P-wave velocities to about 2.0 km/s, densities about 2.0 g/cm^3, and increased porosities of about 50 %. This unit downlaps onto Unit V two kilometers east of Site 956. The 170 m thick Unit III correlates with the abruptly diminished influx of volcaniclastic material at the end of the Fataga Group volcanism ($\sim$9.5 Ma). During this period, sedimentation was dominantly pelagic; in the early part of this period mostly nannofossil mixed sediments changing to nannofossil ooze with time. Therefore, this sequence is especially important for seismostratigraphic interpretations of sedimentary structures in the Southern Canary Basin, and logging parameters provide a foundation for seismic modelling. P-wave velocities increase from about 1.7 km/s at the top of this sequence to 2.0 km/s at the base, density increases from about 1.8 to 2.0 g/cm^3, and porosities increase to 60 % towards the top of this sequence. Recovery of the 40 m thick Unit II was poor. The influx of coarse tuffs and lapillistones coincides with the Roque Nublo phase of volcanism (4.5-3.7 Ma) on Gran Canaria. This sequence is assumed to be deposited as slump debris from collapsed flanks rather than volcanic activity. Due to high P-wave velocities of more than 4.0 km/s and densities about 2.3 g/cm^3, this unit marks a very prominent marker horizon (high acoustic impedance) in seismic sections, which can be
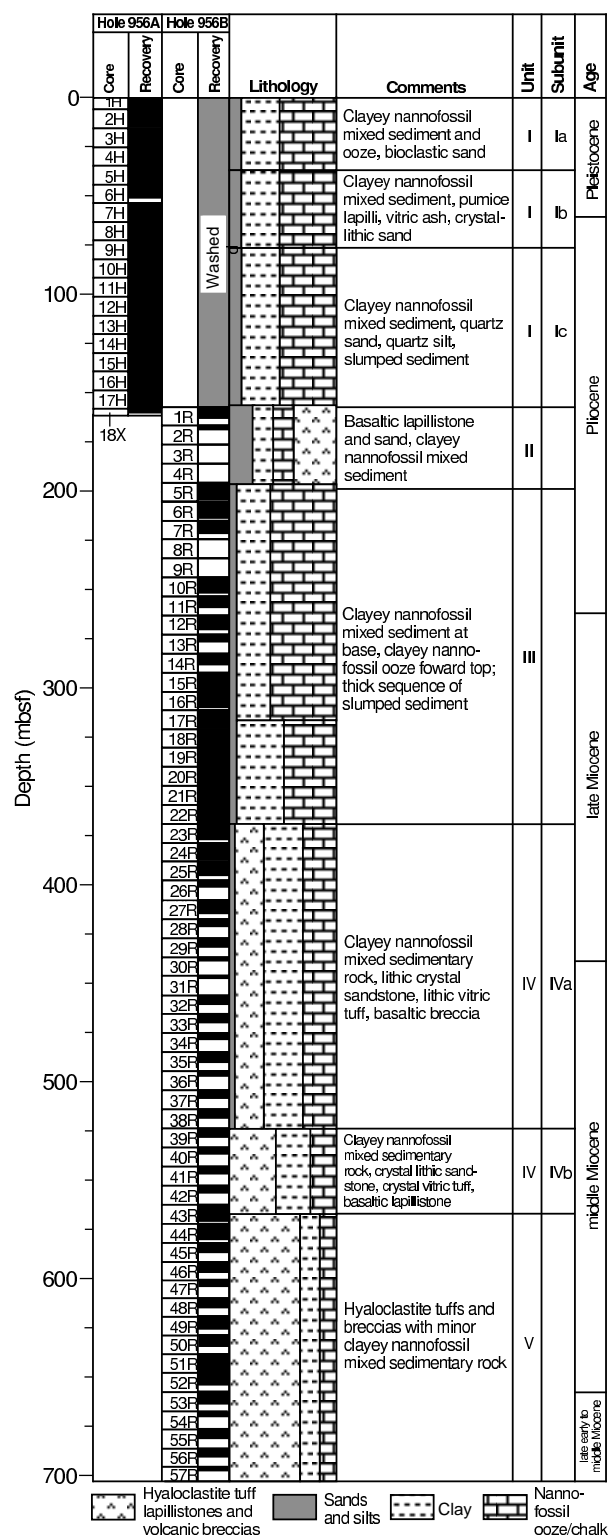
Figure 2.2: *Lithologic summary of ODP site 956 showing the main lithologic units identified with age and a generalized graphic lithology (Schmincke et al., 1995). Site 956 is located on the submarine apron of Gran Canaria in the Southern Canary Basin.*
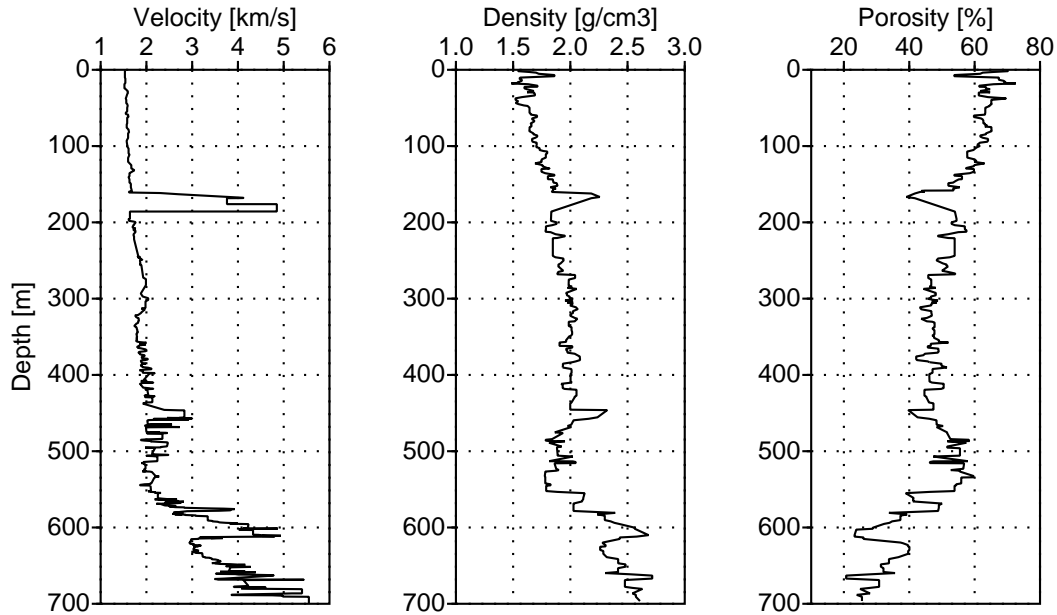
Figure 2.3: *P-wave velocity measured on cores from Site 956 by DSV and Hamilton Frame method (left), densities (center) and porosities (right) are calculated from measurements of weight and volume of sediment and rock samples (Schmincke et al., 1995). A 3-point median filter has been applied to suppress extreme values.*

traced far into the southern basin. Unit I is 158 m thick. The subdivision into three lithologic subunits is based on differences in minor sand lithologies and the occurence of specific volcanic components. The dominant lithology is clayey nannofossil mixed sediment. The abundance of thin ash layers and lapilli is interpreted as debris flow deposits from Tenerife. This unit shows only weak reflectivity in seismic sections due to small acoustic impedance contrasts.

2.6 Hydrocarbon system

An Upper Triassic/Lower Jurrassic salt basin developed during the syn-rift period of initial rifting in the Central Atlantic region. The salt filled topographic lows between pre-Mesozoic basement highs, resulting in an uneven original distribution. The progressive deformation of the vast amount of salt during the Late Cretaceous/Tertiary period created major structural hydrocarbon traps. The seaward extent of salt diapirs, folds, and salt tongues are bound by magnetic anomaly S1 (Hinz *et al.*, 1982). Presently, an active petroleum system is well established onshore Morroco, while recent exploration efforts concentrate on the shelfal region and several blocks were licensed in the last few years covering large offshore acreage in water depths to almost 3000 m (Tari *et al.*, 2000).

Chapter 3

Reflection Seismic Data

Reflection seismic data analyzed in this study have been acquired on two cruises of the German R/V *Poseidon* in the Southern Canary Basin. In the scope of the investigation of submarine landslides on the flanks of the Canary Islands during R/V *Poseidon* cruise 236 (Theilen & Riedel, 1997), a number of pronounced seismic bright spots have been imaged in the sedimentary column on steep-angle reconnaissance line 28/97 (Fig. 3.1, Fig. 3.2). In order to provide wide-aperture reflections and to map the areal extent and regional distribution of these bright spots, two locations have been selected for detailed investigation by simultaneous application of MCS and OBH technique on R/V *Poseidon* cruise 251 (Theilen & Müller, 1999). Wide-angle data, recorded on five OBHs from Geomar Kiel (Flueh & Bialas, 1996), provide coverage of both refracted and reflected arrivals originating at the acoustic basement and above. 15 OBH stations are indicated in Fig. 3.1. OBH 01 through 05 were deployed from north to south across the bright spot structure south of El Hierro island. 10 OBH stations are located at the bright spot southwest of El Hierro island, where OBH 06 through 10 were deployed from northeast to southwest and OBH 11 through 15 were deployed from west to east. Details on acquisition parameters and seismic equipment are given in table 3.1. An MCS amplitude spectrum is shown in Fig. 3.3.

Table 3.1: Acquisition parameters

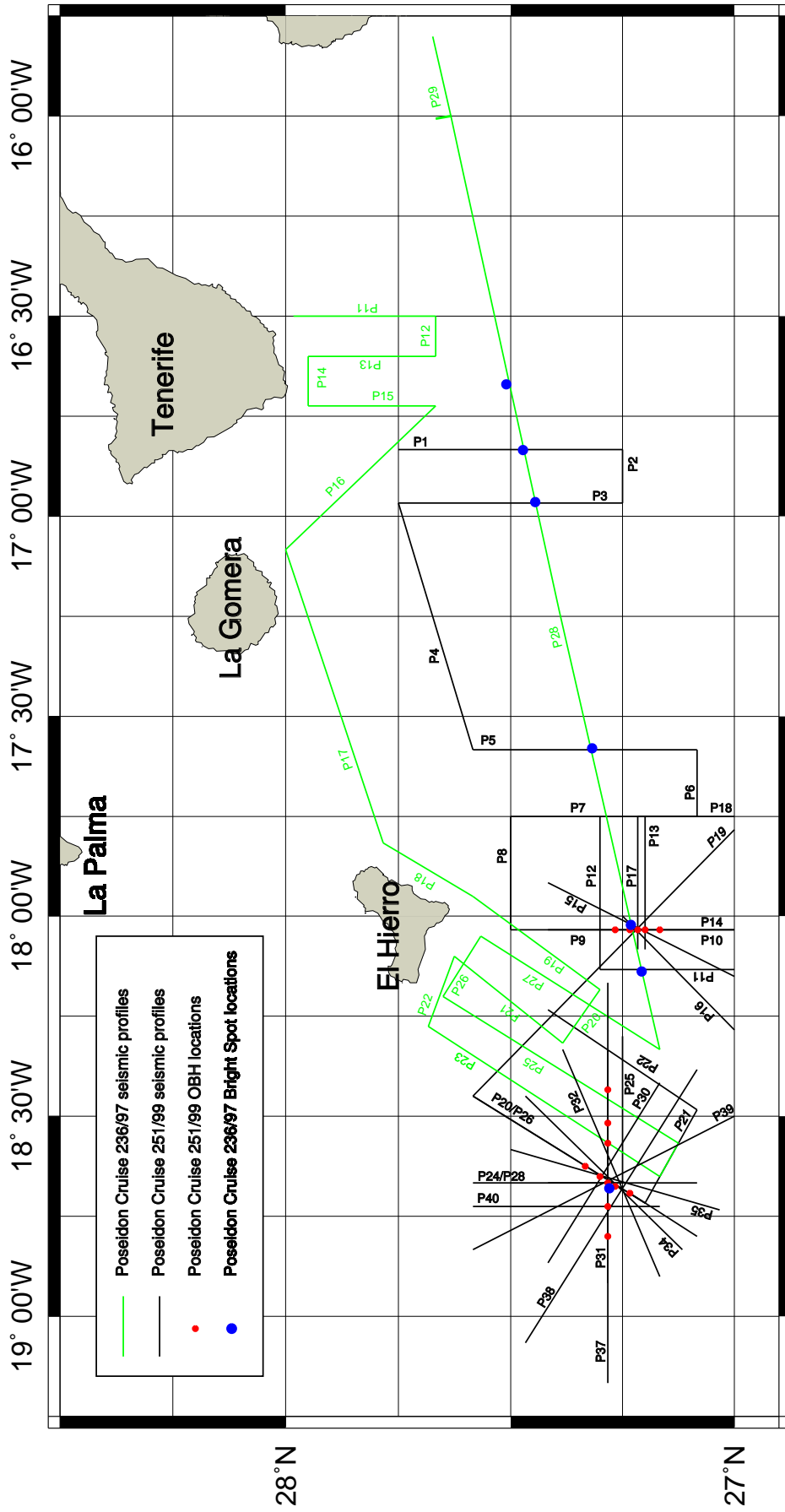|	
Acoustic source:	2.0l, 0.8l, 0.6l and 0.33l (VLF, Prakla-Seismos) two-element airgun array 6 m towing depth
Streamer:	24 channel hydrophone streamer (AMG) 600 m active length 230 m lead in cable 6 m towing depth
Recording system:	Geometrics Strataview R60 1 ms sample interval & 5 sec record length Geomar OBH 5 ms sample interval & 10 s/20 s record length

Figure 3.1: *Location map of the survey area showing reflection seismic profiles acquired on R/V Poseidon cruise 251 (black lines) and 236 (green lines). Locations of seismic bright spots imaged on cruise 236 are marked with blue dots and OBH stations on cruise 251 are marked with red dots.*
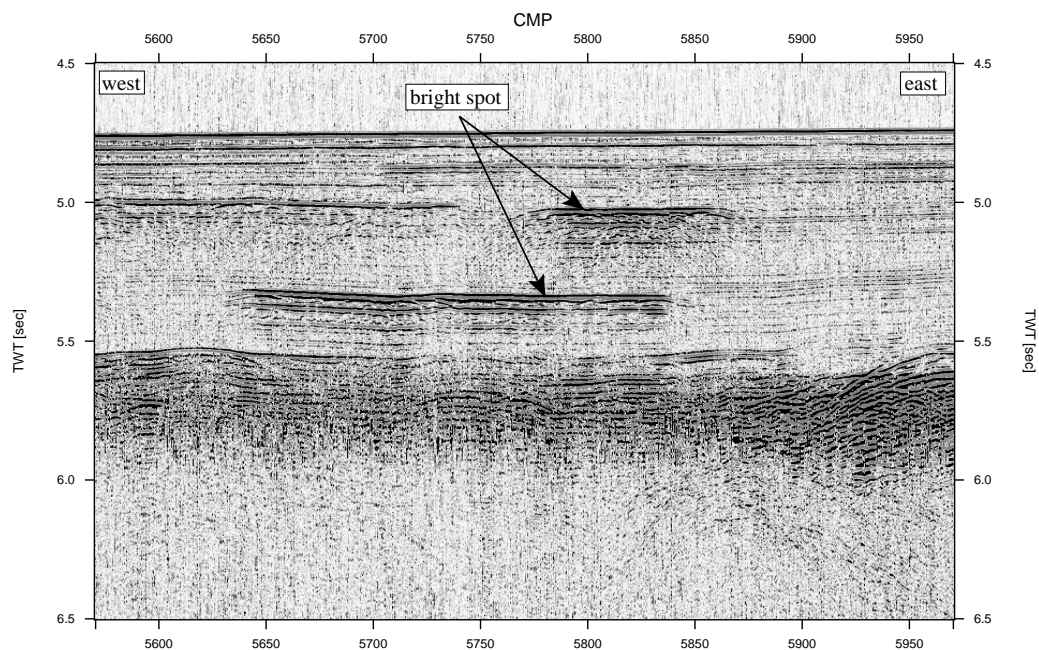
Figure 3.2: *Brute stack showing two bright spots on line 28/97, south of Tenerife (V.E. = 4).*
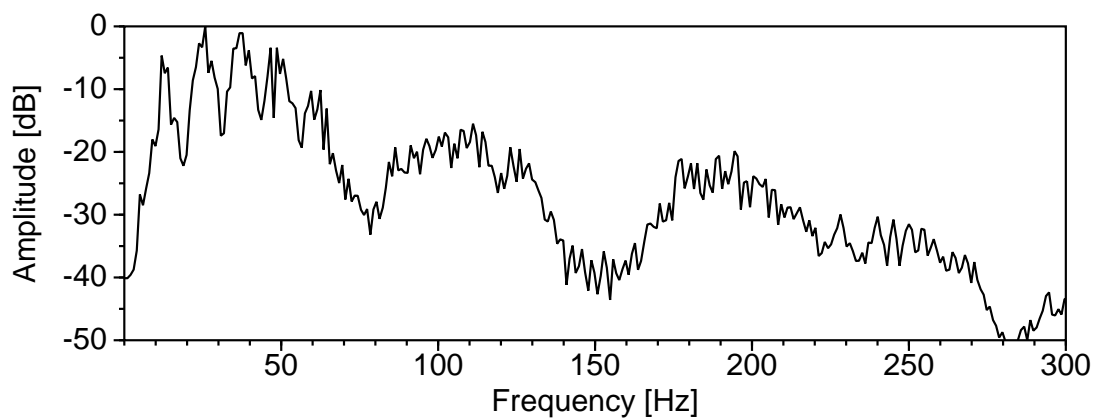

Figure 3.3: *Amplitude spectrum calculated from MCS shotrecord 560, line 17/99.*

Chapter 4

Methods

In order to analyze the seismic origin of the observed bright spot reflections, various methods and techniques were applied to the available data, including standard reflection seismic processing sequences, amplitude-versus-offset analysis, and waveform inversion. Additionally, traditional techniques have been adapted to new fields of application. Procedure and theoretical background of these methods is briefly described in this section.

4.1   Acquisition and processing geometry

The application of airguns with multichannel hydrophone streamer and ocean-bottom-hydrophones employs two complementary acquisition techniques to obtain structural information from stacked seismic sections and subsurface P-wave velocity information from wide-aperture OBH data. Fig. 4.1(left) illustrates acquisition geometry accompanied by these methods for MCS (left) and OBH (right) surveys. Note that the direct water wave in MCS geometry has a noticeably shorter travelpath than the primary reflections, assuming significantly larger water depth than the length of the receiver array. In contrast, the length of the travelpath of the direct water wave in OBH geometry is similar to that for shallow reflections from immediately below the seafloor. Therefore, shallow sedimentary reflections are usually masked by the high-amplitude direct water wave in OBH records necessitating application of techniques for suppression of this event.

In order to increase the signal-to-noise ratio, MCS data are sorted into common depth point (CDP) or common mid point (CMP) gathers. An example of a 4-fold CDP gather is shown in Fig. 4.2(left). High-fold data significantly improve data quality compared to single-fold or near-trace gathers. In contrast, OBH geometry provides only single-fold data, and reflection points in OBH gathers are spread along the reflecting interface (Fig. 4.2, right). Therefore, an appropriate signal-to-noise ratio has to be assured during acquisition. In the case of approximate 1-D subsurface geometry, the major advantage of OBH records, i.e., large shot-receiver offsets, can be utilized for velocity analysis.
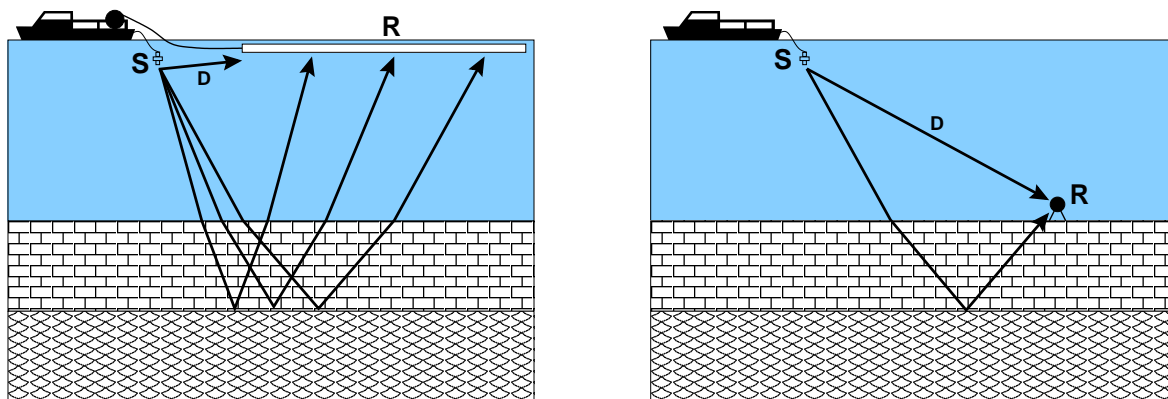
Figure 4.1: *Seismic data were acquired using streamer- and ocean-bottom-hydrophone techniques. Airgun (S) and streamer (R) acquisition geometry in multichannel reflection seismic profiling reveal common shot gathers, where the direct water wave (D) is well-separated from the primary arrivals (left). In airgun-OBH acquisition geometry, the direct water wave often masks shallow primary reflections in the common receiver gather (right).*
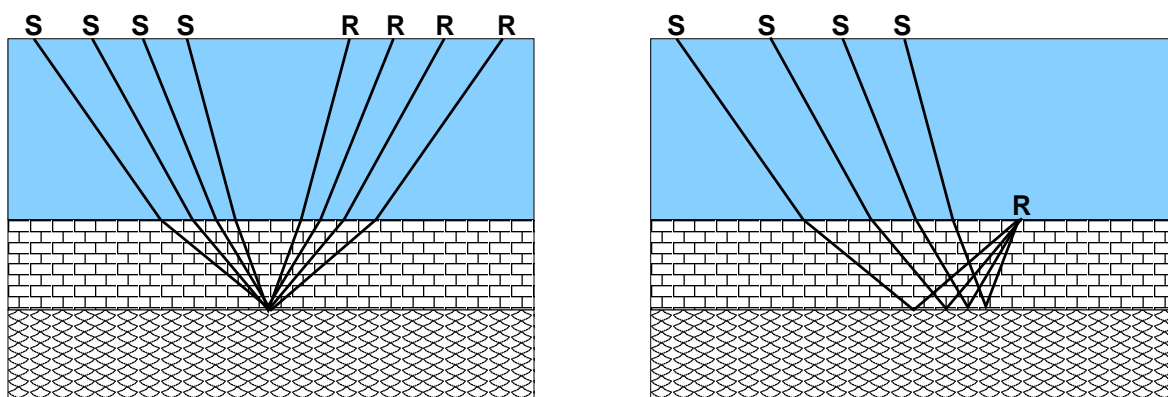

Figure 4.2: *MCS data are processed in common mid point (CMP) or common depth point (CDP) gathers, where the reflection element at the target zone is covered by multiple shot-receiver pairs (left), whereas the reflection points in the common receiver gather are single-fold and spread out over the reflecting interface (right).*

4.2 MCS data processing

A standard seismic processing sequence has been applied to the multichannel seismic sections presented in this thesis. A schematic flow chart of the processing procedure is given in Fig. 4.3, while further details are briefly described below.

Data format

The seismic data have been acquired on a **StrataView R60** acquisition unit (*Geometrics*) in SEG-D format. For data processing, using the software **FOCUS** (*Paradigm Geophysical*), these data have been converted into SEG-Y format.

Editing, geometry, and recording delay

Bad weather conditions intermittently introduced strong noise, especially at the position of depth control birds, on single channels of the shotrecords. To ensure a significant improvement of the signal-to-noise ratio, these traces have been muted.

The acquisition geometry is defined as 24 active sections with 25 m separation and a shot-point distance of 50 m during simultaneous acquisition of MCS and OBH data, and 25 m during exclusive acquisition of MCS data.

The maximum record length at the desired sampling rate of 1 ms was 5 s. Water depths of more than 3800 m necessitated application of a recording delay of 4 s. Since the processing software could not account for this delay-time in the processing modules, shotrecords had to be replenished with zero traces.

Predictive deconvolution

To improve the vertical resolution in the seismic sections, a predictive deconvolution (e.g., Yilmaz, 1987) has been applied. Since tuning of the airgun array was not possible, the initial primary-to-bubble ratio in the data was about 2:1. At the beginning of each line, the source signature has been acquired by omitting the acquisition delay. From these shotrecords, showing the undisturbed direct arrival, a prediction-error-filter was calculated. Application improved the primary-to-bubble ratio up to about 30:1 for individual airgun configurations. A wide band-pass filter was applied to suppress additional noise introduced by deconvolution.

Velocity model

The absence of sufficient moveout in the gathers caused by the short hydrophone streamer and water depths of more than 3800 m did not allow velocity analysis based on normal moveout. Therefore, a velocity gradient starting at 1500 m/s at the seabed and increasing to 2200 m/s at the basement was applied for further processing. This gradient is roughly consistent with velocities determined from OBH records at the bright spots and well logs at the ODP sites.

19

Spherical divergence and NMO correction

The correction for spherical divergence and normal moveout was applied using the assumed velocity gradient. Due to small offsets and low velocities, no NMO stretch-mute was necessary. Subsequently, the data were stacked 12-fold and 6-fold, respectively.

Migration

Finally, a finite-difference time migration was applied to the stacked data. An amplitude balancing applied before migration noticeably improved the results. This gain was withdrawn after the process. For display purposes, a mute above the seafloor reflection and a bandpass-filter of $10 - 120$ Hz showed best results.

4.3   OBH semblance velocity analysis

Semblance based velocity analysis is routinely used to determine the subsurface velocity structure in multichannel seismic surveys showing appropriate normal moveout in CMP gathers (e.g., Yilmaz, 1997). The high angular aperture in the OBH records enables extraction of subsurface velocities as well. The OBHs have been deployed at bright spot locations, where reflectors in the subsurface can be considered as horizontal, and the absence of significant lateral variations in the strata enables assumption of 1-D geometry. Therefore, the source and the receiver (ref. Fig. 4.1) can be considered to be located halfway in the water column simulating a symmetric acquisition geometry, which enables the application of existing routines for semblance velocity analysis. The zero-offset traveltimes are thereby retained. This method is applied to determine indications for a reduction in stacking velocity beneath the bright spot reflections and to determine the subsurface velocity structure at the bright spot locations, since no other on site velocity information is available. The wells from ODP Leg 157 are significantly offset from the area under investigation. An often observed disadvantage in OBH records is that shallow sedimentary reflections are masked by the high-amplitude first arrival, which is a superposition of the direct water wave and the seafloor reflection (ref. Fig. 4.2). To suppress the direct water wave, a common method used in vertical-seismic-profiling surveys (e.g., Hardage, 1983) has been adopted to OBH records. Thereby, the direct water wave is aligned horizontally, and an average estimate of the direct arrival, calculated from a horizontally moving window, is subtracted from the panel. Subsequently, residual energy left from trace-to-trace variations in the source signature shows significantly reduced coherency.

4.4   Amplitude-versus-offset analysis

The variation of reflection and transmission coefficients with incidence angle (and corresponding increasing offset) is referred to as offset-dependent-reflectivity and is the fundamental basis for amplitude-versus-offset analysis. Knott (1899) and Zoeppritz (1919) invoked continuity of displacement and stress at the reflecting interface as boundary
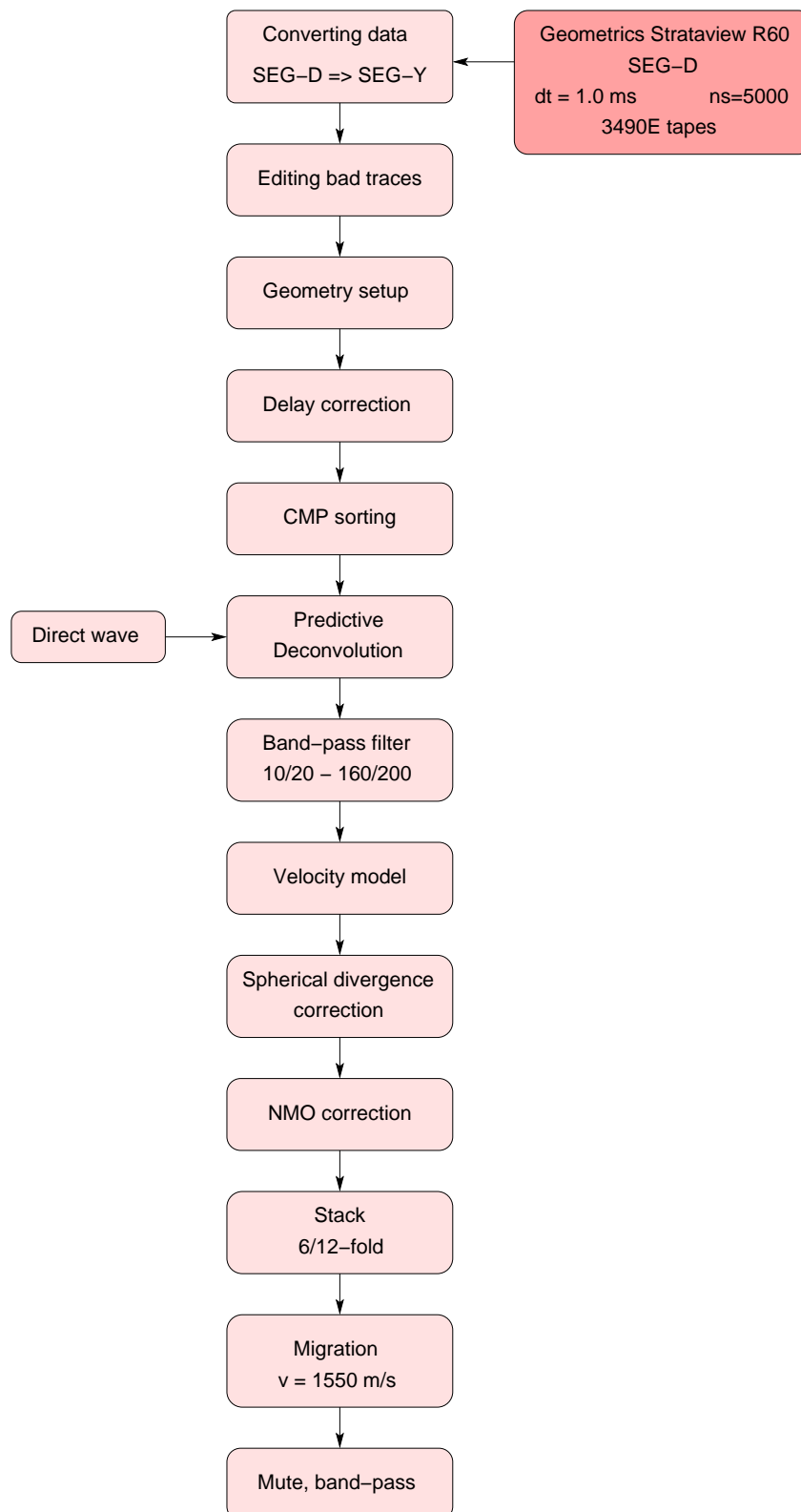
Figure 4.3: *Schematic flow chart of the MCS processing procedure applied in this study.*

conditions to solve for the reflection and transmission coefficients as a function of incident angle and elastic properties of the medium (i.e. density, bulk and shear modulus). The resulting Knott and Zoeppritz equations are complex and subject to troublesome sign, convention, and typographical errors (Hales & Roberts, 1974). Aki & Richards (1980) provided an easily solved matrix form of these equations.

Common incidence angles in exploration seismology are about 30 degrees or less (Castagna, 1993). For easier visualization of how the variation of a particular parameter will effect the reflection coefficient curve in the range of common incidence angles, a number of approximations to the Knott and Zoeppritz equations have been presented. A review of these approximations and their underlying assumptions (usually small contrasts in elastic parameters across the reflecting interface and moderate, precritical angles) is given by Castagna (1993). Since the OBH data used for AVO analysis in this study provide very high angular aperture, an approximation valid for angles approaching the critical angle has to be considered to support the interpretation. A very useful and descriptive approximation of the Aki and Richards equations is given by Shuey (1985), where three terms simply describe different angular ranges of the offset curve. The first term is the normal incidence reflection coefficient, the second term predominates at intermediate angles and is mainly influenced by changes in Poisson's ratio, and the third term is dominant as the critical angle is approached, controlled mainly by changes in P-wave velocity:

$$R_{pp} \approx R_p + \left(A_0 R_p + \frac{\Delta\sigma}{(1-\sigma)^2} \right) \sin^2\Theta + \frac{1}{2}\frac{\Delta V_p}{V_{Pa}}(\tan^2\Theta - \sin^2\Theta) \qquad (4.1)$$

where R_p is the normal incidence reflection coefficient. Θ denotes the angle of incidence, σ the Poisson's ratio and ΔV_P and $\Delta\sigma$ the contrast in P-wave velocity and Poisson's ratio across the reflecting interface, respectively. A_0 and B_0 are given in appendix C.

The aim of this AVO analysis is to constrain the interpretation of the observed bright spots by distinguishing between positive and negative acoustic impedance contrasts based on their significantly different AVO response (e.g., Castagna, 1993). Indications of a negative impedance contrast can be interpreted in terms of presence and amount of free gas based on the estimated Poisson's ratio. A number of fundamental AVO responses for increasing, decreasing and constant Poisson's ratio across an interface have been presented by Ostrander (1984). AVO responses indicating the presence of free gas, can further be classified based on the determined normal-incidence reflection coefficient and the AVO behavior. In this context, three classes of gas reservoirs have been introduced by Rutherford and Williams (1989), based on reservoirs characterized by higher, lower, and by the same impedance contrasts as the encasing sediments.

An amplitude preserving data processing has been applied to the OBH data based on determination of travel-paths and offset-angle relationships using ray tracing. Subsequently, data have been corrected for spherical divergence and anelastic attenuation effects. The latter has been performed assuming frequency independent and effective attenuation coefficients Q. Since the OBH experiment approximates a point source and point receiver, no directivity corrections have to be applied.

A disadvantage when considering AVO analysis on OBH records is that analysis can only be performed on a few locations, and the spreading of reflection points over a distance along the target horizon might lead to inaccuracies (ref. Fig. 4.2). Whereas

common AVO analyses in exploration are performed on common depth point (CDP) gathers and are usually applied to numerous positions across the target horizon in the seismic section. In any case, the lack of wide-aperture reflections in deep-water environments due to limited streamer lengths increases ambiguity. The non-uniqueness of AVO analysis and inversion is outlined in a recent case history, where an iterative and linearized inversion of a Gulf of Mexico bright spot was performed with different starting models (Nsoga Mahob *et al.*, 1999). The location investigated was known as a gas reservoir and well logs provided subsurface P-wave and density control. The inversion was performed using starting models for the pay zone with Poisson's ratio appropriate for 100% brine saturation and with Poisson's ratio intermediate between expected values for brine and hydrocarbon saturation. These two starting models did not converge to the real seismic gather during inversion. However, a starting model with Poisson's ratio appropriate for hydrocarbon saturation in the target zone, showed convergence from the initial to the real seismic gather.

4.5 Full waveform inversion

In order to resolve fine-scale velocity structure around the bright spots, 1-D full wave-form inversion is applied to the wide-aperture OBH data. The waveform inversion aims at finding a seismic model of the subsurface such that the sample-by-sample misfit in the frequency-slowness domain between synthetic and observed seismograms is minimized. The misfit function is highly nonlinear, which means that it contains numerous local optima and thus requires a Monte Carlo random search to confirm that a global minimum is found. Since this approach is very time consuming, the inversion strategy consists of the following two steps: (1) the construction of a reliable background velocity model to represent the long-wavelength or large-scale global minimum, and (2) a local search to estimate the short wavelength variations. The local search implies a generalized least squares inversion method based on estimation of velocities by minimization of the misfit in the frequency-slowness domain using a conjugate gradient optimization sheme (Kormendi & Dietrich, 1991). The synthetic wavefield is thereby calculated using the generalized reflection and transmission matrix method of Kennett and Kerry (1979), which accurately treats multiples and mode conversions in the medium, and thus includes all nonlinear effects. These methods have been implemented in the FORTRAN program **inv1d**. Details and examples are given in Kormendi and Dietrich (1991). The inversion code has recently been adapted for OBH geometry (Korenaga *et al.*, 1997). A schematic flow chart of the inversion procedure is given in Fig. 4.4, and further details are briefly specified below.

Theory

If $\mathbf{d}_{obs}(p, \omega)$ is a vector containing the discrete samples of the plane-wave response of the observed seismogram and m is a vector describing the properties of the stratified medium, the misfit function is defined as (Tarantola & Valette, 1982):

$$S(\mathbf{m}) = \frac{\|\mathbf{d}_{cal}(p, \omega) - \mathbf{d}_{obs}(p, \omega)\|_D^2 + \|\mathbf{m} - \mathbf{m}_0\|_M^2}{2} \tag{4.2}$$
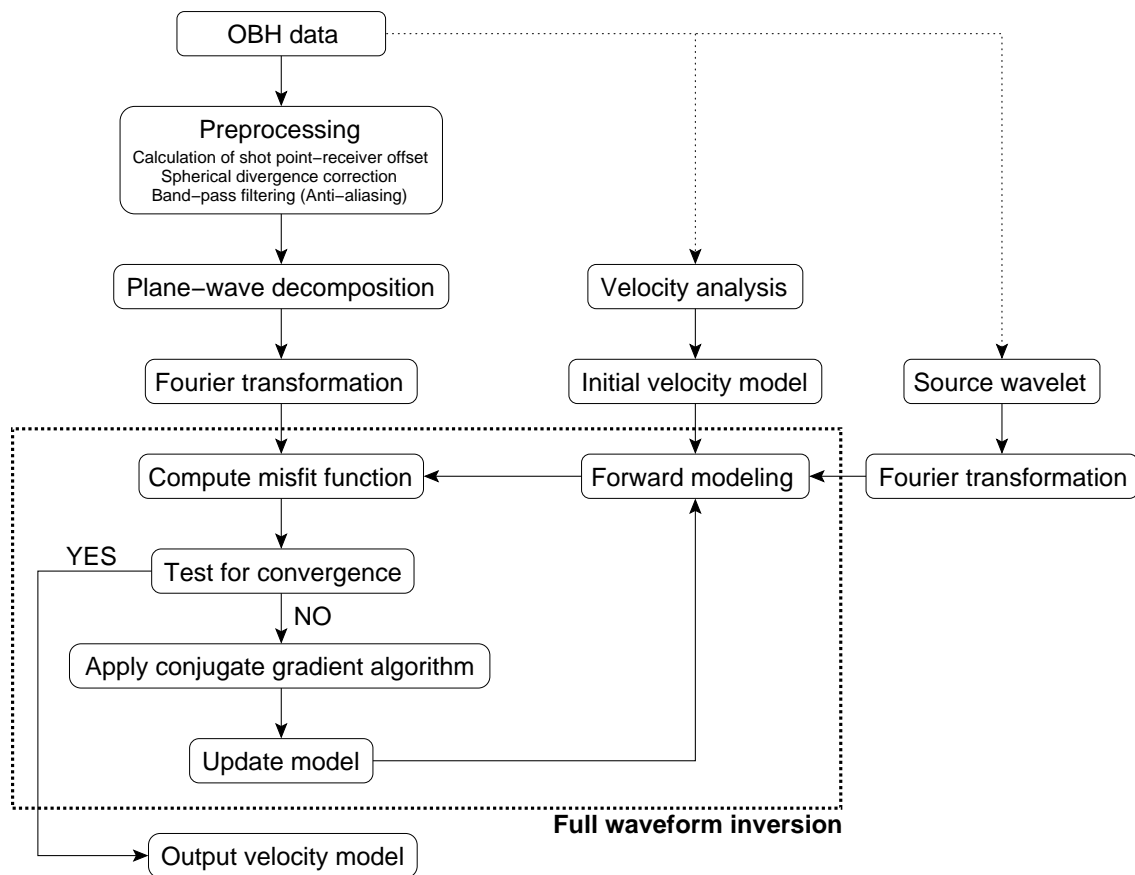
Figure 4.4: *Schematic flow chart of the waveform inversion procedure applied in this study.*

where $\mathbf{d}_{cal}(p, \omega) = f(\mathbf{m})$ is the synthetic seismogram derived from the forward modeling operator f, and $\mathbf{m}_0$ is the initial model. p is the horizontal slowness and ω is the angular frequency. The norms $\|.\|_D^2$ and $\|.\|_M^2$ are weighted L_2 norms defined as:

$$\|\mathbf{d}\|_D^2 = \mathbf{d}^{*T}\mathbf{C}_D^{-1}\mathbf{d} \tag{4.3}$$

$$\|\mathbf{m}\|_M^2 = \mathbf{m}^T\mathbf{C}_M^{-1}\mathbf{m} \tag{4.4}$$

where $\mathbf{C}_D$ and $\mathbf{C}_M$ are the covariance matrices for data and model, respectively. T denotes the transpose of the matrix, and * denotes the complex conjugate. The data and model covariance matrices used for the inversion were $\mathbf{I}$ and $2\mathbf{I}$, respectively, where $\mathbf{I}$ is the identity matrix. This combination has been successfully applied by Korenaga *et al.* (1997) on OBH data. Changing these values by a small factor produced almost the same results with respect to model evolution. Further details on the implementation of the algorithms and the minimization of the misfit function $S(\mathbf{m})$ by conjugate gradient technique are given by Kormendi and Dietrich (1991).

24

Data preprocessing

Thorough preparation of the data set prior to $\tau - p$ transformation is essential to guarantee adequate inversion results. Exact shot point-receiver offsets are particularly necessary for OBH geometry. These might be provided by navigational data or can be calculated from traveltimes of the first arrival and the water depth (e.g., from onboard echo sounder). Correction for spherical divergence has been applied using the estimate of a background velocity model. To avoid spatial aliasing in the data, it is necessary to have trace intervals Δx of:

$$\Delta x \leq v/(2f_{max}) \qquad (4.5)$$

where v is the slowest horizontal phase velocity in the data and f_{max} is the maximum frequency present. Hence, the Nyquist ray parameter is:

$$p_N = 1/(2f_{max}\Delta x) \qquad (4.6)$$

Unfortunately, field data often do not meet these requirements. Shot or receiver gathers usually display trace-to-trace phase correlations with a wide variety of slownesses. To retain the full frequency range, interpolation of the data to a finer spatial sampling rate and application of a weighting filter based on dominant slownesses in different parts of the seismic section has been suggested by Singh *et al.* (1989). The OBH data considered for waveform inversion have been acquired with shot point intervals of 25 m and a Nyquist frequency of 100 Hz. To prevent aliasing, band-pass filtering of $8 - 50$ Hz has been applied.

Source wavelet and seafloor reflection coefficient

The source wavelet for the inversion is deconvolved from first arrival wavelets and first water column multiples for near vertical incidence traces ($x \leq 150$ m). The receiver (OBH) is located at the seafloor, and the first arrival is thus a combination of the direct water wave and the seafloor reflection. After spherical divergence correction using a compressional velocity of 1500 m/s for the water column, the first arrival P and the multiple M may be expressed as (e.g., Korenaga *et al.*, 1997):

$$P(t + T_{sf}) = (\delta(t) + r(t)) * s(t) \qquad (4.7)$$

$$M(t + 3T_{sf}) = -(\delta(t) + r(t)) * r(t) * s(t) \qquad (4.8)$$

where T_{sf} is the one-way travel time from the sea surface to the seafloor, $\delta(t)$ is the delta function, $r(t)$ is the seafloor reflectivity series, $s(t)$ is the source wavelet, and $*$ the convolution operator. The seafloor reflectivity series $r(t)$, and thus the seafloor reflection coefficient is then extracted as Wiener shaping filter from the following equation derived from substituting equation 4.7 into equation 4.8:

$$-M(t + 3T_{sf}) = P(t + T_{sf}) * r(t) \qquad (4.9)$$

Finally, the source wavelet $s(t)$ is also extracted as Wiener shaping filter from equation 4.7. The source wavelet is designed to include up to the fifth bubble pulse. The alternative method is to suppress the bubble pulse sequence in OBH records by deconvolution. Unfortunately, this method often introduces significant noise due to the predominating amplitudes of the direct arrival and inconsistent airgun signature (e.g., Katzman *et al.*, 1994).

Initial model

A reliable estimate of the large-scale P-wave velocity model is necessary to ensure that the inversion for short-wavelength variations is started near the global minimum of the misfit function. Otherwise, the inversion algorithm might be "trapped" in a local minimum, which can lead to misinterpretation. Various methods have been presented to determine an optimum long-wavelength velocity model. Singh and Minshull (1994) presented a two step method, where the RMS velocity was estimated by maximizing the energy within a time window centered on individual reflectors along ellipses in the $\tau - p$ domain. In the second step, interval velocities for the observed reflections were searched simultaneously by maximizing the total energy from all trajectories. A traveltime inversion has been applied by Korenaga *et al.* (1997) to determine the long-wavelength model. These methods have been applied to locations showing several distinct reflections between seafloor and target horizon. The simplicity of seismic structure at the target reflectors in this study, where the overburden can be approximated by one single layer, enables the application of simple $X^2 - T^2$ method to extract reliable overburden P-wave velocity information. Remaining parameters to establish a viscoelastic starting model are the shear-wave velocity (Vs), the density ρ, and quality factors Q_p and Q_s for P-wave and S-wave attenuation, respectively. These parameters are calculated from the determined P-wave velocity function using empirical relationships for Vs (Castagna *et al.*, 1985) and ρ (Hamilton, 1978). Effective quality factors of $Q_p = 200$ and $Q_s = 100$, appropriate for shallow unconsolidated sediments, are implemented (Hamilton, 1972), while well log information from ODP site 956 are considered as a reference. These parameters are kept constant during the entire inversion.

Plane-wave decomposition

The forward modeling algorithm and calculation of the misfit during the inversion is performed in the delay time-slowness ($\tau - p$) domain. The plane-wave decomposition of a point-source seismogram obtained from a horizontally stratified medium allows the separation of wave energy by angle of incidence. This enables a more rapid modeling, since it is faster to compute synthetic seismograms in the $\tau - p$ domain than in the $t - x$ domain (Singh *et al.*, 1989).

Transformation of OBH data into the $\tau - p$ domain is carried out utilizing the routine **segy_ftaup**, provided by J. Korenaga (Massachusetts Institute of Technology; pers. communication). In the time domain, this program applies a slowness dependent

aliasing removal proposed by Singh et al. (1989). Subsequently, a spatial damping filter is adopted to taper traces at large and small offsets in order to suppress artifacts, often introduced by the inconsistent airgun signature in OBH records. Thereafter, the data are transformed into frequency domain, where a radon transformation of the data into frequency-slowness domain is performed. Finally, data are transformed back into delay time-slowness domain using the inverse Fourier transformation. The following successive transformations are implemented in the code:

Fourier transformation:

$$\hat{u}(\omega, x) = \int_{-\infty}^{\infty} u(t, x)e^{j\omega t}dt \tag{4.10}$$

Hankel transformation:

$$\hat{u}(\omega, p) = \int_{0}^{\infty} \hat{u}(\omega, x)J_0(\omega px)xdx \tag{4.11}$$

Inverse Fourier transformation:

$$u(\tau, p) = \frac{1}{2\pi} \int_{-\infty}^{\infty} \hat{u}(\omega, p)e^{-j\omega\tau}d\omega \tag{4.12}$$

Inversion

The starting model, the source wavelet and the OBH data are used as input for the full waveform inversion. All model parameters except the P-wave velocity are kept constant during the inversion. The underlying assumption is that the observed bright spot reflections can be related to significant changes in Vp, while ρ and Vs show very little change. This is approximately true, when pore-fluids are partly replaced by free or dissolved gas (Biot, 1956) as e.g. observed at BSRs. A strategy of progressive increase in bandwidth and slowness range during inversion is illustrated by Minshull *et al.* (1994) and Minshull & Singh (1993). Unfortunately, further limitations of the narrow frequency band implemented for the OBH data were not reasonable. A number of trials considering low slownesses first, and then progressively include contributions from the high slowness range failed, which was obviously due to high ambiguity of the inversion result in the lower slowness region. Therefore, all slownesses and frequencies are inverted simultaneously. The inversion is then performed in runs of 5 iterations each. The final result from each run is smoothed and serves as a starting model for the next run. This is repeated until the misfit function changes little (less than 1%), indicating convergence. This is followed by inverting for several basic starting models, including the derived best-fit model, in the lower slowness range to evaluate ambiguity. Finally, inversion is performed for the full slowness range and basic starting models to analyze uniqueness of the determined results.

27

Chapter 5

Evidence of Fluid Reservoirs

During the investigation of submarine landslides on the flanks of the Canary Islands (R/V *Poseidon* cruise 236) a number of pronounced seismic bright spots were discovered on a reconnaissance profile in the Southern Canary Basin. The bright spot reflections, characterized by increased reflection amplitudes and polarity reversal, were considered as direct hydrocarbon indicators in terms of Sheriff (1991). On a second cruise (R/V *Poseidon* cruise 251) the areal extent of these potential reservoirs was mapped at two selected locations and ocean-bottom-hydrophones were deployed to record wide-aperture reflections in the vicinity of the bright spots. Multichannel reflection seismic sections imaging these bright spots are presented in this chapter.

5.1 Reconnaissance seismic line 28/97

The seismic line 28/97 is approximately 215 km in length and extends from about 60 km southwest of El Hierro island up to the southwestern submarine volcanic apron of Gran Canaria (Figs. 5.1 and 5.2). The initial intention for acquisition of line 28/97 during R/V *Poseidon* cruise 236 was to facilitate the seismostratigraphic interpretation of the grid of 2-D reflection seismic lines southwest of El Hierro island based on well-control by ODP site 956, located southwest of Gran Canaria. A standard CMP processing sheme has been applied. Prestack predictive deconvolution (70 ms predictionlag, 700 ms operatorlength) was applied to suppress the strong bubble pulse sequence. A spherical divergence correction assuming a simple velocity gradient from 1500 m/s near the seafloor increasing to 2000 m/s at 5.6 s TWT restored approximate relative amplitude ratios. Thus, maximum shotpoint-receiver offsets of 600 m at water depths of more than 3500 m did not allow more detailed velocity analysis. Finally, data were stacked 12-fold. The section was not migrated due to large lateral velocity variations and in order to classify reflection events by occurrence of diffraction hyperbolas. The stacked section is laterally subdivided into four regions in which the character of the reflections suggest different type and origin:

- The high-reflective and continuous sedimentary sequences in the west.

- Pronounced basement topography rising towards the seafloor (CMP 4500).

- Well-stratified sediments of low reflectivity embedding pronounced high-amplitude reflection events in the central part.

- The submarine volcanic apron of Gran Canaria and ODP site 956 in the east.

The seafloor gently dips from 4.4 s TWT (3300 m) in the east to 5.1 s TWT (3800 m) in the west of the profile, where the maximum penetration of the seismic signal of more than 1.1 s TWT was attained. Major faults affecting the entire sedimentary sequence might be related to compression and consolidation processes. A pronounced dipping reflector marks the top of the volcanic basement, which rises from 5.8 s TWT at CMP 1600 towards the east and reaches the seafloor near CMP 4500, while the penetration depth of the seismic signal is successively reduced. Sedimentary sequences onlapping the volcanic basement in the east indicate that sedimentation occurred after formation of the volcanic structure. The high-reflective sedimentary sequences to the west in contrast to weak-reflective sequences east of the volcanic structure validate the different sedimentation regime. Considering bathymetry information, this basement structure is interpreted as the subseafloor volcanic edifice of Henry Seamount (ref. Fig 2.1).

Near-surface sediments between CMP 4600 and 7000 show chaotic reflection pattern, most probably related to debris flow deposits originating from El Hierro island. The overall character of the sedimentary sequence beneath, down to $\sim$5.5 s TWT, is characterized as sub-horizontal and weakly reflective. A slightly undulating bright reflection band between CMP 7000 and 11000 at $\sim$5.6 s TWT showing smooth topography is not interpreted as volcanic basement. The origin of this reflection might be related to major changes in lithology (consolidation) or increased acoustic impedance contrasts due to the presence of gas. Between CMP 12000 and 13000 at about 5.5 s TWT, strong diffractions are observed, which might be related to igneous material that has been injected into the sedimentary sequence.

Towards the eastern part of line 28/97, the basement depth decreases from 5.6 s TWT at CMP 13000 to $\sim$5.1 s TWT at CMP 17000. ODP site 956 is located near CMP 17000 and penetrates through the sedimentary sequence down to the acoustic basement at $\sim$5.1 s TWT. A noticeable high-amplitude reflection event can be traced from CMP 15000 to the end of the profile in the east. Due to the high continuity and reflection amplitudes this event is considered as regional marker horizon. It originates from slump debris deposits of volcaniclastic material consisting of tuffs and lapillistone from the Roque Nublo phase of volcanism on Gran Canaria (Schmincke *et al.*, 1995).

In the western and central part of the profile at about 5.3 s TWT (400 to 600 ms below seafloor) a number of strong amplitude anomalies in the sedimentary column are considered to be the most striking observation, which has not yet been reported in literature. They are characterized by increased reflection amplitudes against the embedding sediments. They tend to follow the sedimentary bedding and show inline extents of about 5 km (CMP 1600, 2500, 5600, 10500, 11500, and 13200). These reflections are in the following referred to as 'bright spots'. Based on lithologic units identified at ODP site 956, they are embedded in sediments of middle Miocene age. Bright spots are considered as direct hydrocarbon indicators since they effectively pinpointed gas reservoirs in the Gulf of Mexico, although several examples of bright spots not related to hydrocarbons have been presented in literature (Sengbush, 1983).
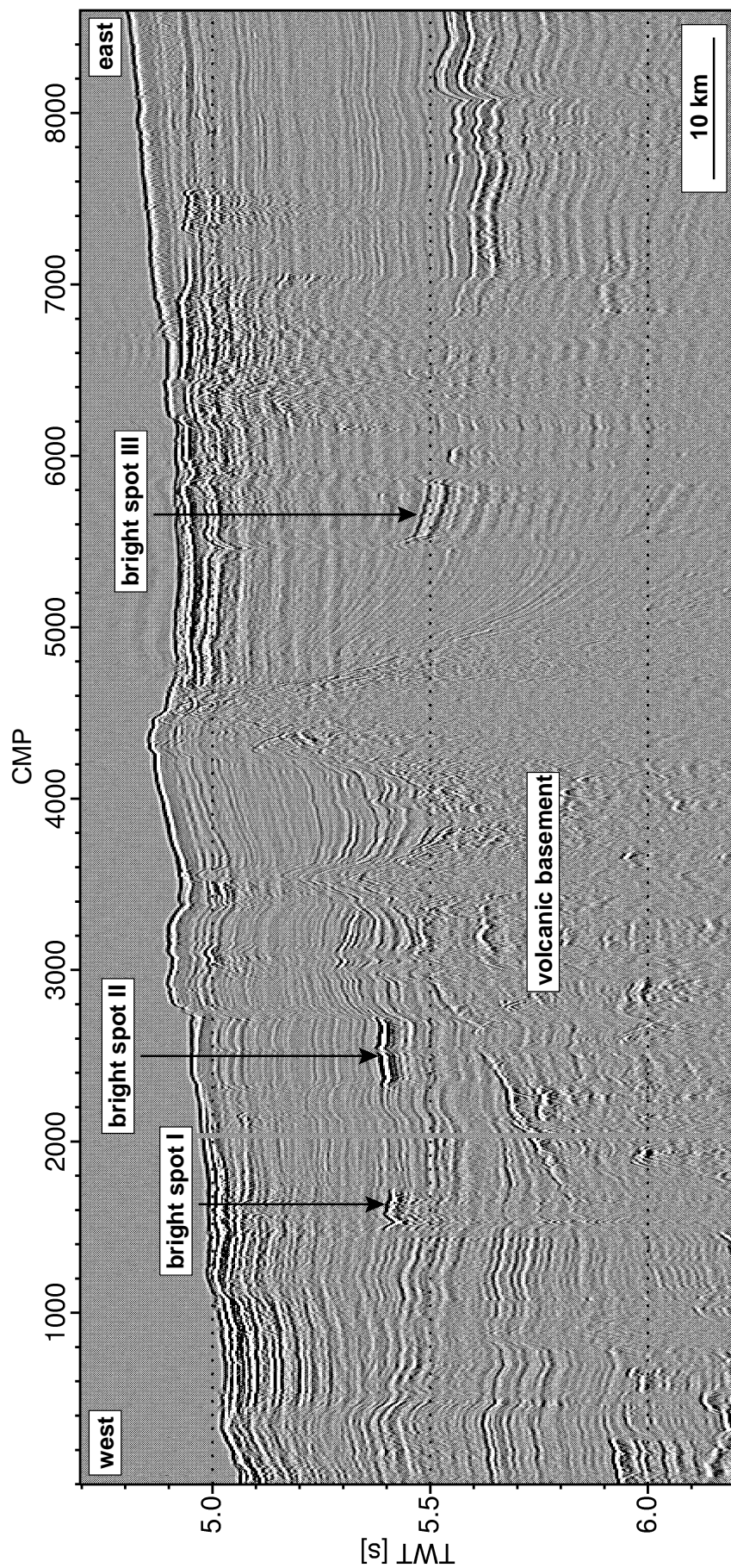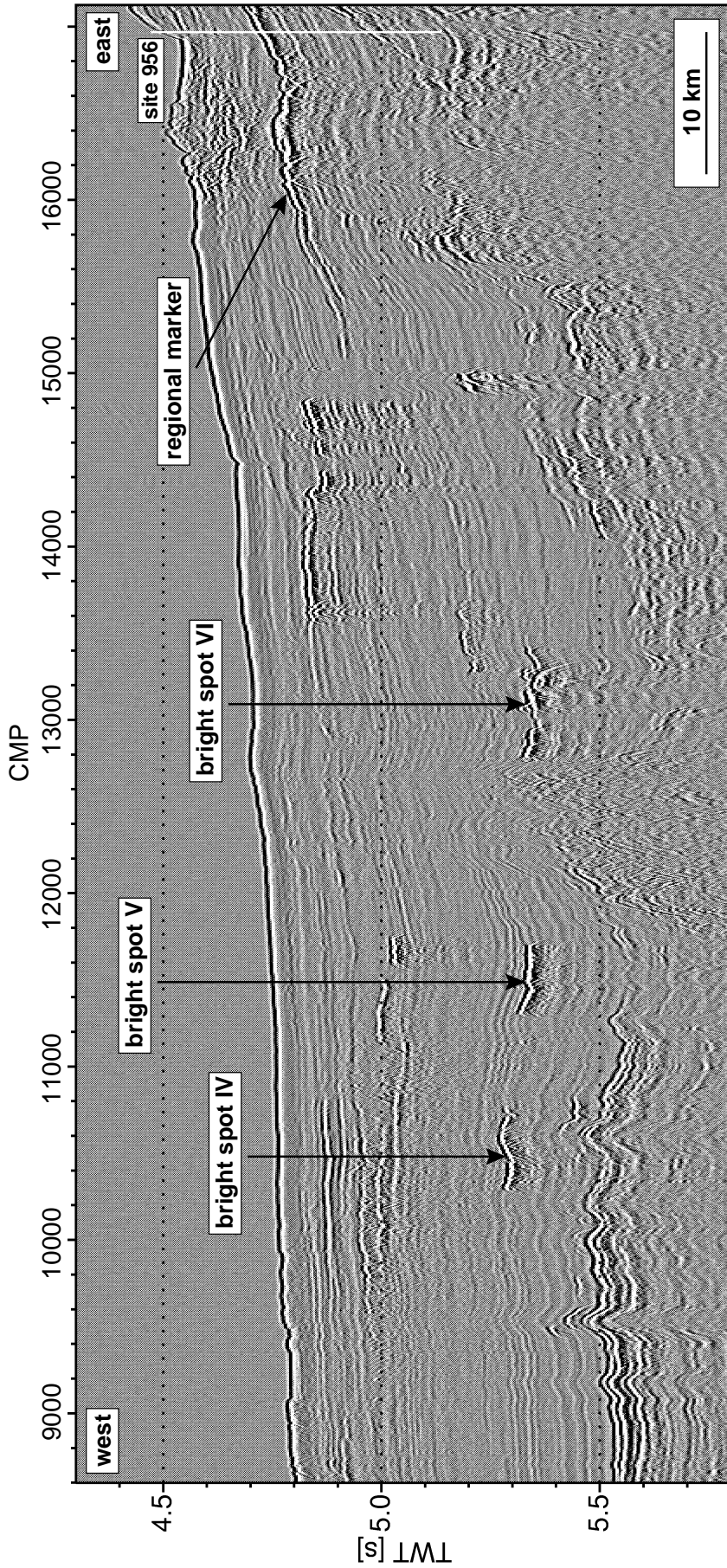
Figure 5.1: *Stacked seismic section of the 215 km long line 28/97, western part (CMP 1 – 8600), showing three pronounced bright spot reflections (I – III) in the vicinity of basement topography, that is interpreted as the sub seafloor volcanic edifice of Henry Seamount. Data were collected with a 2 gun, 1.2 l (70 in³) airgun array and a 24 channel, 600 m long hydrophone streamer. The data shown have been corrected for spherical divergence and stacked 12-fold. No further time-dependent gain has been applied to preserve true amplitude ratios in the section (V.E = 43).*

Figure 5.2: *Stacked seismic section of the 215 km long line 28/97, eastern part (CMP 8600 – 17200), showing three pronounced bright spot reflections (IV – VI). Between CMP 12000 and 13000 strong diffraction hyperbolas indicate intrusion of igneous material. To the east of CMP 15000 the submarine volcanic edifice of Gran Canaria is characterized by increased reflectivity related to volcaniclastic deposits. The regional marker horizon has been identified as slump debris deposits of tuffs and lapillistone associated with the Roque Nublo phase of volcanism on Gran Canaria (Schmincke et al., 1995). ODP site 956 is located near CMP 17000 (V.E = 43).*

31

5.2   Seismic grid south of El Hierro island

In order to map the areal extend and to exclude an origin of the bright spots related to volcaniclastic deposits from the islands or submarine seamounts, a dense grid of 2-D reflection seismic lines has been acquired in the vicinity of bright spot II. Seven seismic lines (9, 13, 14, 15, 16, 17, and 19) clearly image the inline extent of the bright spot reflection, which is exemplified on seismic lines 19 and 17 below.

Seismic line 19 connects the survey area south of El Hierro island via the submarine volcanic apron with the survey area southwest of El Hierro. In the 40 km long section of line 19 (Fig. 5.4) the uniform and undisturbed seafloor reflection is imaged at a water depth of about 3750 m (5.0 s TWT). Well-stratified sediments of almost 1 s TWT thickness are observed in the southeastern part of the profile, while near surface sediments in the northwestern part of the section show a chaotic reflection pattern, indicating the approach to the submarine volcanic apron of El Hierro. The acoustic basement in the section is characterized as highly reflective with rough topography. Bright spot II is imaged between CMP 900 and 1250 at 5.4 s TWT below the seafloor showing a clearly restricted inline extend of ~4400 m, indicated by suddenly decreasing reflection amplitudes at the terminations. The continuity of the well-stratified sedimentary sequences in the central part of the profile is distorted by occurrence of 'seismic chimneys', which are interpreted as mud diapirs indicating migration paths of gas-saturated sediments towards the seabed. Similar features have been observed e.g. in shallow reflection seismic sections from Heggland (1997) in the area of Sleipner Gas Field in the North Sea. The close spatial association of mud diapirs and bright spots suggests that both features can be associated with the presence of gas accumulations in the subsurface. Overpressured muds of increased buoyancy might break the overlying sediments forming the mud diapirs observed at CMP 1350, 1800, and 2300. The diapir at CMP 1800 comprises the entire sedimentary column and develops a mud volcano on the seabed. The base of diapirs is imaged in the same horizon as the bright spot at about 5.6 s TWT. Beneath the smallest diapir at CMP 1350, the basement clearly can be identified, which also confirms a non-volcanic origin of theses features. The basement might be masked by increased absorption of seismic energy at the larger diapirs. The largest mud diapir at CMP 1800 is located at the highest basement level and might be associated with increased supply of gas.

On seismic line 17/99, bright spot II is imaged perpendicular to line 19/99. The bright spot is identified as a smooth reflection surface between CMP 170 and 570 (5000 m) at ~5.4 s TWT (0.45 s bsf), embedded in well-stratified sediments of low reflectivity. The undisturbed seafloor reflection is characterized by a clear black-white-black amplitude sequence, while the bright spot reflection shows an opposite, white-black-white polarity. The top of the acoustic basement gently deepens from 5.55 s TWT in the east to 5.75 s TWT in the west part of the section. The bright spot reflection shows similar terminations on all other profiles. From this, an approximate areal extent of 25 km^2 has been calculated for this location. Furthermore, this grid of 2-D data provides the understanding that the bright spots are definitely not associated with e.g. long lava flows or debris flow deposits originating at the islands or local submarine seamounts.
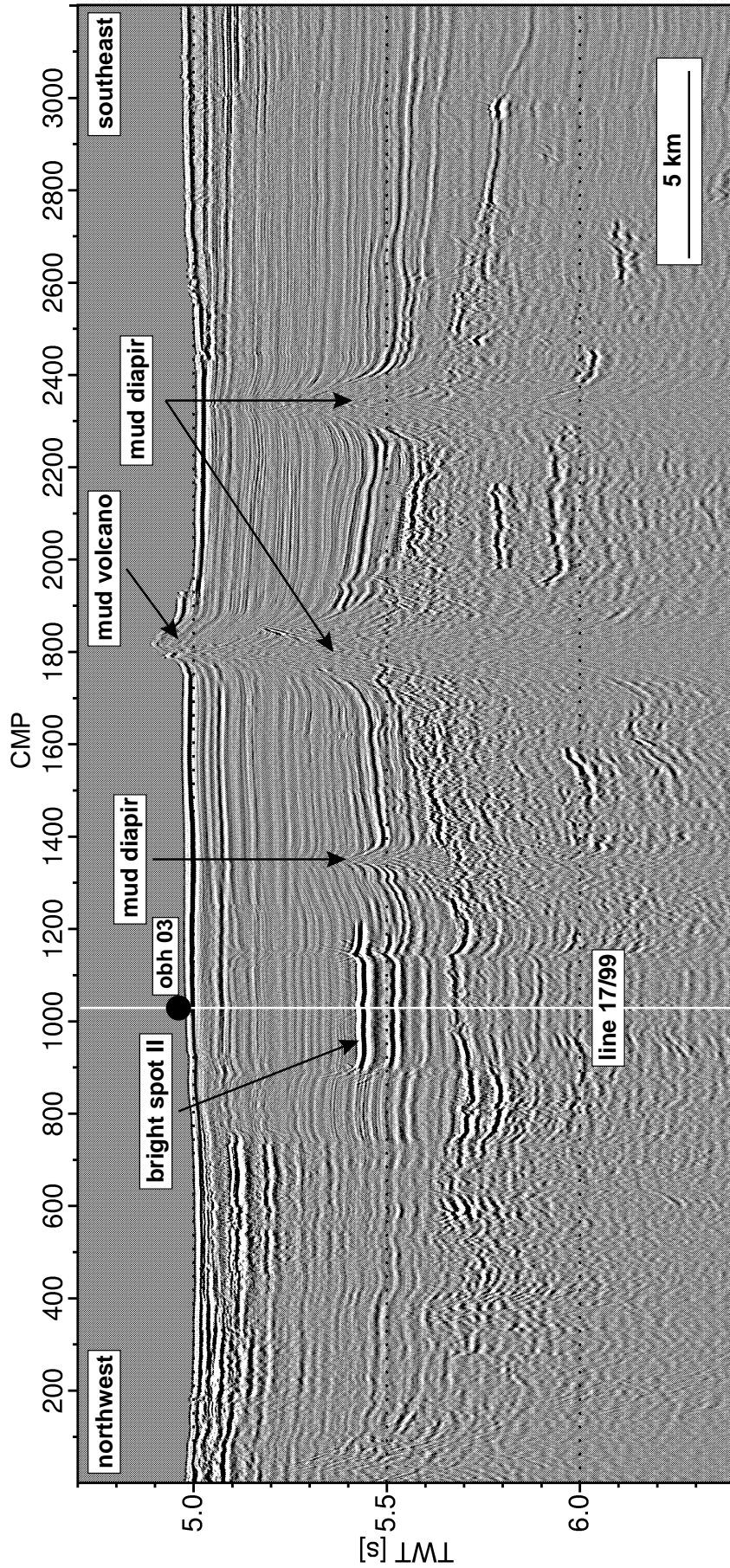
Figure 5.3: *Migrated seismic section of line 19/99 across bright spot II (CMP 900 − 1220). Three mud diapirs at CMP 1350, 1800, and 2300 indicate vertical sediment mobility related to overpressured gas-charged sediments in the subsurface. Note the mud volcano on the seabed at CMP 1800 aligned with the mud diapir in the subsurface. In the northwestern part of the section, increased reflectivity near the seafloor associated with reduced penetration of the seismic signal indicate the approach of the submarine apron of El Hierro (V.E. = 14).*
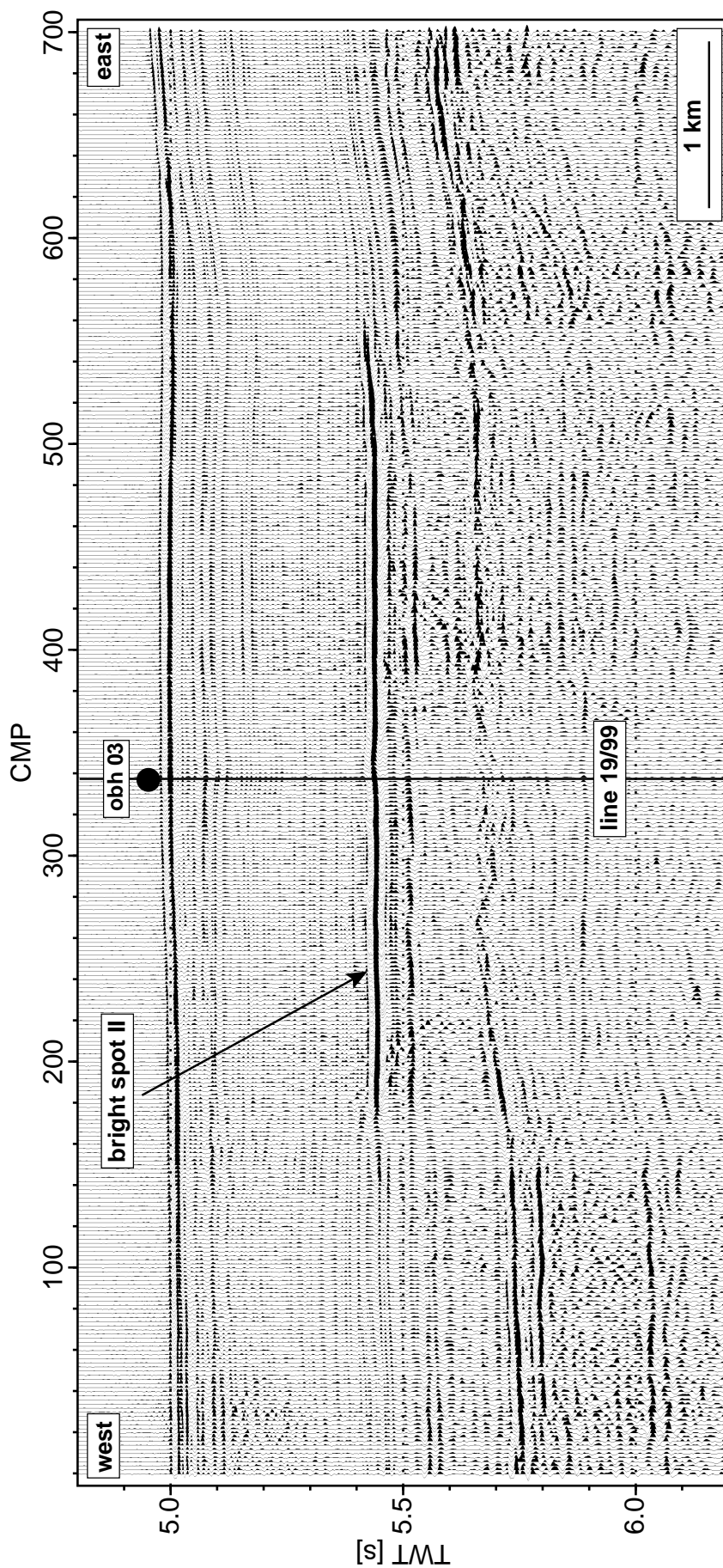
Figure 5.4: *Time-migrated east-west cross section from line 17/99 showing bright spot II. The seafloor reflection is clearly characterized by a black-white-black amplitude sequence, while the bright spot shows an opposite, white-black-white, amplitude sequence indicating a phase reversal. The position of the intersection with line 19/99 and OBH station 03 are indicated (V.E. = 4).*

5.3   Seismic grid southwest of El Hierro island

The most western seismic bright spot imaged in the Southern Canary Basin is located about 70 km southwest of El Hierro island. An areal extent of almost 100 km^2 for this reflection anomaly has been mapped on a dense grid of ten reflection seismic lines. A depth of 900 ms below seafloor at ∼6.1 s TWT distinguishes this structure from bright spot I through VI (400 to 600 ms below seafloor). Two seismic lines from this grid (35 and 37) are presented below.

On the 45 km long section of seismic line 35/99 (Fig. 5.5), two less-distinct mud diapirs are imaged at CMP 800 and 2200 about 300 and 600 ms below seafloor. These structures only affect the lower part of the sedimentary sequence. The seafloor is developed as smooth reflection at ∼5.2 s TWT (3900 m). The well-developed rough basement is overlain by a well-stratified sedimentary sequence of ∼1 s TWT thickness in the southern part of the line. The depth of the basement increases from ∼800 ms below seafloor in the north to about 1.2 s TWT below seafloor in the south. The bright spot reflection, imaged between CMP 1400 and 1760 (4500 m), is gently dipping towards the south, following the sedimentary bedding.

The 90 km long section of seismic line 37/99 (Fig. 5.6) is characterized by a gently dipping seafloor from 5.0 s TWT (3750 m) in the east to 5.4 s TWT (4000 m) in the west. Shallow sediments in the eastern part show chaotic reflection pattern accompanied by high reflectivity that decrease the penetration depth of the seismic signal, indicating debris flow deposits originating from El Hierro island or the African continental margin. The entire sedimentary sequence in the eastern part of the profile is characterized by discontinuous and disrupted reflections. The basement is not clearly developed, which might indicate modification of the crust and the sedimentary sequence by the Canary volcanism. A few high-amplitude reflection events in this region are attributed to magmatic intrusions (sills) or volcaniclastic deposits from debris flows. In contrast, more than 1.5 s TWT of well-stratified sediments are imaged above the rough but well-defined basement in the west of the section. A pronounced basement step of about 500 ms TWT is observed at CMP 600. This basement is interpreted as the top of the igneous oceanic crust (layer 2A), which agrees with the interpretation of Ranero *et al.* (1995) based on MCS reflection seismic lines west of El Hierro island. The sedimentation regime clearly changes from the influence of the Canary volcanism in the vicinity of the submarine apron of El Hierro in the east to undisturbed pelagic sedimentation in the west. The bright spot is imaged between CMP 3100 and 4400 following the westward dipping sedimentary sequences including two steps of about 0.05 s TWT at CMP 3500 and 4100. The undisturbed amplitude sequence of the bright spot (white-black-white) in the region of CMP 3250 indicates a phase reversal in contrast to the undisturbed seafloor reflection (black-white-black) in the western part of the profile.

Five OBHs have been successively deployed along line 26/99 and line 37/99 to record wide-angle reflections in the vicinity of the bright spot. Ray-tracing and 1-D traveltime inversion applied to OBHs 8, 12, and 13 provide a background P-wave velocity model (Papenberg, 2000), plotted together with the seismic section in Fig. 5.6. The velocity steadily increases from 1500 m/s near the seafloor to 1700 m/s at 5.75 s TWT, where the base of the reflective sedimentary sequence is represented by a velocity step from
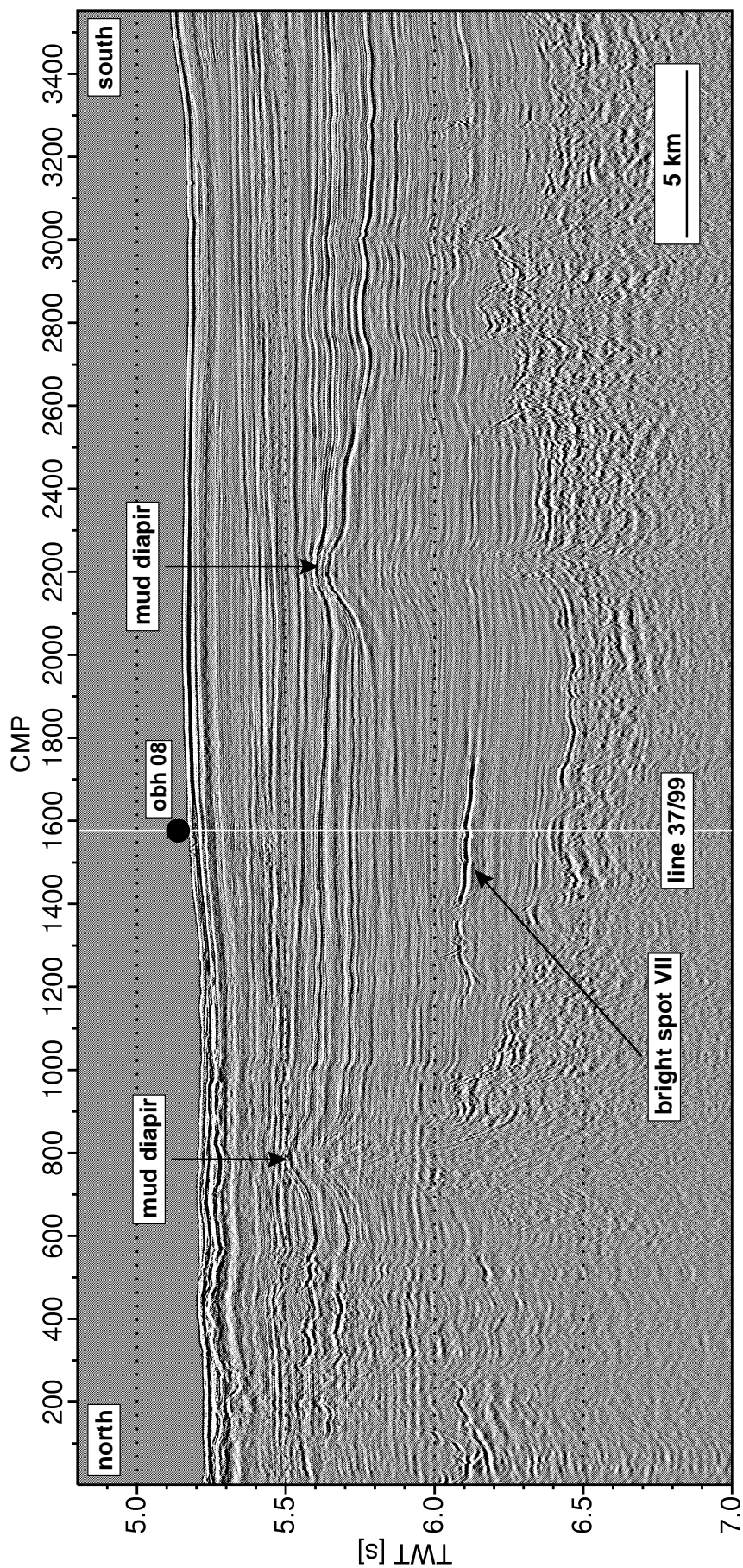
Figure 5.5: *45 km long segment of line 35/99 showing less-distinctive mud diapirs at CMP 800 and 2200 in depths of 5.5 and 5.6 s TWT. The bright spot is imaged between CMP 1400 and 1750 (4375 m) at 900 ms below seafloor. The position of the intersection with seismic line 37/99 and OBH station 08 is indicated. The section has been time-migrated (V.E. = 12).*
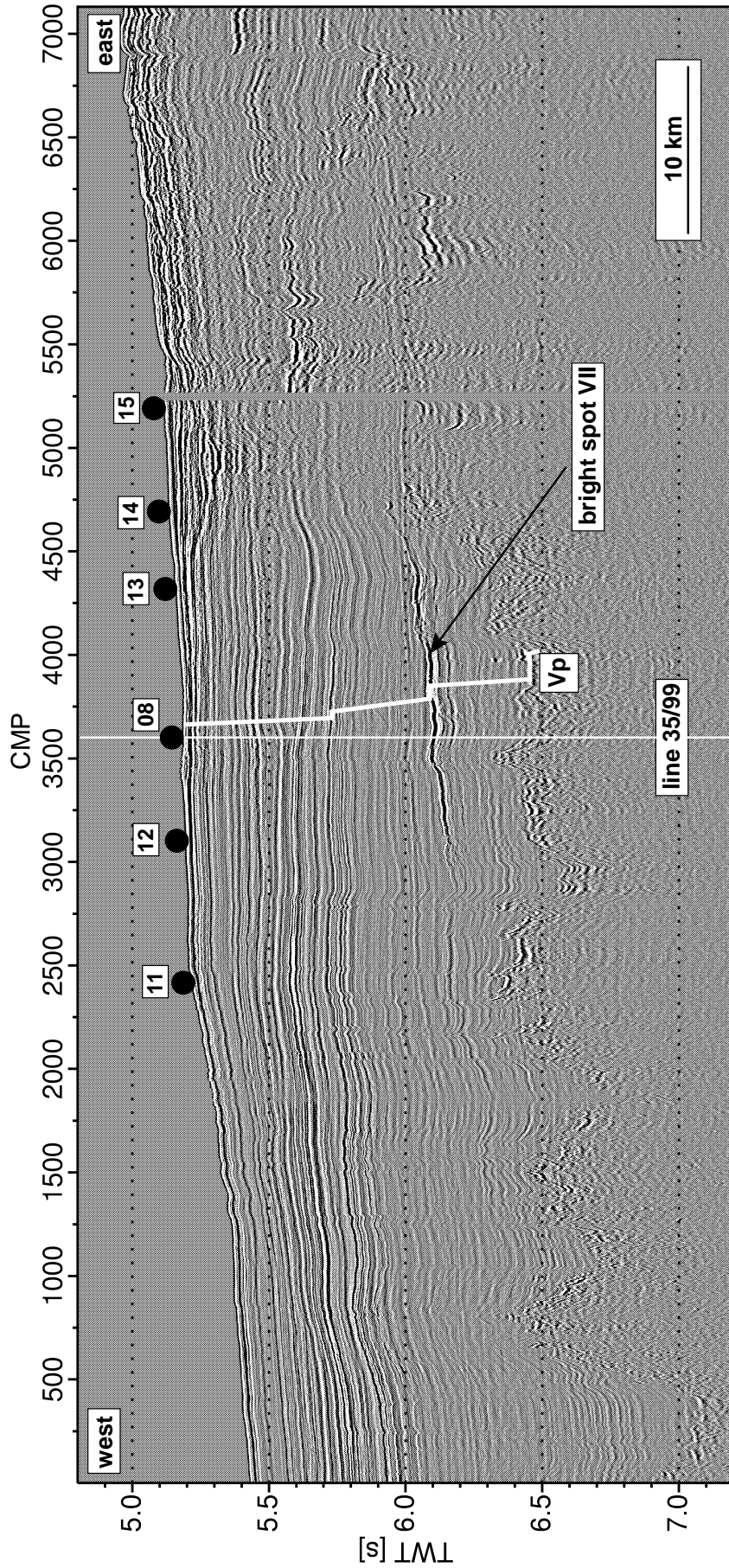
Figure 5.6: 90 km long segment of line 37/99 showing bright spot VII extending between CMP 3100 and 4400 at about 6.1 s TWT. The basement in the western and central part of the profile is interpreted as the top of the oceanic crust. The position of six ocean-bottom-hydrophone stations is indicated. The subsurface velocity model at the bright spot location has been derived from traveltime inversion (see text for details). The section has been time-migrated (V.E. = 22).

1700 m/s to 1800 m/s. Towards the bright spot, the velocity steadily increases to 2600 m/s and steps to 2900 m/s at 6.1 s TWT. A velocity gradient of 0.4 s^{-1} beneath the bright spot suggests a uniform sequence of sedimentary rock. At the basement, the velocity increases from 3100 m/s to about 4300 m/s, indicating velocities representative for the igneous oceanic crust (layer 2A). The traveltime inversion could not resolve a low- or high-velocity zone at the bright spot. Thus, the velocity increase assumed in the background model does not reproduce the observed amplitudes and the phase-reversal at the bright spot, but provides significant constraints for further analysis (i.e. AVO, inversion).

The extent of the bright spot reflection has been mapped on individual profiles to estimate the areal extent. Seismic lines 26, 28, 30, 32, 37, and 39 have been processed including navigational data for every shot-point, which provided exact positions of the bright spot terminations on the profiles, defined by a sudden decrease in amplitude within a few CMPs (a few hundred meters). An areal extent of about 100 km^2 has been calculated for this bright spot location (Fig. 5.7).
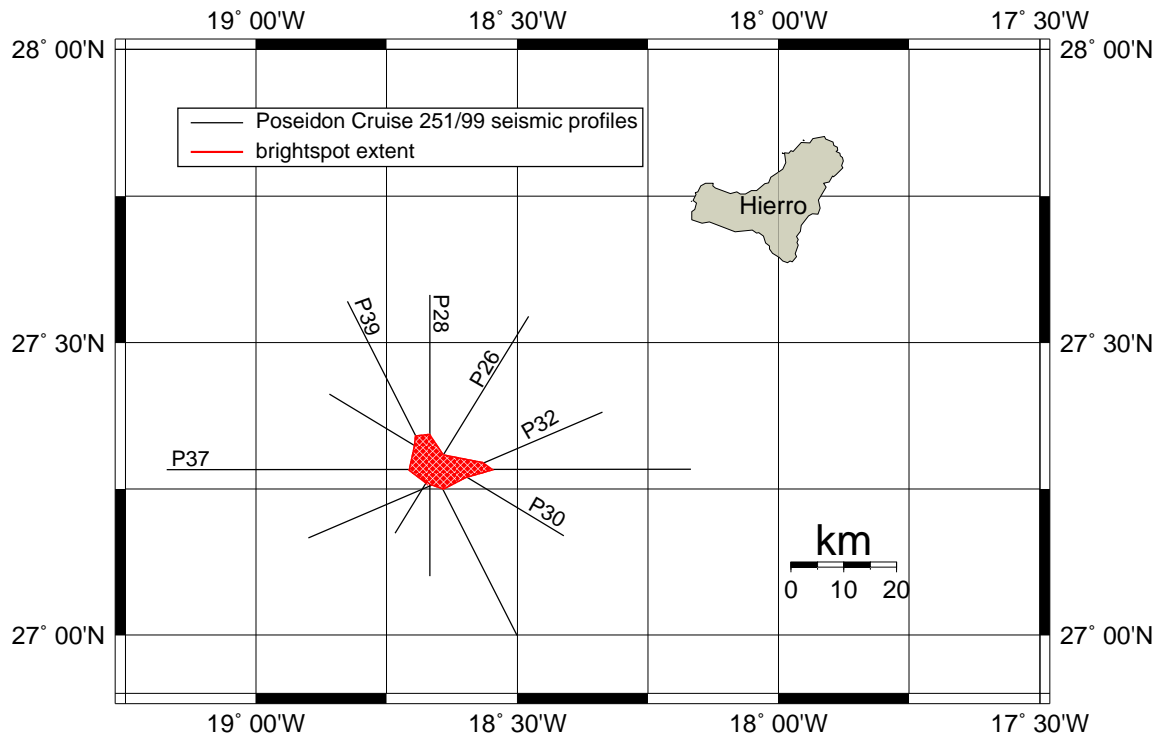

Figure 5.7: *An areal extent of about 100 km^2 has been calculated from mapping the extent of the bright spot reflection on individual profiles based on navigational data.*

5.4 Summary of bright spot properties

The pronounced bright spot reflections imaged in the Southern Canary show some similarities, but also major differences to bright spots observed in exploration industry and deep crustal seismic sections. The observed properties are summarized in the following:

- The bright spots (B.S.) are characterized by unusual strong reflection amplitudes against embedding sedimentary and volcaniclastic sequences (debris flow and slump deposits).

- B.S. in the Southern Canary Basin occupy areas between 25 and 100 km^2. From this, a relation to long submarine lava flows or debris flow deposits can be excluded.

- B.S. are embedded in sediments of approximate Middle Miocene age.

- B.S. are imaged in distances of 60 to 80 km from the shoreline of the islands.

- B.S. occur 400-500 ms and 900 ms below seafloor, embedded in almost transparent sedimentary sequences.

- B.S. do not crosscut the stratigraphic sequences, distinguishing them clearly from bottom-simulating-reflectors (BSRs). They strictly follow the sedimentary bedding.

- No time-sag anomaly is observed on reflections beneath the bright spots, indicating a thin reservoir.

In the following section the properties of the bright spot reflections with respect to its elastic parameters will be analyzed from multichannel reflection seismic and ocean-bottom-hydrophone data.

Chapter 6

Characterization of Seismic Bright Spots

6.1 Instantaneous amplitude and phase

In the *Encyclopedic Dictionary of Exploration Geophysics*, Sheriff (1991) defines a hydrocarbon indicator as a "measurement which indicates the presence or absence of a hydrocarbon accumulation". Bright spots and polarity reversal are examples of such indicators. Although Sheriff points out that all indicators can have causes other than a hydrocarbon accumulation, he concludes that a case is generally strengthened when several indicators point to the same conclusion. The phase of the bright spot reflection is analyzed on prestack MCS shotrecords and bright spot reflection amplitudes are mapped on single-channel seismic sections. Calibration of the seafloor reflection amplitude at ODP site 956 enables estimation of absolute reflection coeffcients.

6.1.1 MCS prestack shotrecords

An estimation of the wavelet character and associated phase can quite often be visually identified at distinctive reflection interfaces. This includes the water bottom on marine data, the top and bottom of thick stratigraphic units, regional events, and direct hydrocarbon indicators (Roden & Sepúlveda, 1999). The assumption is that the entire wavelet processed is preserved at clean reflecting interfaces. Prestack MCS shotrecords from line 17/99 provide the direct water wave on records acquired without delay, clean seafloor reflections, and basement reflections to analyze the polarity of the bright spot reflection. Analysis is performed on raw shotrecords with no alteration of the data with respect to processing (e.g., band-pass filtering and deconvolution). A clear image of the source wavelet is identified at the undisturbed seafloor reflection on shotrecord 560 (Fig. 6.1a) and on the direct water wave (Fig. 6.1b). Both are recorded from firing a single 2.0 l (120 in^3) airgun on R/V *Poseidon* cruise 251. The source wavelet consists of three lobes: a leading peak (black), a trough (white) and finally a peak (black). In the following this sequence is referred to as **peak-trough-peak** amplitude sequence. This positive polarity is clearly identified at the basement reflection in shotrecord 482 (Fig. 6.1c). The reversed polarity of the bright spot reflection is clearly observed in Figs. 6.1a and 6.1d, where the final lobe of the wavelet is a well-developed

trough, which is opposite of the peak observed at the source wavelet. The main lobes of the bright spot reflections are characterized by a **trough-peak-trough** amplitude sequence. This reversal is also clearly evident when comparing the first bubble pulse of the bright spot reflection (Fig. 6.1a) with the first bubble pulse of the direct water wave (Fig. 6.1b).

Since no indication of a noticeable lower boundary reflection below the bright spot reflection is observed, a thin layer of first order discontinuities at or below tuning thickness or a higher order lower boundary reflection, i.e., a gradient zone, might be considered. An amplitude increase resulting from constructive interference of the top and the bottom reflection from a bed of a quarter wavelength thickness is called tuning. A thin bed is defined as a situation, where the thickness of beds under consideration is less than $\lambda/4$ (Sheriff & Geldart, 1982). The initial lobe of the bright spot reflection in shotrecord 566 (Fig. 6.1d) is identified as a small peak (black), followed by a dual-trough, which suggests an interference pattern between a weak positive reflection followed by a strong negative reflection caused by a large negative acoustic impedance contrast. The initial peak suggests a positive reflection of approximately the same strength as the seafloor reflection, while the strong final negative lobe of the bright spot reflection suggests a reversed polarity reflection much stronger than the seafloor reflection. These observations do not agree with a 'sill-model', e.g., the regional marker horizon at ODP site 956, where the bed is assumed to produce a positive reflection at the top and a negative reflection at the bottom of approximately the same amplitude. Sheriff & Geldart (1982) presented modeling of the amplitude of the interference reflection from the top (positive) and the base (negative) of a sand layer (similar to 'sill-model'). The maximum constructive interference amplitude at the tuning thickness was calculated to be about 160 percent of the wavelet amplitude. From this, the bright spot reflection indicates generation from a small positive reflection (top of reservoir), followed by a stronger negative reflection (gas layer) with a velocity gradient defining the base of the reservoir.

6.1.2 Amplitude mapping

The strong reflection amplitude characterizing the bright spots has been mapped along seismic line 28/97 and is compared to the seafloor reflection amplitude and the reflection amplitude of the regional marker horizon in the vicinity of ODP site 956. The analysis is performed on single-channel sections in order to prevent amplitude alteration introduced by stacking. Any errors which might be introduced by phase rotation of the source signal during penetration of the sedimentary column, are considered by extracting the amplitude from the envelope trace rather than from the measured seismic trace. The envelope of a trace at any given time is that maximum value that the trace can have under a constant-phase rotation. The envelope is easily found, when rotating the trace incrementally from 0° to 360°. At any time, the maximum value that the trace assumes during the phase rotation is the envelope, also called the instantaneous amplitude (Taner & Sheriff, 1977; Barnes, 1998).

Figure 6.2(b) shows the neartraceplot (channel 1) from bright spot location V, south of Tenerife. The maximum amplitude of the envelope has been picked in a 70 ms window around the bright spot reflection, which does not include the bubble pulse se-
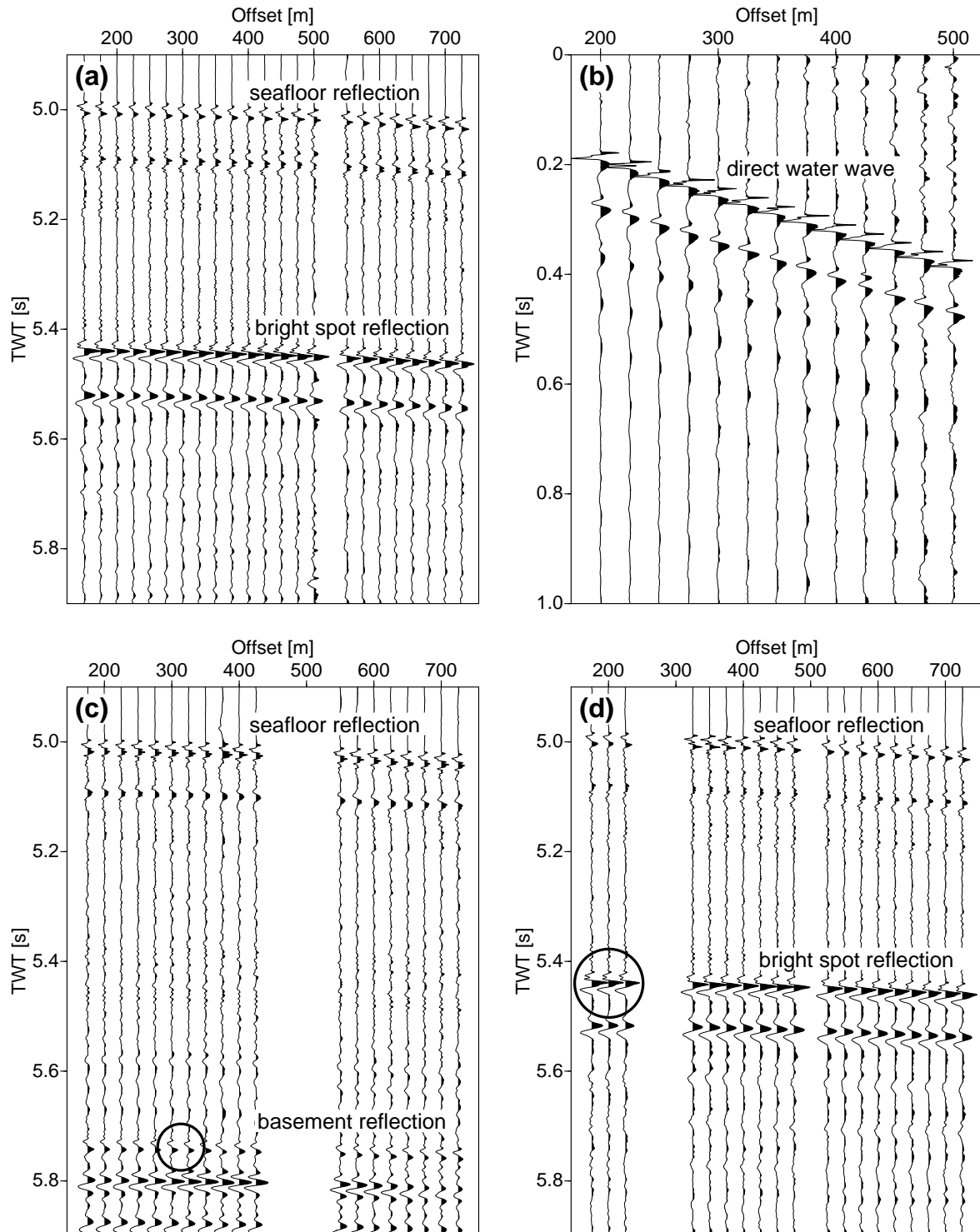
Figure 6.1: *A clear phase reversal of the bright spot reflection is imaged on unprocessed prestack MCS shotrecords by comparison against the well-defined source wavelet. (a) shotrecord 560 showing a clean seafloor reflection and the bright spot reflection. (b) the direct water wave showing the source signature. (c) shotrecord 482 showing a clean positive reflection from the basement, and (d) the bright spot reflection indicated as interference pattern on shotrecord 566.*

quence. The maximum instantaneous amplitude of the seafloor reflection has also been picked in an 70 ms window. The picked amplitudes are displayed in Fig. 6.2(a). The thin line shows the amplitude of the seafloor reflection, which is very smooth with an average amplitude of about 75. The bright spot amplitude (bold line) clearly defines the position and the terminations of the anomalous reflection response; latter indicated by a sudden decrease in reflection amplitude within a few shotpoints. The average ratio between bright spot and seafloor reflection amplitude, calculated between shotpoint 40 and 240, is about 1.9. An additional amplitude anomaly between the bright spot and the seafloor (shotpoint 180 to 260) at ~5.0 s TWT causes a decrease in the mapped bright spot reflection amplitude due to reduced transmission of energy, while the sequence of increased reflectivity starting at the western end of the section extending up to shotpoint 140 at ~5.0 s TWT shows similar effects. Minimum transmission losses are observed between shotpoint 140 and 180.

The limited areal extent of bright spot location II, south of El Hierro island, has already been mapped on several stacked profiles in section 5.2. The single-channel section from line 28/97 in Fig. 6.2d shows the bright spot embedded in a sedimentary sequence of low reflectivity at ~5.4 s TWT. The bright spot reflection is interrupted by a zone of reduced reflectivity at shotpoint 150, which is interpreted as fault affecting the entire sedimentary column from below the bright spot up to the seafloor. The amplitude of the seafloor reflection in Figure 6.2c (thin line) is undulating around an average value of about 90, which is slightly higher than at bright spot location V and might be related to increased reflectivity due to volcaniclastic deposits (debris flow). The bright spot reflection amplitude (bold line) again clearly defines the position and the terminations of the bright spot. The fault is clearly characterized by the strong reduction of reflection amplitude, which might be related to increased reflection angles that are not covered from the short hydrophone streamer. The bright spot reflection amplitude drops down to below the level of the seafloor amplitudes outside the bright spot. An average amplitude ratio between bright spot and seafloor reflection amplitude of about 2.2 is calculated between shotpoint 60 and 240.

The strong reflection amplitude of the bright spots is compared with reflection amplitudes from the regional marker horizon at ODP site 956, which represents a layer of increased acoustic impedance against the embedding sediments (ref. section 2.5.1). The neartrace section in Figure 6.3b shows the target reflection immediately above 4.8 s TWT. The reflector appears much less-continuous than the bright spot reflections. The amplitude of the seafloor reflection (Fig. 6.3a, thin line) is undulating around an average amplitude value of about 100. The target reflection (bold line) shows slightly increased reflection amplitudes compared to the seafloor reflection. The average amplitude ratio in this section is about 1.1, which significantly distinguishes this reflection event from the bright spot reflections. Calibration of amplitudes at the seafloor reflection coefficient of about 0.2 at the ODP site yields an average reflection coefficient for the regional marker horizon of about 0.2 and for the bright spot reflections of about 0.4, based on the calculated amplitude ratios. This amplitude analysis and the phase reversal observed on shotrecords provide additional indications for the bright spots originating from a pronounced low acoustic impedance contrast (such as a gas reservoir).
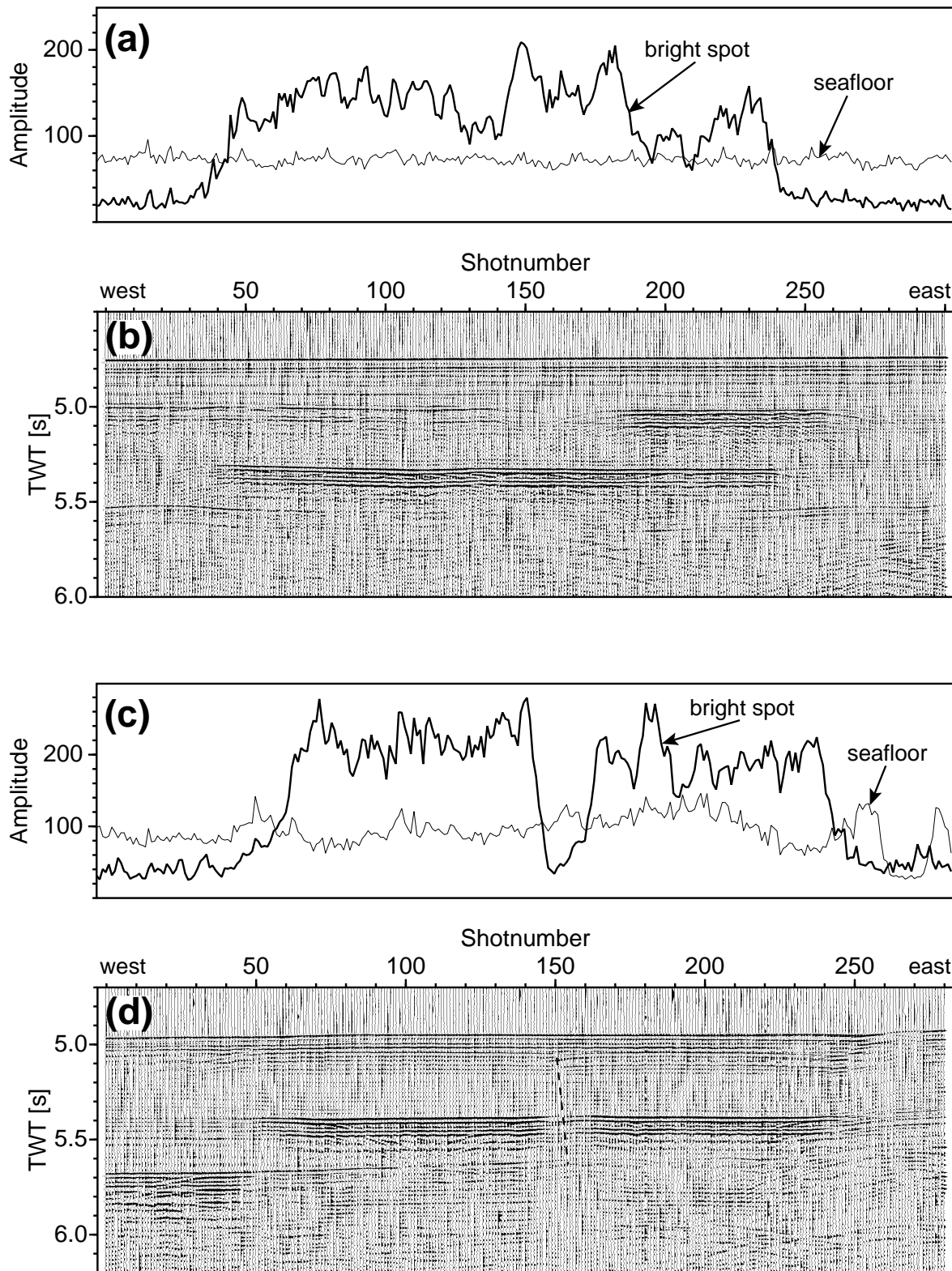
Figure 6.2: *Mapping of the instantaneous amplitude of the bright spot against the seafloor reflection demonstrate the local character and clear lateral terminations of the bright spots. (a) and (b) Bright spot V, line 28/97. (c) and (d) bright spot II, line 28/97. A fault is indicated at shotpoint 150. Shotpoint spacing is 25 m.*
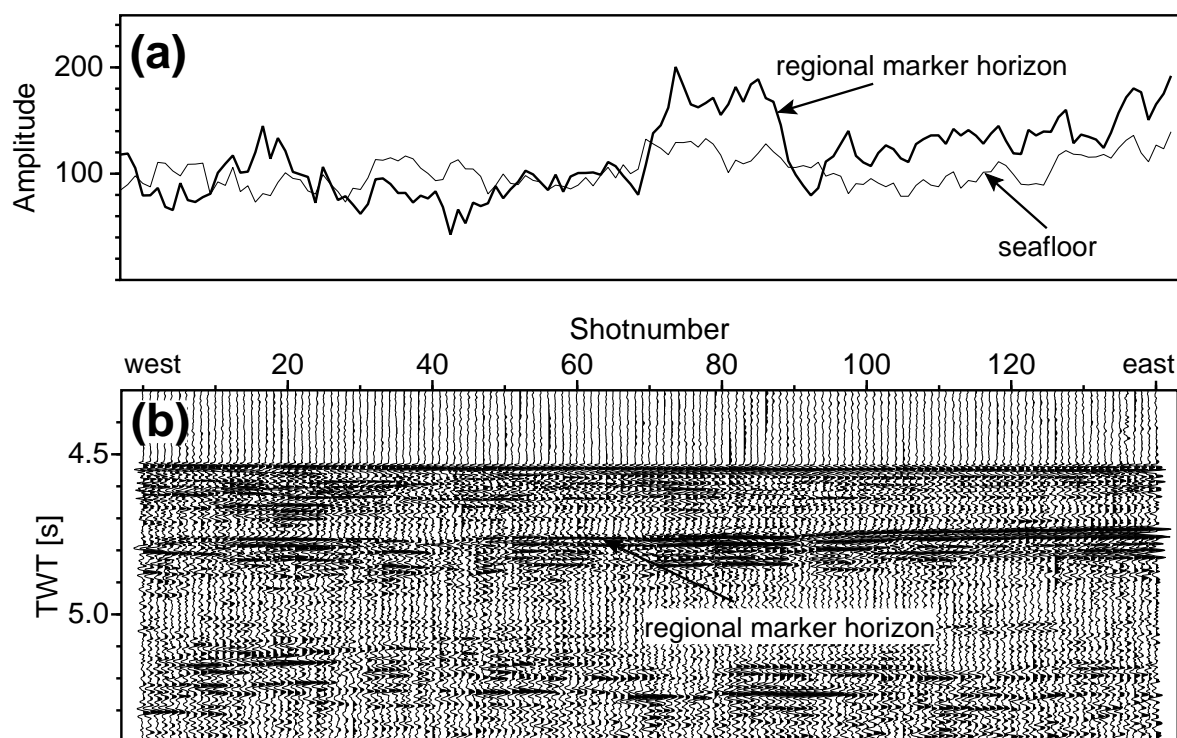
Figure 6.3: *The reflection amplitude of the regional marker horizon at ODP site 956 shows a similar amplitude level as the seafloor reflection. The seafloor reflection amplitudes have approximately the same magnitude at the ODP site and at the bright spot locations (seafloor reflection coefficient $R \approx 0.2$).*

6.2 Semblance velocity analysis

The major factor involved with hydrocarbon indicators is the effect on velocity. As deep MCS data provide poor resolution in velocity analysis accompanied by high ambiguity, ocean-bottom-hydrophones have been deployed at the bright spot locations to record wide-aperture reflections. This method provides long shot-receiver offsets for a good resolution in the velocity spectrum to resolve velocity anomalies and to obtain a regional velocity-depth function. OBH records can be used for stacking velocity analysis, if reflections from the subsurface can be approximated as originating from flat interfaces and as long as the moveout is hyperbolic. This is roughly true at the bright spot locations, so the shotpoint and the receiver can be considered as located midway in the water column, providing a symmetric acquisition geometry similar to CMP gathers.

A significant disadvantage of OBH records is the occurrence of a strong first arrival, consisting of the high-amplitude direct arrival and the seafloor reflection, which generally masks shallow sedimentary reflections (Fig. 6.4, top). This is particularly noticeable when no tuned airgun-array is used as during both R/V *Poseidon* cruises. Application of predictive deconvolution to suppress the bubble pulse sequence was not successful, which obviously was due to the trace-to-trace variation of the source signature and the dominating amplitudes of the first arrival. The bubble pulse is naturally dominated by low frequencies, while primary reflections have a much broader bandwidth. Therefore the application of a high-pass filter of 25 to 100 Hz could reduce the bubble pulse slightly. This was followed by subtraction of an average estimate of the first arrival. For this purpose, the first arrival was aligned horizontally and an average trace was calculated from a horizontally moving window consisting of 100 traces. The average trace only contains amplitudes of the first arrival wavelet, since this event occurs at the same traveltime on every trace, while primary reflections are suppressed due to their moveout and hence destructive interference in this window. This new method led to a significant improvement of the signal-to-noise ratio. After suppression of the first arrival, OBH record 09 has been correlated with MCS line 20/99 (Fig. 6.4, bottom). Shallow reflection events can be correlated from the MCS section (left) through large offsets in the OBH panel (right). The first arrival in the OBH section has been aligned horizontally. Therefore, all primary events are characterized by a moveout and can easily be identified. Seven sedimentary reflections (R1 to R7), the seafloor reflection (SF), the bright spot reflection (BS), and the basement reflection (BM) are indicated in the MCS section and can easily be traced through the OBH panel. Again, the reversed polarity of the sedimentary reflections (black-white-black) against the bright spot reflection (white-black-white) is clearly discernible.

Semblance-based velocity analysis has been performed on OBH record 09, line 20, and OBH 13, line 37 (Fig. 6.5). The first arrival in the OBH panels were suppressed. Then the data are transformed from the offset versus two-way time domain (right) to the stacking velocity versus two-way zero-offset time domain (left). Maximum coherencies in the velocity spectrum can clearly be correlated with pronounced hyperbolic trajectories in the OBH panels. The bubble pulse in OBH record 13 appears much stronger than in OBH record 09. This is particularly obvious at the bright spot reflection. The simultaneous firing of the 2.0 and 0.85 l airgun during acquisition of record 09 leads to a destructive interference of the individual bubble pulses due to their differ-
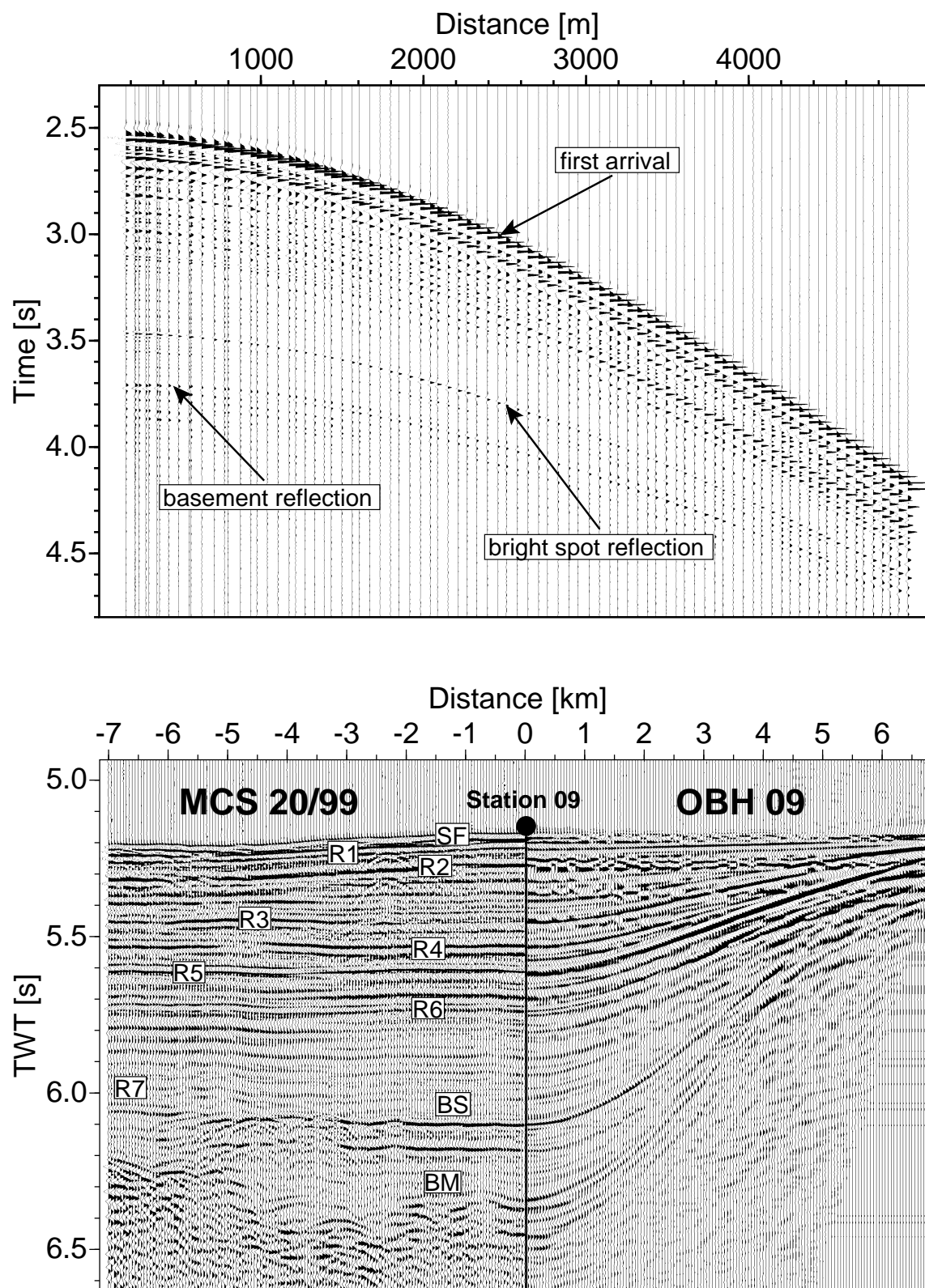
Figure 6.4: *OBH 09, line 26, shows the high-amplitude first arrival masking shallow sedimentary reflections (top). After subtraction of an average estimate of the first arrival, shallow sedimentary reflections can be correlated from the MCS through the OBH section (bottom).*
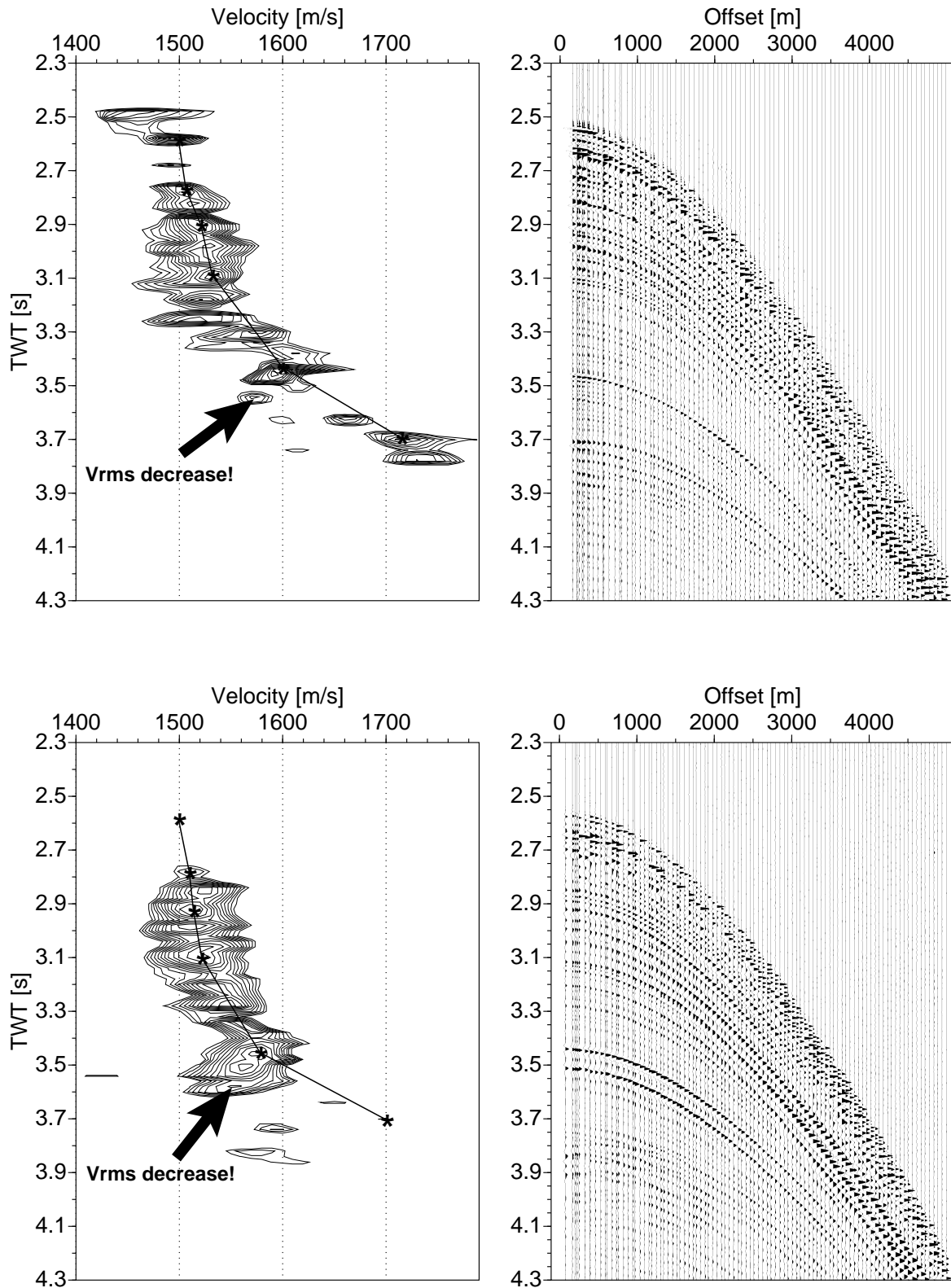
Figure 6.5: *Velocity spectra are plotted as contour plots for OBH 09, line26 (top) and OBH 13, line 37 (bottom). An average estimate of the first arrival has been subtracted in the OBH panels. The noticable decrease in stacking velocity immediately beneath the bright spot reflection at ~ 3.45 s is caused by the bubble pulse sequence. A V_{RMS} decrease related to the reservoir, would be masked by this effect.*

49

ent bubble periods (Dragoset, 2000). In contrast, the simultaneous firing of two 0.85 l airguns during acquisition of OBH record 13 leads to an amplification of the bubble pulse. Based on the maximum stacking power, the following picks for a stacking velocity function are made from the velocity spectrum of OBH station 09 (Fig. 6.5, top): 1500, 1505, 1513, 1530, 1600, and 1720 m/s corresponding to 2.55, 2.80, 2.90, 3.10, 3.45, and 3.70 s two-way zero-offset time. These picks only include the major distinct coherence maxima that can be correlated with pronounced reflection hyperbolas in the OBH panel. A minor coherence maximum is observed immediately below the bright spot maximum at ~3.55 s, that clearly indicates a reduction in stacking velocity. Since this maximum cannot be correlated with a pronounced reflection immediately below the bright spot reflection, this event is not considered for the following calculation of interval velocities. Above the bright spot reflection, the stacking velocity steadily increases with depth. The semblance velocity analysis for OBH 13, line 37, shows similar stacking velocities in the sedimentary column. The following picks are made for this velocity spectrum: 1500, 1505, 1510, 1525, 1590, and 1700 m/s corresponding to 2.55, 2.80, 2.90, 3.10, 3.45, and 3.70 s two-way zero-offset time. The seafloor does not show a coherence maximum, which might be caused by destructive interference of the seafloor reflection with residual energy from the direct arrival. The less-distinctive basement in the OBH panel does not produce a significant coherence maximum either. The basement at about 3.7 s appears weak and is composed of several weak diffraction and reflection hyperbolas, possibly related to its faulted character, which does not stack in phase. The velocity spectrum from OBH 13 shows the reduction of stacking velocity immediately beneath the bright spot as well.

The reduced stacking velocities in the spectra are related to the bubble pulse sequence of the seismic signal, and thus do not indicate reduced velocities in the reservoir. Anyhow, these events might mask a true velocity reduction. Simple vertical Dix inversion has been applied to convert the stacking velocities to interval velocities in order to obtain a regional seismic interval velocity model as shown in Figure 6.6. Both models show the bright spot at a depth of about 800 m below seafloor. The bright spot reflection is represented by a velocity increase only, because a velocity decrease is not resolvable from stacking velocities. These models indicate interval velocities of about 2100 m/s above the bright spot and about 2900 m/s between bright spot and basement. An increase of velocities above 4000 m/s at the basement is constrained by traveltime inversion applied to these OBH data (Papenberg, 2000), indicating layer 2A of the oceanic crust (Keary & Brooks, 1991).
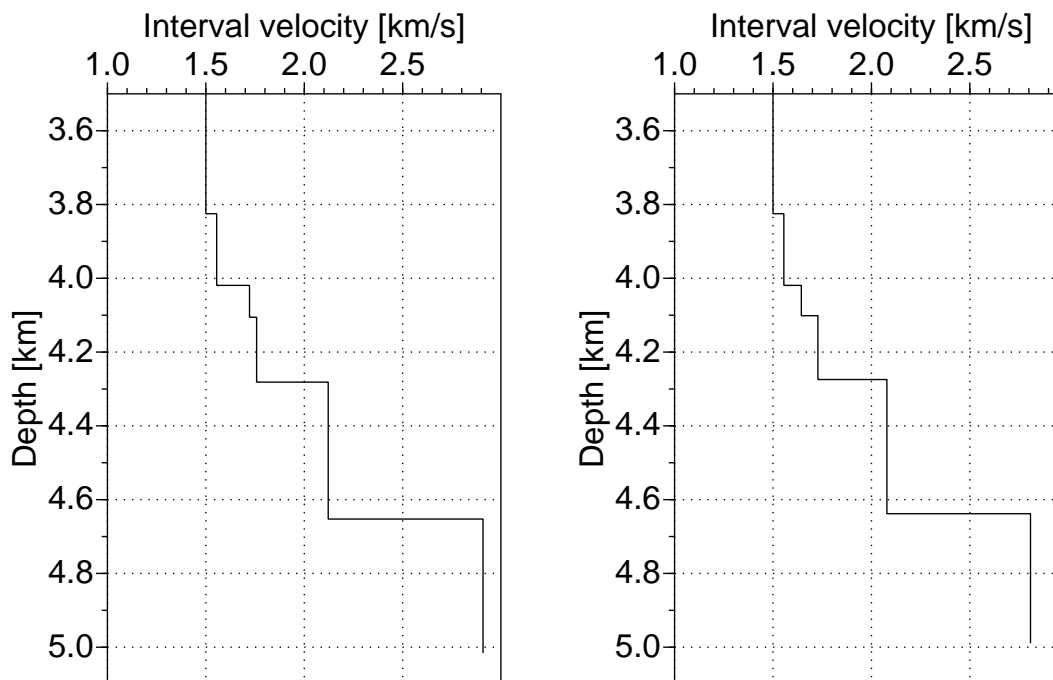
Figure 6.6: *A regional seismic interval velocity model is obtained from semblance-based velocity analysis of OBH 09 (left) and OBH 13 (right) southwest of El Hierro island. Minor differences between these models might be related to slightly dipping horizons.*

6.3 Amplitude-versus-offset analysis

Acoustic impedance contrasts are well resolved from near-offset reflections in the MCS data, but provide incomplete information about petrophysical properties of the subsurface. Extraction of a second parameter related to shear waves, such as Poisson's ratio, is necessary. For this purpose amplitude variation with offset (AVO) analysis is applied to the wide-aperture OBH data. The range of incidence angles for conventional AVO studies carried out on CMP gathers is typically less than 30° (Castagna, 1993), while OBH geometry can provide angles of incidence beyond 80°. The main theory behind AVO is based on the effective response of compressional waves (P-wave) versus shear waves (S-wave). As a seismic wave travels within the pore space of a gas saturated reservoir rock, the P-wave velocity (Vp) decreases rapidly. The S-wave velocity (Vs), on the other hand, increases linearly. The effective decrease in the Vp/Vs ratio, which is directly related to Poisson's ratio, causes changes in the relative amplitude of seismic reflections as a function of the angle at which a wave strikes the gas saturated reservoir rock.

In exploration geophysics, AVO is considered as direct hydrocarbon indicator and has been a primary tool for predicting a reservoir's rock type and pore-fluid content for more than 17 years (Ostrander, 1984; Estill & Wrolstad, 1993; Hilterman *et al.*, 2000). More recently, AVO has been used to evaluate the presence and amount of free gas below bottom simulating reflectors, for example at the Blake Ridge (Ecker *et al.*,

1998) and offshore Oregon (Andreassen *et al.*, 1997). The aim of this AVO analysis is to distinguish between a negative polarity reflection (reservoir-model) and a positive polarity reflection (sill-model) based on their significantly different AVO behavior at large offsets. The amplitude build-up towards the critical angle and the phase change beyond can be used to identify positive polarity reflections (Castagna, 1993). In contrast, a reservoir-model characterized by constant or decreasing Poisson's ratio and decreasing P-wave velocity is characterized by high zero-offset reflection coefficients which slightly decrease at intermediate offsets and then increase slightly during the approach of 90° incidence angle (Sheriff & Geldart, 1982; Katzman *et al.*, 1994).

AVO analysis is performed on OBH records 03 and 04 at bright spot location II, south of El Hierro island (Fig. 6.7). The bright spot reflection is imaged at ∼400 ms bsf, where embedding sediments appear nearly transparent. This bright spot reflection can much better be approximated as horizontal reflection interface than the slightly undulating bright spot reflection at location VII. The shot point distance of 25 m provides a denser sampling of the offset range, favouring this location for AVO analysis. The shooting direction was from north to south and reflections from heading towards the OBHs are considered for analysis. OBH record 03 is shown in Fig. 6.8. The bright spot reflection hyperbola is clearly imaged up to offsets of 6000 m, where it interferes with the high-amplitude first arrival. The interference with the bubble pulse sequence from the first arrival starts at offsets between 3000 and 4000 m. No near-surface sedimentary reflections are masked by the first arrival as indicated in the MCS section. Therefore, in order to avoid any additional processing noise introduced to the OBH panel, the first arrival is not suppressed for AVO analysis.

An amplitude preserving data processing sequence has been applied to the wide-aperture OBH data to compensate for overburden effects. This includes detailed velocity analysis and correction for spherical divergence and anelastic absorption. The OBH data are of good quality and the overburden can be approximated by one single horizontal layer. Therefore the overburden velocity structure has been derived from the $X^2 - T^2$ method, which can give accurate velocities within a few percent (Telford *et al.*, 1990). This analysis (Fig. B.1) demonstrates the hyperbolic moveout of the bright spot reflection and yields a velocity gradient starting from 1500 m/s at the seafloor increasing to 2200 m/s at the bright spot depth. This velocity model was then implemented in the FORTRAN program **ANRAY** (Gajewski & Pšenčik, 1990), where ray-tracing has been applied to derive the relationship between offset, arrival time, and incidence angle. The observed traveltime curve is well represented by traveltimes calculated from this model (Fig. B.2). The coefficients for spherical divergence correction have been determined from the length of the wave propagation path. Anelastic absorption has been corrected with an effective quality factor Q_e of 200, appropriate for shallow unconsolidated sediments (Hamilton, 1972). Another advantage of OBH geometry is that no directivity correction is required, because the experiment approximates a point source and a point receiver.

For this experiment, medium properties are assumed to vary only with depth (1-D). Reflector curvature and the spreading of reflection points along the bright spot might introduce minor inaccuracies. Event tuning, caused by differential traveltimes between two closely spaced reflections, can be expected for the bright spots. Differential tuning effects will therefore occur from near to far offsets. Thin beds, such as many gas sands,
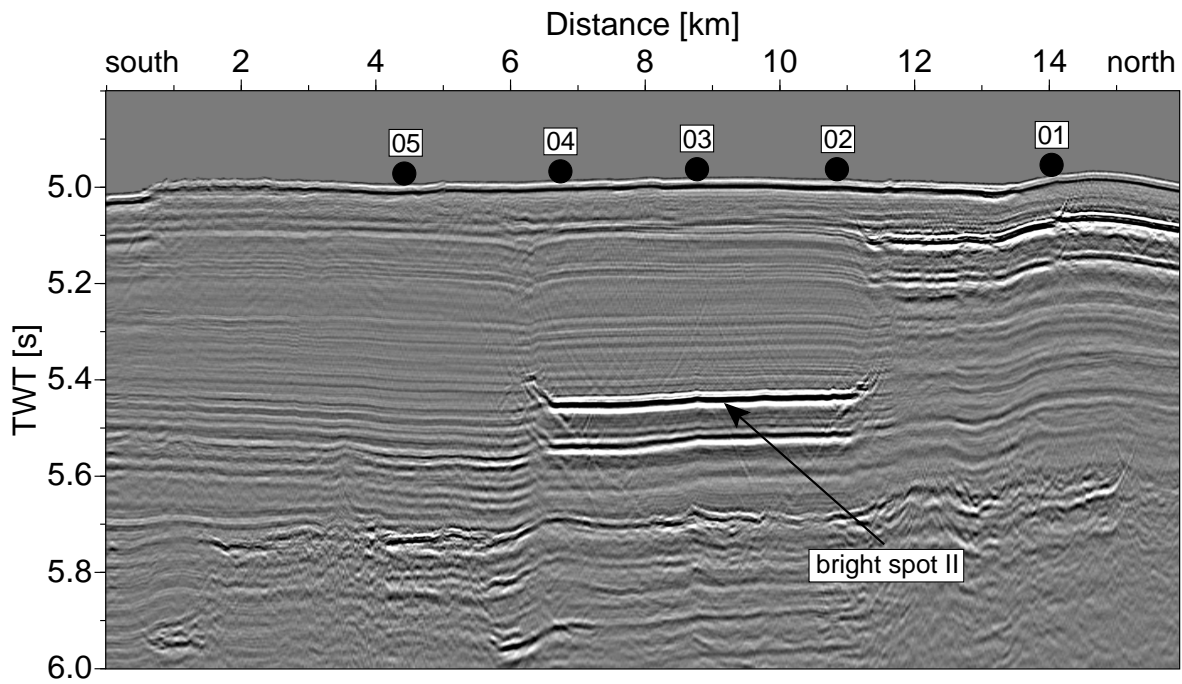
Figure 6.7: *Imageplot showing a stacked and migrated section of seismic line 14/99. The locations of OBH 01 to 05 are indicated. OBH 03 and 04 have been selected for AVO analysis.*
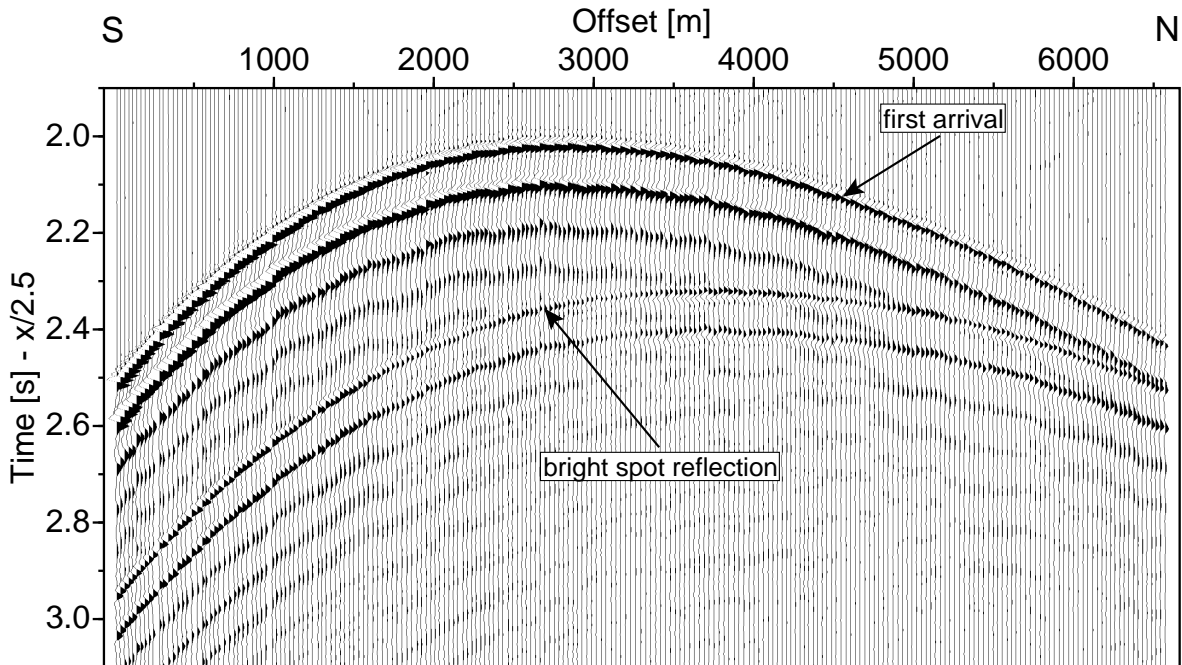

Figure 6.8: *Unprocessed record of OBH 03, line 14/99, showing the first arrival and the bright spot reflection. Interference of the hyperbolas occur at offsets beyond 6000 m.*

decrease recorded amplitudes with increasing offset (Ostrander, 1984). However, the trend of an increase or decrease in acoustic impedance and Poisson's ratio across an interface can be consistently resolved.

The travelpaths calculated for seismic rays from the subsurface model for bright spot location II is shown in Figure 6.9. It is evident, that the bottoming points of the bright spot reflection are spread over a distance of about 1 km along the bright spot. Nevertheless, considering positions of the OBH stations and the lateral extent of the bright spot reflection on the stacked section of line 09/99 (Fig. 6.7), the bottoming points does not spread beyond the bright spot reflection, validating the approximation of a 1-D subsurface model. The ray diagram indicates that rays arriving at offsets of about 6 km occur as diving waves rather than reflections from the bright spot interface. This observation can not be considered as very reliable, since minor variations in the overburden velocity model might shift the transition from reflections to diving waves towards higher offsets. Ray tracing provides the relationship between incidence angles at the bright spot interface and source-receiver offsets measured in the data (Fig. 6.10). From this relationship, the OBH geometry provides incidence angles up to about 80°, which is about twice the range of incidence angles provided by traditional AVO studies on CMP gathers.

To evaluate a possible phase change related to reflections beyond the critical angle, reflections observed in OBH 03, line 14, are NMO corrected using the stacking velocity model derived from $X^2 - T^2$ velocity analysis (Fig. 6.11, top). Despite the NMO stretch observed at large offsets, it is obvious that no phase reversal and no major phase changes are present in the bright spot reflection. This is even more distinct in Fig. 6.11 (bottom), where the bright spot reflection has been flattened at zero-offset reflection time to avoid NMO stretch. The main peak of the reflection can be traced throughout the entire section, while the interference with the bubble pulse sequence of the first arrival is indicated by minor variations in the amplitudes of the sidelobes of the reflection as clearly observable at offsets of 3500 m and 4500 m. The absence of a phase change, related to post-critical reflections, and refracted arrivals is considered as an indication for the presence of a negative acoustic impedance contrast at the bright spot.

Amplitudes from the main peak of the bright spot reflection in OBH 03 and 04 have been picked for AVO analysis. In Fig. 6.13 these picks are displayed after correction for spherical divergence and anelastic absorption. Zero-offset reflection amplitudes have been scaled to match a reflection coefficient of about -0.4, which was estimated from amplitude mapping in section 6.1.2. A clear decrease in reflection amplitudes is observed between incidence angles of 0° and 50°. Beyond the minimum, amplitudes increase towards higher incidence angles. There is no indication for a critical angle in the data. The undulations in amplitude around the average trend is related to the alternating constructive and destructive interference with the bubble pulse sequence from the first arrival. This AVO response is characteristic for decreasing P-wave velocity and density across an interface, while Poisson's ratio remains constant or is reduced slightly (Sheriff & Geldart, 1982). Therefore, four Zoeppritz curves for constant Poisson's ratio ranging from 0.3 to 0.45 across an interface are plotted together with picked data in Fig. 6.13. Model parameters for calculation of these curves are shown in table 6.12. The P-wave velocity and density are kept constant for all models to reproduce
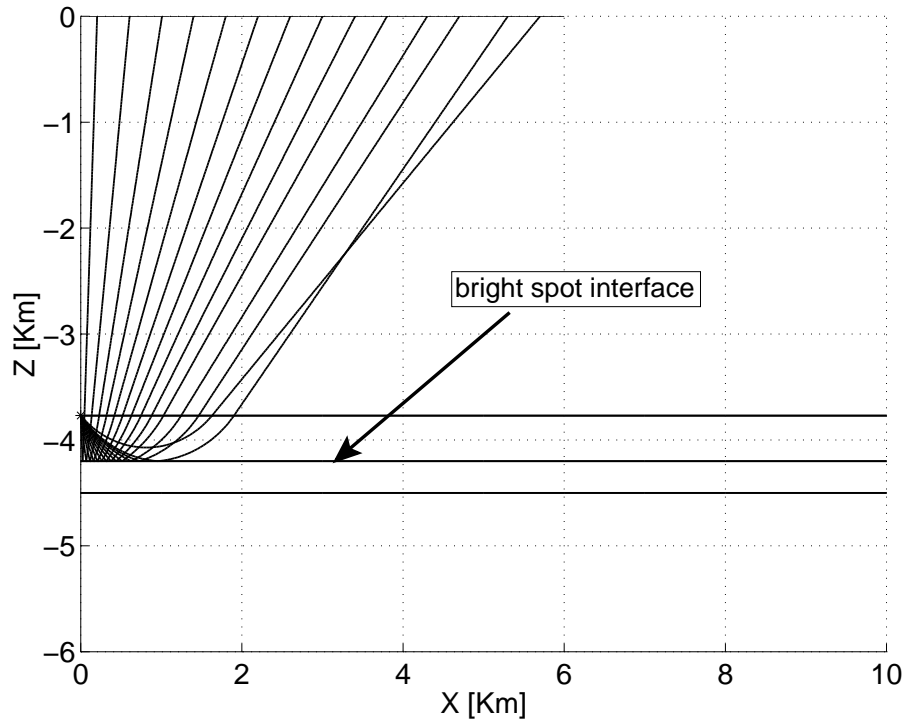
Figure 6.9: *Ray diagram showing that in airgun-OBH geometry, the bottoming points of a 6 km long bright spot reflection are spread out over a distance of about ~1 km along the bright spot.*
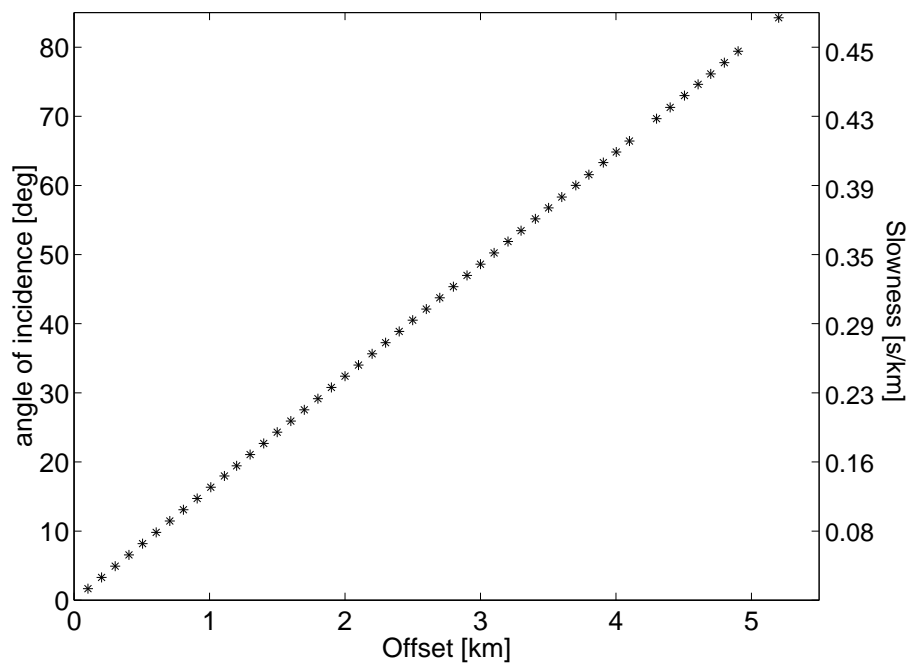

Figure 6.10: *Angle of incidence and slowness (not equidistant) at the turning point of the ray as function of shot-receiver-distance for the bright spot reflection. Reflections observed at offsets of 5 km are associated with incidence angles of 80°. Slownesses are used for waveform inversion.*
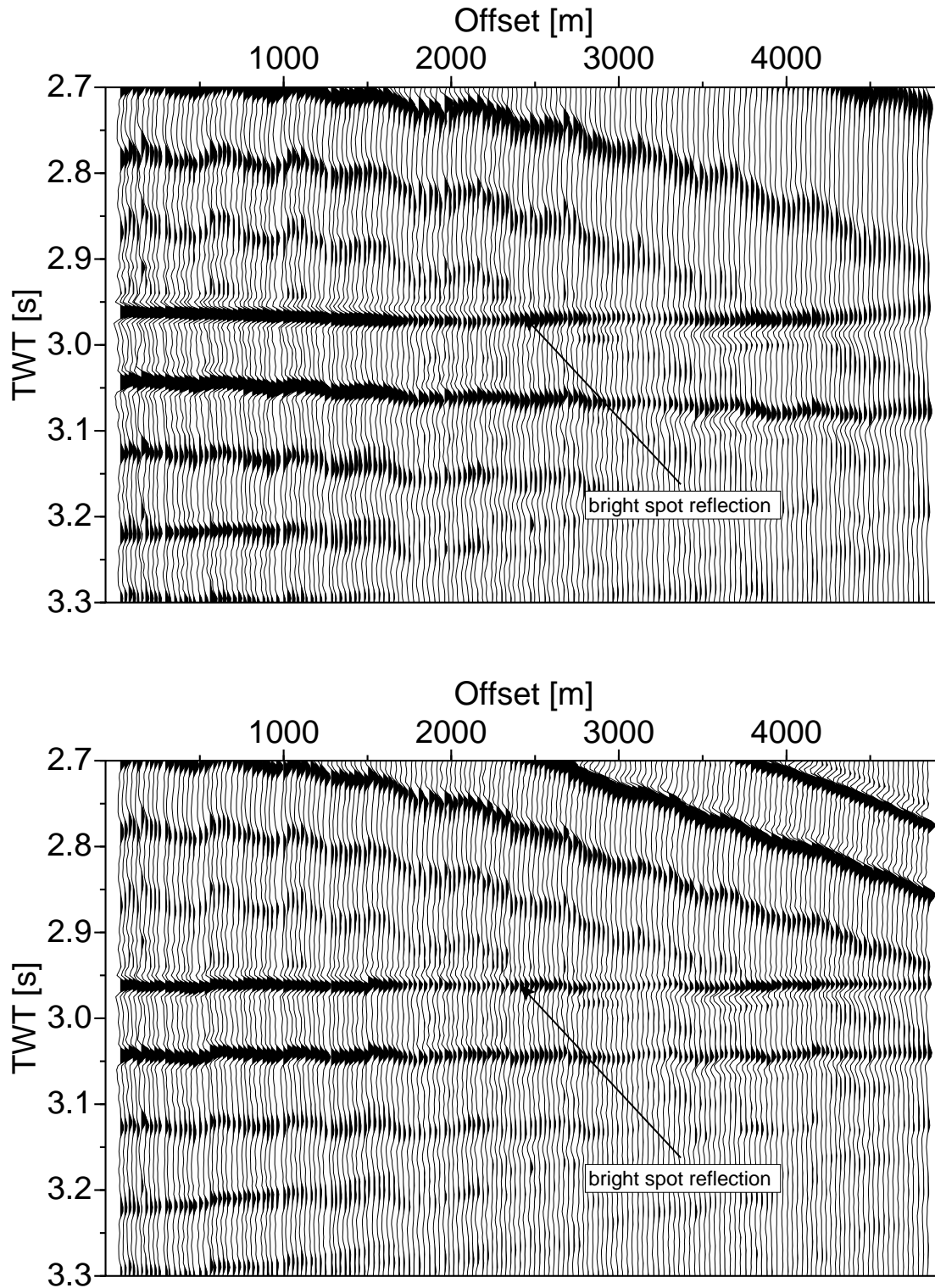
55

Figure 6.11: *Raw data from OBH 03, line 14, corrected for NMO (top) using the velocity model derived from $X^2 - T^2$ velocity analysis. No phase change, critical angle, and refracted arrival is associated with the bright spot reflection, indicating a velocity decrease at the bright spot. This is even more distinct when the bright spot reflection is flattened, thereby avoiding NMO stretch at larger offsets (bottom). A small decrease in amplitudes around offsets of 3000 m is discernible.*

the high zero-offset reflection coefficient. The density is calculated from the P-wave velocity using Hamilton's empirical relationship for soft sediments (Hamilton, 1978). The AVO responses have been calculated using the program **ZOEPIT**, where Rabbel (1987) implemented a form of the full Zoeppritz equations introduced by Červeny *et al.* (1977). The observed data show best fit to theoretical AVO responses with constant Poisson's ratio between 0.30 and 0.35.

The absence of a critical angle and associated phase change in the observed AVO data indicate the presence of a low-velocity zone at the bright spots. A significant reduction in Poisson's ratio, indicative for significant amounts of free gas, is not resolved. In terms of Rutherford & Williams (1989), this type of AVO response is considered as Class III reservoir due to high zero-offset reflection coefficients and no major changes in amplitude from near to far offsets.

Figure 6.12: *Model parameters for calculation of theoretical AVO responses from Zoeppritz equations*

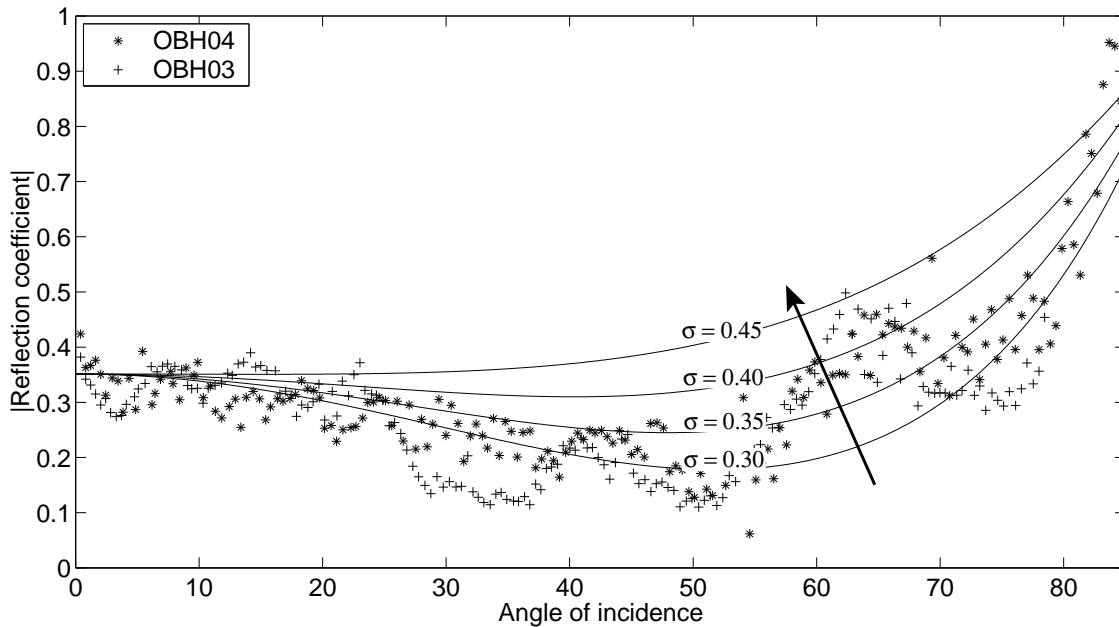| Upper medium				Lower medium			
σ	V_p	V_s	ρ	σ	V_p	V_s	ρ
0.45	2.2	0.7	2.3	0.45	1.3	0.4	1.8
0.40	2.2	0.9	2.3	0.40	1.3	0.5	1.8
0.35	2.2	1.1	2.3	0.35	1.3	0.6	1.8
0.30	2.2	1.2	2.3	0.30	1.3	0.7	1.8

Figure 6.13: *Amplitude versus offset response picked from OBH 03 and 04, south of El Hierro island. Comparison with four Zoeppritz curves for constant Poisson's ratio ranging from 0.30 to 0.45 across the interface indicate best fit between 0.30 and 0.35. The arrow indicates increasing Poisson's ratio.*

6.4 Full waveform inversion

Strong evidence for the presence of a low acoustic impedance zone beneath the bright spots has been presented in the previous sections: steep-angle amplitude and phase considerations as well as wide-angle semblance and amplitude-versus-offset analyses. In this section, the AVO behavior and the waveform of the bright spot reflection for the full range of incidence angles will be considered when applying 1-D full waveform inversion. The inversion scheme is implemented in the frequency-slowness domain, where velocities are estimated by minimizing the sample-by-sample waveform misfit between observed data and reflectivity synthetic data using a conjugate gradient optimization sheme (ref. Methods). The P-wave velocity from a viscoelastic model is updated during inversion, assuming that the main reflection characteristics observed can be assigned to variations in V_p only (e.g., gas, volatiles).

The acquisition of wide-aperture reflections up to incidence angles of 90° is the major advantage of OBH over standard MCS/CDP geometry in deep-water environments. This section will discuss whether the spreading out of reflection points over the bright spot or the shot-to-shot variation of the source signature will have an impact on the quality of the inversion results. Several examples on application of 1-D full waveform inversion on MCS data have been presented (Singh & Minshull, 1994; Collier & Singh, 1997; Singh, 1993; Pecher, 1995), but this inversion scheme has only once been successfully applied to OBH data. Korenaga et al. (1997) applied this technique to determine the seismic origin of BSRs on the Blake Ridge and the Carolina Rise, on the southeastern U.S. continental margin, where indications for varying amounts of free gas below bottom-simulating-reflectors were found.

The location selected for application of 1-D full waveform inversion should meet the following criteria: (1) seafloor, bright spot and other major reflections should be sub-horizontal, and (2) their reflection characteristics should be laterally continuous in regions covered by seismic rays. The wide-aperture data require: (1) dense trace spacing to prevent spatial aliasing, (2) consistent source signature, and (3) adequate data extent in the $t - x$ domain to cover the full range of incidence angles. These conditions are at best fulfilled in the OBH experiment across bright spot location II, south of El Hierro island, where 5 hydrophones have been deployed and three seismic lines (14/99 - 16/99) with shot point distances of 25 m were acquired. On line 14/99, three ocean-bottom-hydrophones (02 - 04) are positioned to record the wide-aperture bright spot reflections; two at the outside margin and one at the center of the bright spot (Fig. 6.14). OBH stations 01 and 05 are located outside the bright spot reflection. The reflectivity between seafloor and bright spot is very weak, but horizontally well stratified. The phase reversal of the bright spot reflection against seafloor and other major reflections is obvious. The MCS bright spot reflection amplitude does not vary significantly inline as shown by steep-angle reflection amplitude analyses in Section 6.1.2. In the following, the full waveform inversion scheme is applied to OBH 04.

6.4.1 Data preprocessing

The pronounced bright spot reflection is well imaged at offsets up to 6.5 km in OBH 04 (Fig. 6.15). In order to achieve reliable inversion results, a careful preprocessing of
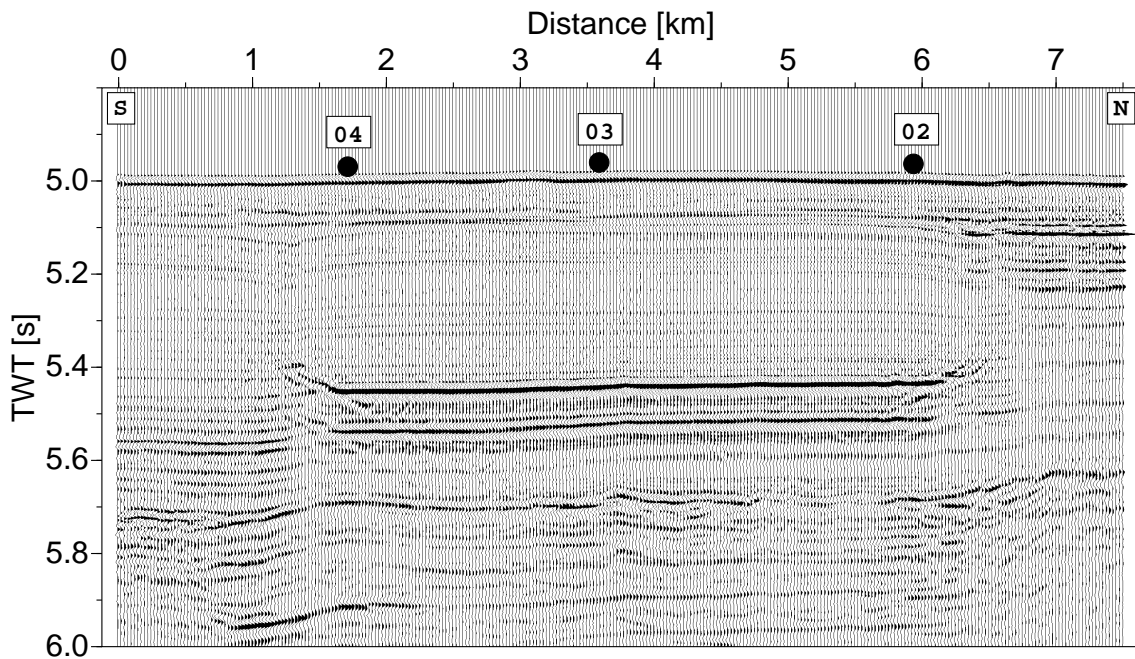
Figure 6.14: *Stacked and time-migrated MCS section from line 09/99 showing bright spot V, south of El Hierro island. No AGC has been applied for display (V.E.=4.5).*
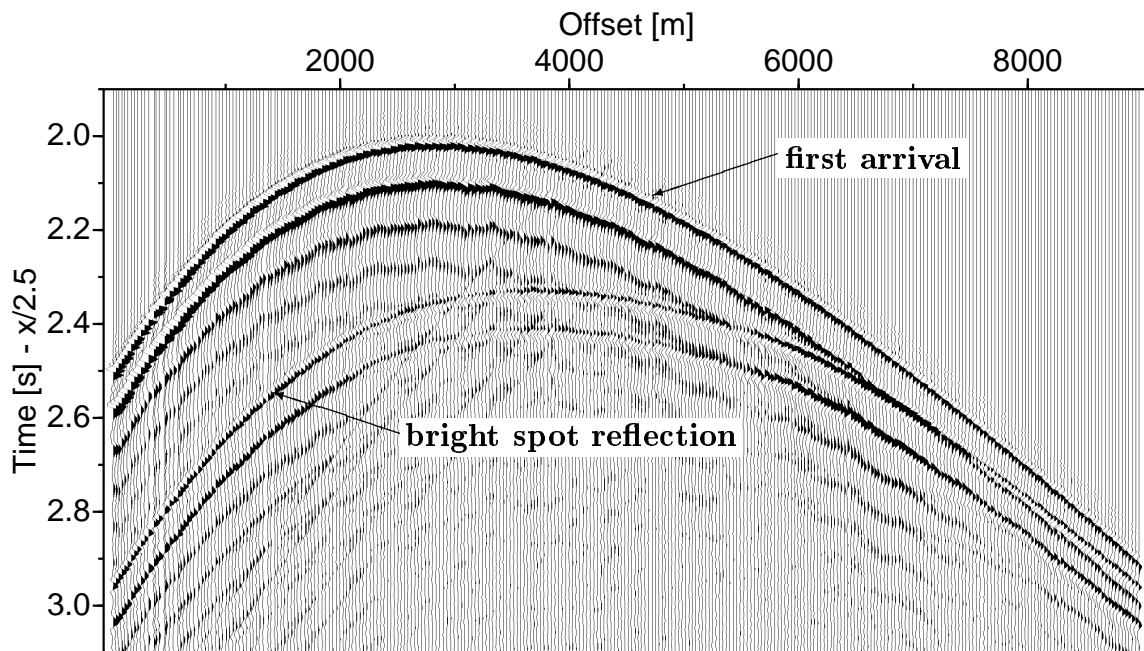

Figure 6.15: *OBH 04, line 14, wide-angle data selected for full waveform inversion (plotted with reduction velocity of 2.5 km/s). Energy from the previous shot crosscuts primary reflections at offsets between 1 and 4 km. Interference of the bright spot reflection with the bubble pulse sequence of the first arrival is obvious.*

the data is necessary. Three steps of preprocessing have been applied prior $\tau - p$ transformation: (1) application of spherical divergence correction, (2) band-pass filtering, and (3) calculation of source-receiver geometry.

To restore amplitude decrease caused by spherical divergence, a simple time-dependent $(v^2 \cdot t)$ correction has been applied (e.g., Yilmaz, 1987). Above the bright spot reflection, the velocity steadily increases with depth; no pronounced reflection anomalies are present. An average velocity gradient of 1.5 s^{-1} was derived applying the $X^2 - T^2$ method (ref. appendix B.1).

To reduce aliasing effects during $\tau - p$ transformation, the frequency content of the data has to be restricted considering the spatial sampling interval (to avoid aliasing entirely, spatial sampling intervals of 10 m are necessary considering the full frequency range up to 100 Hz). Due to the fixed trace spacing at 25 m, a zero-phase Butterworth band-pass filter of 8-50 Hz has been applied. Attempts of simple linear trace interpolation did not produce sufficient results, especially at higher offsets with significant moveout. Therefore, the second and third OBH experiments, with trace intervals of 50 m, are not considered for waveform inversion.

Exact shot point-receiver offsets have been calculated from picked traveltimes of the first arrival and the water depth.

6.4.2   Source wavelet and seafloor reflection coefficient

The common receiver geometry for OBHs implicate that every single trace in the record originate from a different shot with a more or less varying source signature. Furthermore, the high-amplitude direct water wave dominate in the section and its bubble pulse sequence usually masks shallow primary reflections. In this experiment, a single 2 l ($\sim$120 in^3) airgun was utilized. Basically, there are two ways to handle the strong bubble pulse sequence in the inversion scheme: (1) application of predictive deconvolution to suppress the bubble pulse sequence, or (2) including the bubble pulse sequence in the source wavelet for forward modeling. Since deconvolution introduced some numerical noise to the data, the second method was chosen. The data length of 10 s in OBH records enables extraction of the source signature and the seafloor reflection coefficient from the first water column multiple and the primary reflection. The first arrival wavelet is assumed to be the convolution of the source wavelet with the seabed reflectivity series whereas the multiple wavelet results from a polarity reversal at the sea surface and from a second convolution with the seabed reflectivity series (ref. Methods). A spherical divergence correction with a constant P-wave velocity of 1500 m/s has been applied and the wavelet is then extracted in $t - x$ domain as Wiener shaping filter. Primary and multiple reflections from the first trace of OBH 04 are shown in Fig. 6.16a. The extracted source signature (Fig. 6.16b) includes the primary pulse and the first five bubble pulses. After the fifth bubble pulse, the source signature is tapered. Comparison between extracted source wavelet and primary reflection (Fig. 6.16c) shows that the source clearly resembles the shape of the primary reflection, which point out the predominating effect of the direct water wave in OBH records with respect to amplitude and phase, and the negligible influence of the distance between hydrophone and seafloor ($\sim$2 m). Wavelets from the first eight traces have been extracted for stability considerations (Fig. 6.16d). Here, it is important to notice the small variation
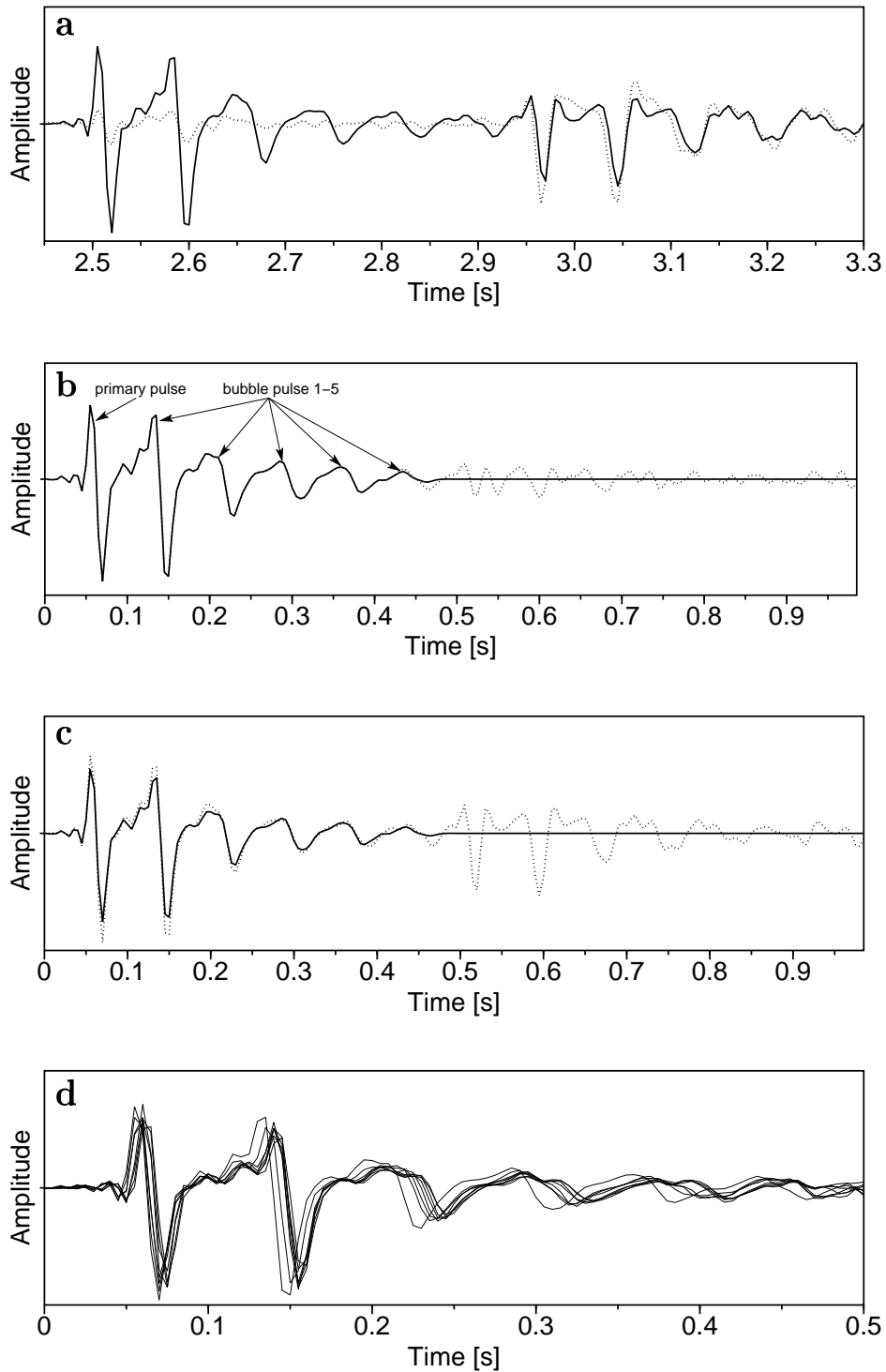
Figure 6.16: *Source wavelet for full waveform inversion extracted in t − x domain from primary and multiple seafloor reflection. Primary (solid) and multiple (dashed) reflection (a). Source wavelet is tapered at ∼0.5 s (solid) to include up to the fifth bubble pulse (b). Source wavelet (solid) and primary (dashed) reflection (c). Stability of source wavelet estimation illustrated on extracted wavelets from eight traces (d).*

Table 6.1: *Seafloor reflection coefficients extracted from OBH 04*

shot-receiver offset [m]	25	50	75	100	125	150
peak-to-peak	0.17	0.21	0.20	0.20	0.20	0.19
reflectivity	0.17	0.25	0.24	0.19	0.21	0.22

in delay time of the bubble pulse relative to the primary pulse. These small trace-to-trace variations in amplitude and phase of the source signature will have impact on the best possible waveform fit between synthetic and observed data because an average wavelet has to be designed for the inversion. This is particularly related to inversion of OBH data, considering the high-amplitude direct arrival. The average wavelet is calculated from the first eight traces.

In addition to the source wavelet, the seafloor reflection coefficient is required for the forward modeling algorithm. This parameter is extracted from (a) the peak-to-peak amplitude ratio of primary and multiple seafloor reflection (Warner, 1990), and (b) the reflectivity series of the seafloor obtained during extraction of the source wavelet. Table 6.1 shows results from six traces. Small, not systematic, variations of extracted reflection coefficients are assumed to be related to small inconsistencies in waveform shape affecting peak-to-peak amplitudes. An influence of AVO or 2-D effects at near-vertical incidence is not assumed. An average value of 0.20 for the seafloor reflection coefficient is implemented in the inversion.

6.4.3 Background velocity model

A viscoelastic starting model is required for the forward modeling algorithm. Only P-wave parameters such as the velocity gradient above the bright spot reflection and the seafloor reflection coefficient have been determined. Other parameters as V_s, ρ, and attenuation coefficients Q_p and Q_s have to be calculated from empirical relationships. S-wave velocities are calculated from Vp using the "mudrock line" introduced by Castagna et al. (1985), which is derived from in-situ and laboratory measurements on sediments and sedimentary rocks. Densities are calculated from Vp using Hamiltons (1978) relationship for soft, unlithified sediments at water depths of 4000 m. The seafloor reflection coefficient of 0.20 is only produced by an increase in density. The P-wave velocity at the seafloor is fixed at 1500 m/s.

Hamilton (1972) concluded approximate frequency independence of Q from rock through most natural, water-saturated sediments. Measurements of the in-situ attenuation Q_p in his report yielded a range from 100 to 450 for shallow clayey silt ($\sim 1000\,m$ water depth). Frequency independent quality factors of $Q_p = 200$ and $Q_s = 100$ are implemented here and kept constant in the sediments. For the water column, a constant Q_p of 10000 is assumed.

Based on the absence of reflections below the bright spot, the downward continuation of velocities remains undefined. Therefore, a constant velocity continuation below the bright spot is chosen. The models were then discretized at 5 m intervals (Fig. 6.17). Smoothing of the background model was applied to avoid large discontinuities at the reflectors.
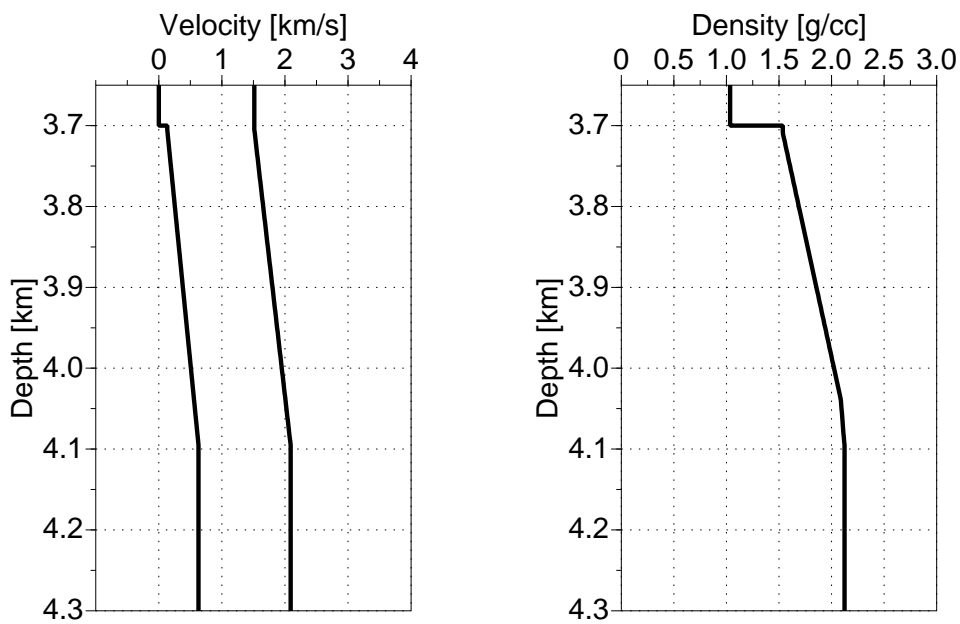
Figure 6.17: *Viscoelastic starting model for full waveform inversion. S-wave velocity and density are calculated from P-wave velocity. Attenuation values Q are constant with depth ($Q_p = 10000$ in water column, $Q_p = 200$ and $Q_s = 100$ in sediments).*

6.4.4 $\tau - p$ transformation and forward modeling

According to the frequency content of 8-50 Hz, data are transformed for slownesses up to 0.5, using the $\tau - p$ transformation implemented by Korenaga et al. (1997). Successful 'tuning' of frequency content and spatial sampling rate provide a clear image in $\tau - p$ domain. Prior to the inversion, a best fit forward modeling of the first arrival is performed including the extracted wavelet, the starting model and the seafloor reflection coefficient. Observed data are scaled to amplitudes of 1.2 ($1.0 + R_{sf}$) for the first arrival at vertical incidence, while the source wavelet is scaled to 1.0. This scaling accounts for correct amplitude ratios in OBH geometry. Fig. 6.18 (top) shows $\tau - p$ transformed observed data (bold line) plotted together with synthetic data (thin line), which are calculated from the background model. Amplitudes and waveform of the first arrival appear to be very well preserved. This has to be assured prior to the inversion, which is very sensitive to amplitude and phase informations. In Fig. 6.18 (bottom), the residual (observed data minus synthetic data) is plotted. In the first arrival, minor discrepancies are observed, which are mainly related to the first bubble pulse rather than to the primary pulse. This is assumed to be caused by the shot-to-shot variation of the source signature as discussed before. The bright spot reflection is well imaged in $\tau - p$ domain. A decrease in amplitudes around $p = 0.3$ and increased amplitudes at higher slownesses is observed. During inversion, the first 20 samples (100 m) below seafloor are kept constant to focus the inversion on the bright spot reflection. Data and wavelet are transformed to frequency domain before inversion.

6.4.5 Inversion

The full waveform inversion has been carried out in 11 runs, each consisting of five iterations. The final result of each run was smoothed and served as starting model for the next run. This approach retains the low-frequency character of the model and avoids a final model containing strong high-frequency components, which might produce perfect waveform fit, but hardly can be considered as a realistic model. The initial model does not contain any pre-information about a low-velocity layer (ref. Fig. 6.17). From the beginning, the full frequency and slowness range was inverted simultaneously, so that the inverted result contains a model, which is consistent with data from all slownesses and frequencies, and therefore is less likely to be influenced by incoherent noise due to two- and three-dimensional effects. These might produce solutions which fit at high or low slowness regions only. During the last runs, the misfit function changed only little ($\sim$1%), indicating convergence. At this point, the best waveform fit was achieved.

The best fit velocity model presented in Fig. 6.19 (thin line) shows a clear low-velocity zone (LVZ) overlain by a high-velocity zone (HVZ). The bold line shows the starting velocity model. The bright spot reflection is best reproduced by an increase in P-wave velocity up to $\sim$3000 m/s followed by a sharp drop down to $\sim$1000 m/s. The base of the low-velocity zone is developed as velocity gradient rather than a sharp bottom, as a consequence of the absence of a pronounced lower boundary reflection in the data. This model is in the following referred to as 'reservoir-model'. The evolution of the misfit function during the inversion is shown in Fig. 6.20. Smoothing of the model after every five iterations introduced an increase in the misfit, while the general
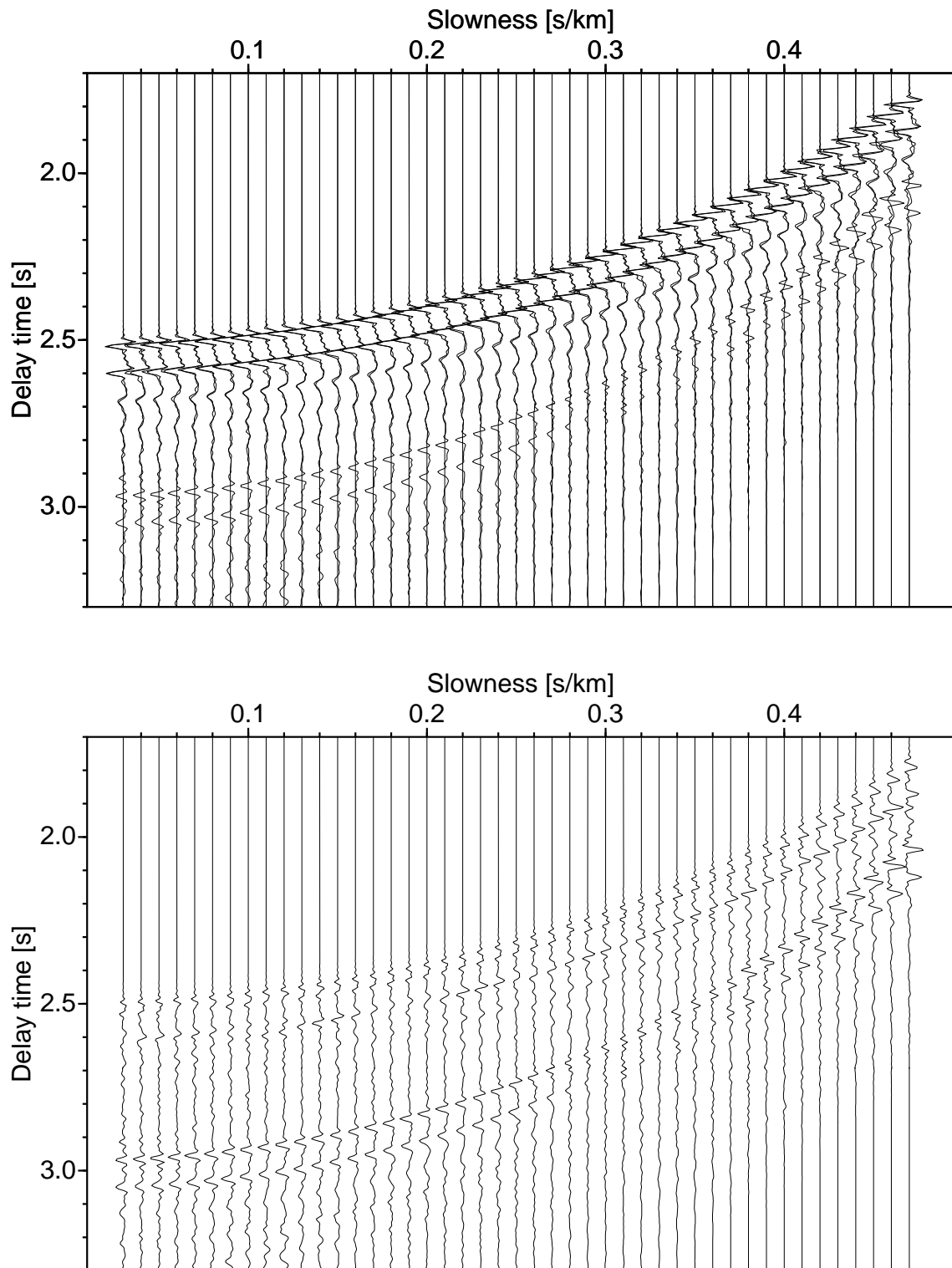
Figure 6.18: *Top: Observed data from OBH 04, line 14, in τ − p domain (bold line) plotted with synthetic seismogram (thin line) computed from background model (Fig. 6.17). Bottom: Residual data (real minus synthetic data). Figures are plotted using same amplitude gain.*
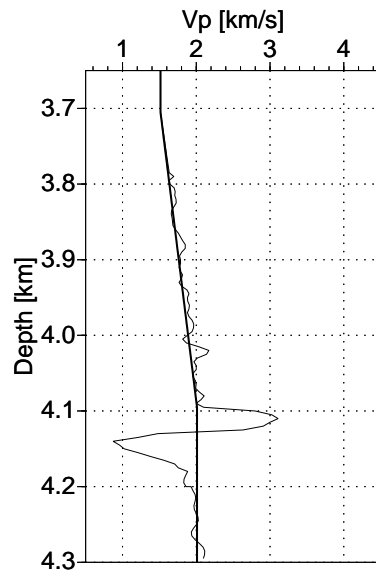
Figure 6.19: *Best fit P-wave velocity model after 55 iterations of the full slowness range (thin line), plotted together with the starting model (bold line). A clear low-velocity zone of ~50 m thickness overlain by a ~20 m high-velocity zone generate the best waveform fit to the observed data.*
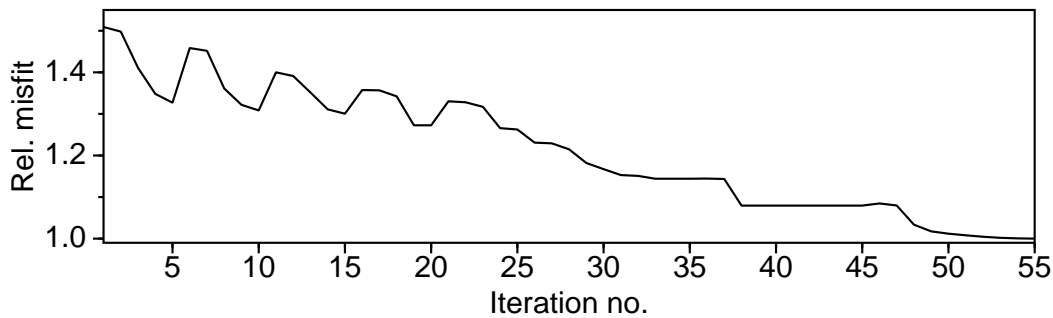
Figure 6.20: *Evolution of the misfit function during 55 iterations for the full slowness range. The final misfit is scaled to 1.0. The rise in misfit during the first iterations is caused by smoothing of the model after every five iterations.*

trend clearly develops towards a minimum. Additional iterations could not further reduce the misfit. The corresponding synthetic seismogram is plotted together with the observed data in Fig. 6.21 (top) showing a remarkable waveform fit throughout the full range of slownesses. The area around $p = 0.3$, showing reduced amplitudes, is very well fitted, as well as the high slowness range, where an increase in amplitudes is observed. Fig. 6.21 (bottom) shows the misfit between observed data and best fit synthetic data. Only minor coherent residuals in the intermediate slowness range are visible, which obviously are caused by small phase delay errors between observed and synthetic data, mainly linked to the bubble pulse sequence.
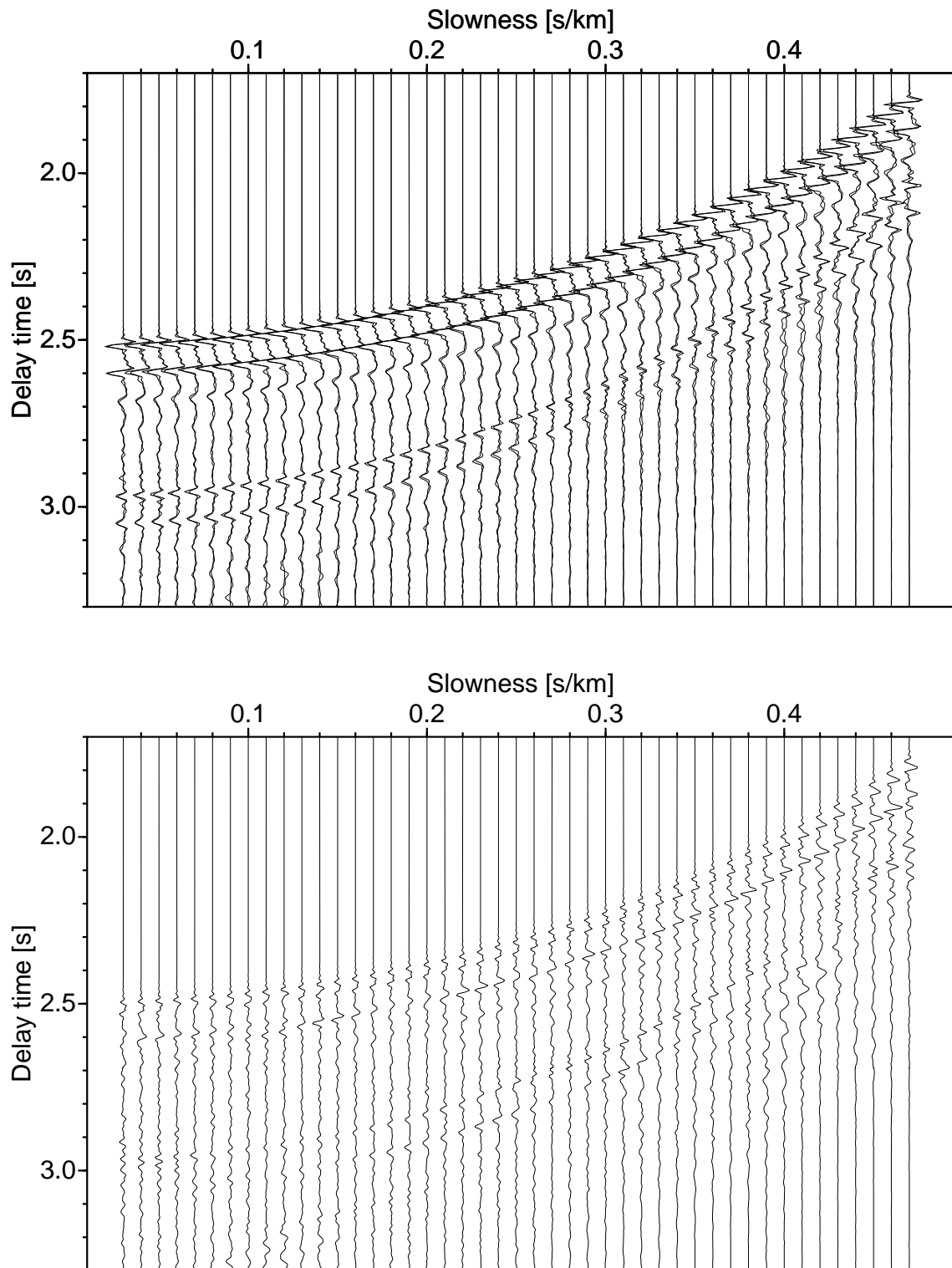
66

Figure 6.21: *Top: Observed data from OBH 04, line 14, in $\tau - p$ domain (bold line) plotted with best fit synthetic seismogram computed from final P-wave velocity model (Fig. 6.19) for full slowness range (thin line). Bottom: Residual data (real minus synthetic data). Figures are plotted using same amplitude gain.*

6.4.6 Perturbation of starting velocity model

In order to investigate the significance of the best fit model obtained, a number of 'basic' starting models, consisting of single high-velocity and single low-velocity zones, have been inverted. A faster convergence of the inversion is usually achieved when a smaller slowness range is implemented. Therefore, a slowness range from 0.03 to 0.25 ($x \leq 2000\ m$, $angles \leq 30°$, ref. Fig. 6.10) has been selected. This slowness range is equivalent to that used in other publications as e.g. Minshull *et al.* (1994) (p: $0.01 - 0.25$) and Pecher *et al.* (1998) (p: $0.06 - 0.20$), which were limited by the maximum source-receiver offsets in their data. Inversion results from three low-velocity zone (LVZ) models of 16 m, 20 m, and 24 m and four high-velocity zone (HVZ) starting models of 24 m, 28 m, 32 m, and 36 m are shown in Fig. 6.22. Further thicknesses of the LVZ and HVZ show worse misfit. The waveform fit achieved after 5 iterations is generally about 90% ± 3% (crosscorrelation) for individual traces and the misfit function changed less than 1 %, indicating convergence. The misfit at the bright spot S_{BS} is measured in a 200 ms window around the bright spot reflection in terms of total residual energy divided by total energy of the observed data; calculated from the following equation:

$$S_{BS} = \frac{\sum_{p,\omega}(d_{cal}(p,\omega) - d_{obs}(p,\omega))^2}{\sum_{p,\omega}(d_{obs}(p,\omega))^2} \tag{6.1}$$

Results clearly show, that the final waveform fits obtained from all starting models are similar. The 28 m high-velocity zone (Fig. 6.22e) shows almost the same waveform fit as the result from the 'reservoir-model' (Fig. 6.22h). The best fit inversion result from a low-velocity zone model shows similar misfit in this particular slowness range (Fig. 6.22b). From these inversion results it is concluded, that inverting for only the lower slowness region does not provide any unique results. A 'sill-model' provides almost identical waveform fit as a 'reservoir-model' and a pure low-velocity zone model.

The 'basic' starting models, which produced the best waveform fit during inversion of the lower slowness range (20 m LVZ and 28 m HVZ) are chosen as starting models for inversion of the full slowness range in order to analyze uniqueness of the best-fit model. Due to the slower convergence of the misfit function, one single run of 20 iterations was carried out. Results are again considered calculating the misfit S_{BS} for the bright spot reflection. Fig. 6.23 shows the best fit velocity models after 20 iterations (thin line) derived from 'basic' starting models (bold line), plotted together with best fit synthetic seismograms and observed data. The final model derived from the LVZ starting model (Fig. 6.23a) changed significantly during inversion. The initial low-velocity zone has been reduced and a HVZ peak above 4.1 s followed by a slight decrease in velocity evolved. This model tends to develop against a solution similar to the 'reservoir-model' (Fig. 6.23c), whereas the HVZ model converges against a local solution retaining the HVZ structure. The 'reservoir-model' shows the best misfit after 20 iterations. The major feature differentiating the HVZ and the 'reservoir-model' is the waveform fit around $p = 0.3$, indicated by arrows in the seismic sections. The high-velocity model does not reproduce the amplitude decrease observed. The evolution of the misfit functions during inversion is shown in Fig. 6.24.
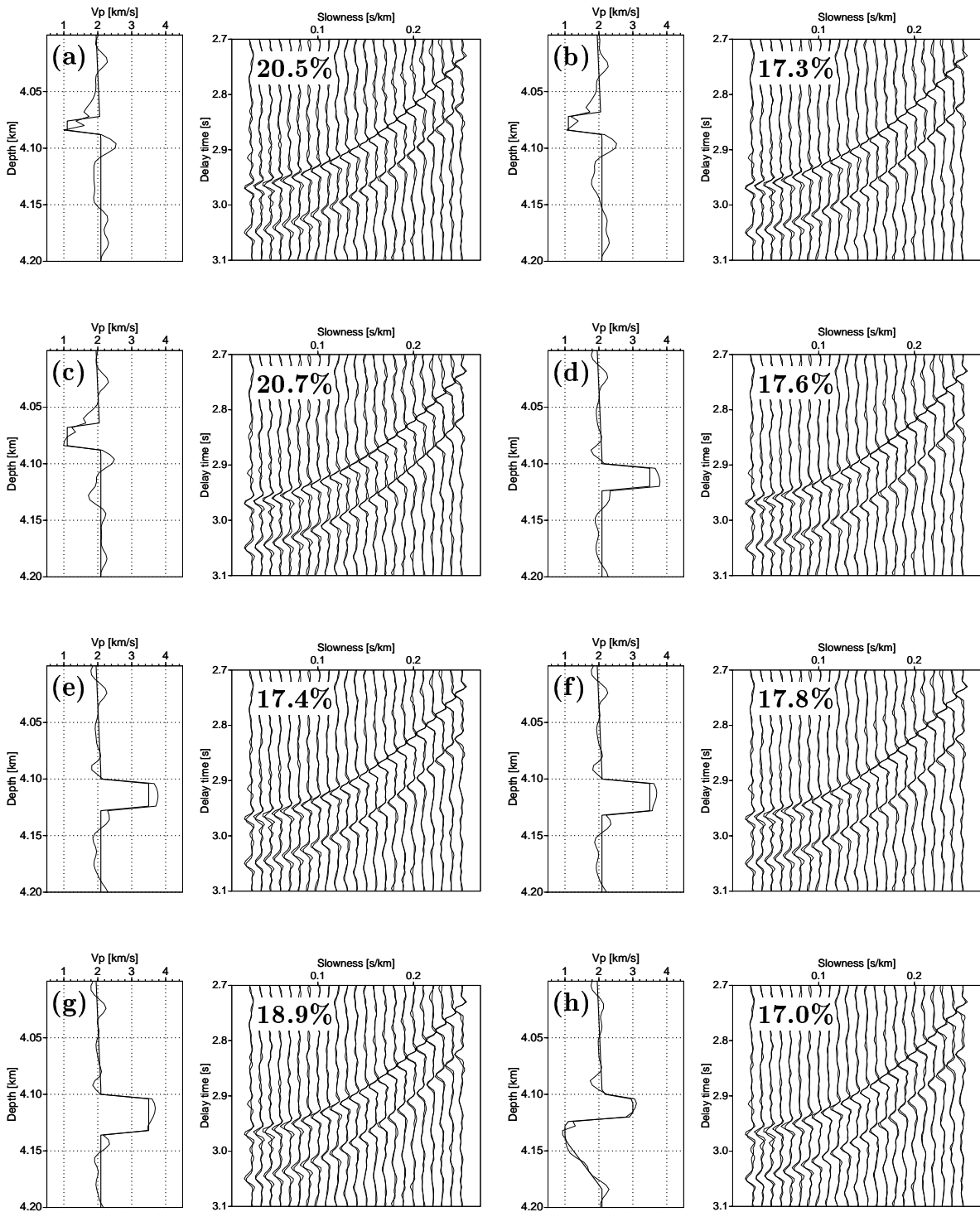
68

Figure 6.22: *Inversion results (thin line) for various starting models (bold line) plotted with observed data (bold line) and best fit seismogram (thin line). Inversion is performed only for the lower slowness range (0.03 − 0.25). The misfit S_{BS} after 5 iterations is indicated in the seismograms. (a) 16 m LVZ. (b) 20 m LVZ. (c) 24 m LVZ. (d) 24 m HVZ. (e) 28 m HVZ. (f) 32 m HVZ. (g) 36 m HVZ. (h) 'reservoir-model' from previous section.*
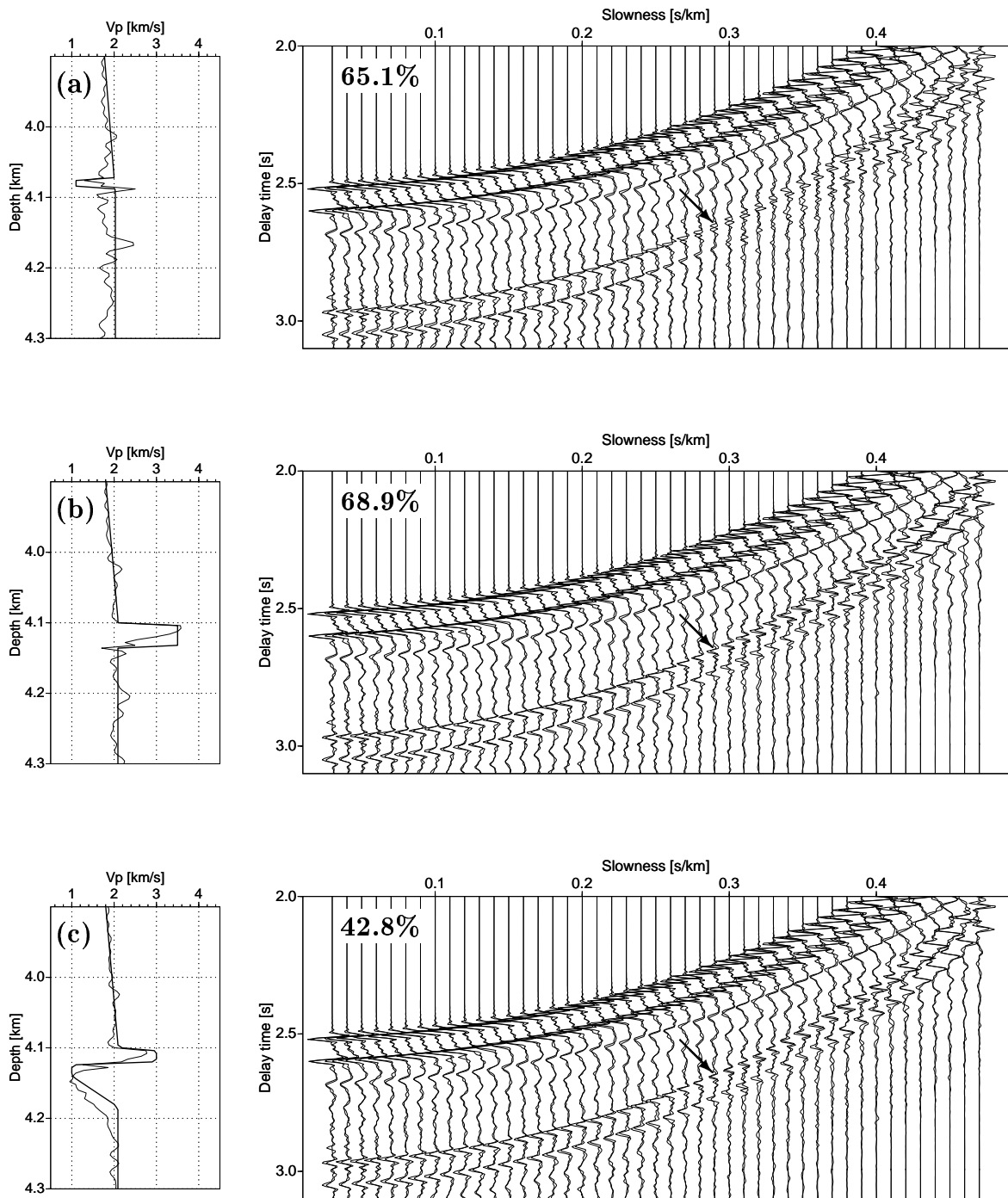
Figure 6.23: *Best fit P-wave velocity models (thin line) derived from inversion of three 'basic' starting models (bold line) for the full slowness range. (a) 20 m LVZ. (b) 28 m HVZ. (c) 'reservoir-model'. The misfit S_{BS} after 20 iterations is indicated in the seismograms. Arrows mark the region around $p = 0.3$, where the 'reservoir-model' produces a significantly better waveform fit.*
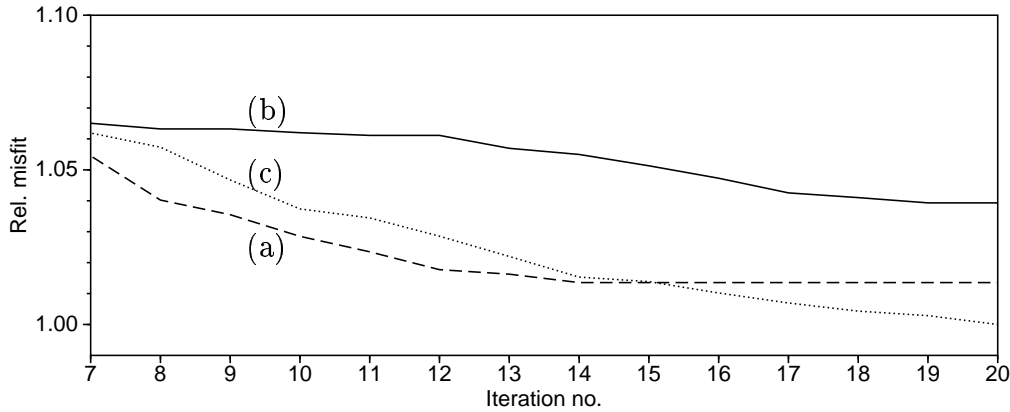
Figure 6.24: *Evolution of the misfit function from inversion of three different starting models (Fig. 6.23) for the full slowness range. (a) 20 m LVZ. (b) 28 m HVZ. (c) 'reservoir-model'. The overall best misfit after 20 iterations (c) is scaled to 1.0.*

6.4.7 Discussion and interpretation of inversion results

The OBH data and the bright spot reflection emerge to be very well suited for 1-D waveform inversion. A very good waveform fit in the entire slowness range was attained. Results provide a number of new constraints concerning the seismic origin of the bright spots and the uniqueness of the interpretation. The following conclusions are drawn from this analysis:

- The best waveform fit is obtained from a 'reservoir-model', which consists of a ~20 m high-velocity zone underlain by a ~50 m low-velocity gradient zone.

- 'Sill-model', 'reservoir-model' and LVZ model produce similar waveform fit in the restricted lower slowness range (p: $0.03 - 0.25$). Thus it is not possible to draw any conclusions about the seismic origin of the bright spots from inversion results in this slowness (≤ 0.25), offset ($\leq 2000\ m$), and angle of incidence ($\leq 30°$) range.

- The main distinctive feature between the 'sill-model' and the 'reservoir-model' is the waveform fit in the slowness range about $p = 0.3$, where the 'sill-model' does not reproduce the observed amplitude decrease

Since the obtained results are based on inverting for P-wave velocity only, the influence of S-wave velocity and density has to be discussed. Presumably, the high-velocity zones in the 'reservoir-model' and the 'sill-model' will additionally show variations in S-wave velocity and density. Variations in density primarily affect the amplitudes in the lower slowness range and might even produce an overall better waveform fit due to an increased vertical-incidence acoustic impedance contrast. The S-wave velocity will mainly affect the intermediate slowness range, due to the change in amplitude-versus-offset behavior caused by an increased S-wave velocity contrast (e.g., Castagna et al., 1993). The contribution of these parameters might reduce the maximum P-wave velocities in the final model slightly. A significant increase of shear-wave velocity in the 'sill-model' would produce a noticeable converted S-wave emerging in the data, as
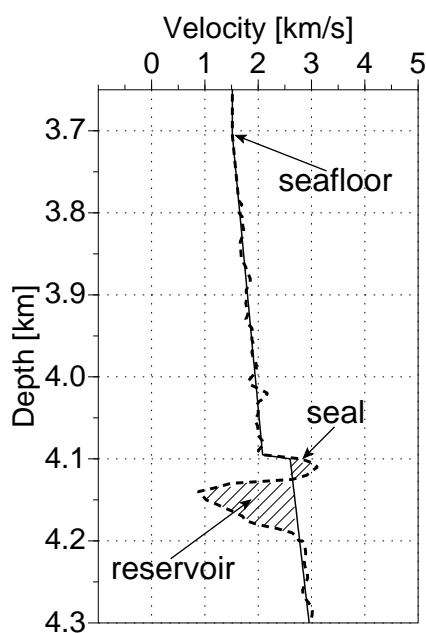
71

Figure 6.25: *Interpreted, best fit P-wave velocity model for the full slowness range (dashed line) showing a reservoir of about 50 m thickness. Modified background velocity model (solid line) represents estimated velocity trend without reservoir.*

observed by Singh et al. (1998) from inversion of reflection data from a crustal magma chamber at the southern East Pacific Rise. This converted mode is not observed in these OBH data, which additionally privilege the 'reservoir-model'.

The best fit inversion result is interpreted as a typical reservoir model (Fig. 6.25), where free or dissolved gas is trapped beneath a stratigraphic discontinuity causing a pronounced decrease in bulk P-wave velocity. The reservoir has an approximate thickness of 50 m. The high-velocity zone above is interpreted as reservoir seal, which basically might be composed of a natural increase in velocity as indicated by the background velocity structure (Fig. 6.25, solid line) and additionally be amplified by in situ consolidation processes (e.g., cementation, hydrated sediments), which reduce porosity and permeability (Schön, 1996).

Chapter 7

Discussion and Conclusions

This study provides substantial evidence for the existence of large fluid reservoirs in the deep-water sedimentary basin adjacent to the Canary Islands. Interpretation of wide-angle and normal-incidence seismic data is based on analysis of a number of pronounced seismic bright spots on a dense grid of reflection seismic lines. However, lack of near well logs, equivocal age-dating of the sedimentary sequence, and lack of geochemical information advises cautiousness. Several examples for seismic bright spots associated with igneous intrusions and volcanic ash deposits have been reported (e.g., Pironon & Champanhet, 1992), although most of these studies lack supplemental wide-angle information. Present analyses of comprehensive seismic data provide a number of characteristics associated with the Canary Island bright spots, where several are related to the presence of gas (direct hydrocarbon indicators), and thus significantly reduce the possibility of misinterpretation:

- Strong reflection amplitudes of bright spots exceed those from the seafloor, volcanic deposits, and lithologic boundaries such as the basement. Calibration of amplitudes at the seafloor reflection yields absolute reflection coefficient of up to 0.4.

- Clear phase reversal of the bright spot reflection indicates a decrease in acoustic impedance.

- Distinct limited areal extent of bright spots on 25-100 km^2.

- Occurrence at 60-80 km from the shoreline of the islands.

- Embedded in subparallel weak-reflective to transparent sedimentary sequences, following the sedimentary bedding.

- Occurence in immediate vicinity of mud diapirs related to the presence of over-pressured muds and vertical fluid migration.

- Absence of a resolvable time-sag or pull-up anomaly associated with reflectors beneath the bright spots points towards a "thin" layer.

- Absence of a lower boundary reflection indicates an event at or below tuning thickness or a velocity gradient at the bottom of the reservoir.

- An amplitude-versus-offset response characteristic for a negative impedance contrast, i.e., absence of refraction event, critical angle and associated phase reversal.

- Emergence of a thin high-velocity layer (seal) above an $\sim$50 m low-velocity gradient zone (gas) as best-fit model from full waveform inversion.

In the sedimentary basin adjacent to the volcanic islands, two sources of fluids are proposed. Firstly, CO_2-rich fluids of magmatic origin, transported from deep crustal and mantle reservoirs to shallow magma chambers, migrating along faults and trapped in the sedimentary sequence. In this case the bright spots demonstrate the first direct observation of large magmatic gas reservoirs. Secondly, microbially generated or thermogenic methane is considered. Large amounts of methane-rich fluids have been drilled at ODP site 955 (southeast of Gran Canaria) and ODP site 952 (Madeira Abyssal Plain), generated from organic-rich sediment deposits originating at the African continental margin (Schmincke et al., 1995).

The temperature and pressure conditions at the potential reservoirs are estimated assuming that the pore pressure can be approximated by the hydrostatic pressure. A mud line temperature of about 3°C and geothermal gradients between 10°C/km and 50°C/km, determined at the ODP sites (Schmincke et al., 1995), yield 8-28°C at about 450 atm at reservoir depths. Although these values might vary significantly in areas of increased heat flow and overpressured sequences, the classification of pore fluid properties in phase diagrams is possible. In the carbon dioxide-water phase diagram (Fig. 7.1), the bright spots are located at the transition between (i) coexistence of carbon dioxide clathrates and liquids, and (ii) coexistence of water and carbon dioxide gas. In-situ formation of carbon dioxide clathrates in the sedimentary column could form an impermeable seal, where upward migrating fluids are trapped. The presence of carbon dioxide dissolved in liquids agree well with the estimated AVO response for almost constant Poisson's ratio (minor amounts of free gas). In the methane-water phase diagram (Fig. 7.2), bright spots are located predominantly within the stability field of methane clathrates (gas hydrate) and free gas. Depending on the amount of available methane, large deep-water hydrocarbon reservoirs are conceivable.

However, the bright spots imaged in the Southern Canary Basin are clearly distinguishable against the occurrence of bottom simulating reflectors, observed in polar regions and outer continental margins. In contrast to the BSRs, the bright spots follow the sedimentary bedding. The reflectivity above BSRs is usually characterized as weak reflective due to hydrate formation and a distinct increase of reflectivity beneath, wheras the bright spots are embedded in weak reflective sequences and occur at various depths below the seafloor.

Based on obtained velocity-depth profiles, the bright spots are located in depths of 300-800 m below seafloor. The overall thickness of the sedimentary sequence down to the basement (Layer 2A) is roughly estimated to be about 1200 m in the western part of the Southern Canary Basin and agree well with published results (e.g., Ranero et al., 1995). Magnetic anomalies in this region propose a Jurassic age of about 156 Ma (M25) for the igneous oceanic crust, while age-dating on oldest sedimentary rocks at ODP site 956 has determined ages of about Early Miocene ($\sim$20 Ma) at 700 m below seafloor. Although the sediment influx at the island flanks might be considered as significantly larger than at the bright spot locations, a striking discrepancy with
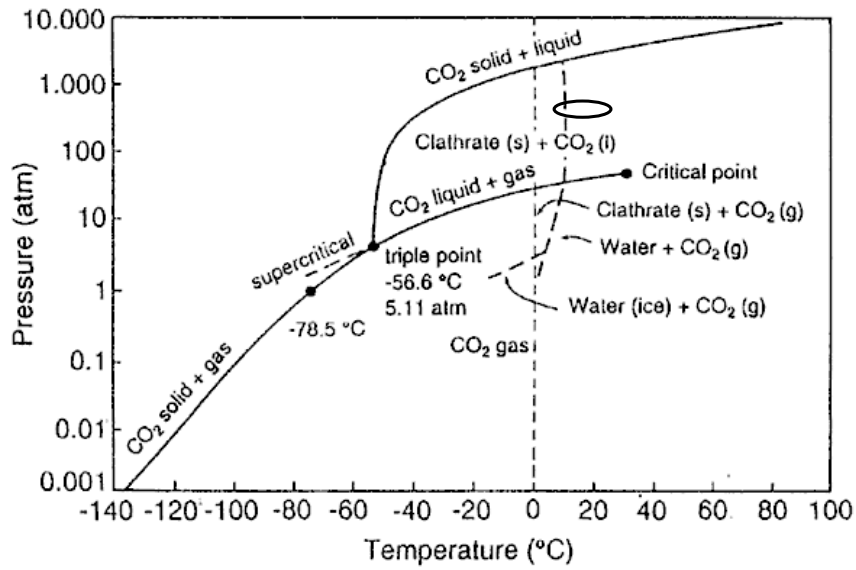
Figure 7.1: Pressure-temperature phase diagram for carbon dioxide (Murray et al., 1996). Circle indicates approximate location of bright spots.
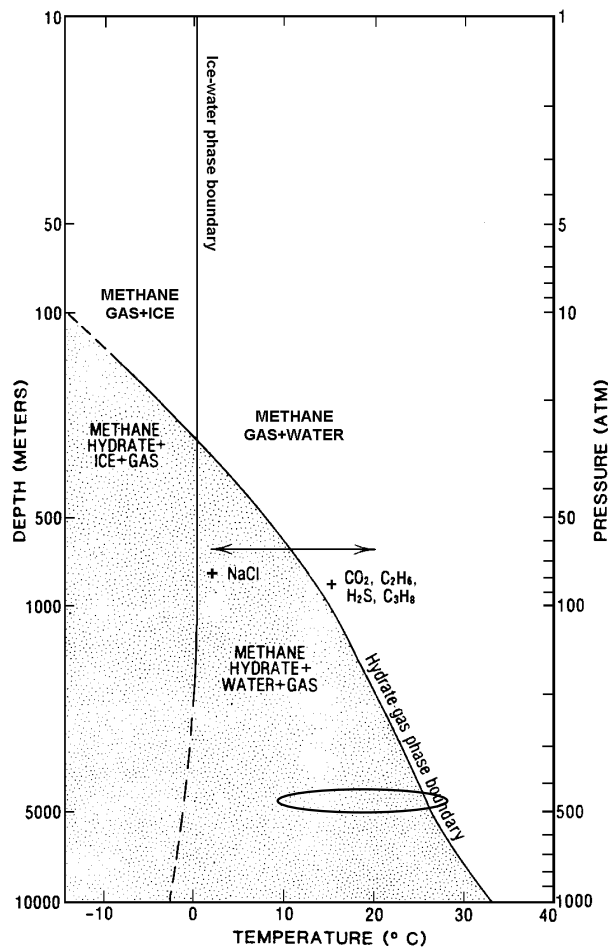

Figure 7.2: Pressure-temperature phase diagram for methane (Kvenvolden & Barnard, 1983). Circle indicates approximate location of bright spots.

respect to the age of the lower sedimentary sequence occurs. This ambiguity must be discussed in the context of the evolution of the sedimentary basins adjacent to the Canary Islands. The current topic of discussion is whether the basins have developed at noticeable shallower water depths and subsided due to the load of the volcanic islands as proposed for Tenerife (Watts & Masson, 1995), or subsidence is much less distinctive (Funk & Schmincke, 1998).

Obtained results associated with high signal-to-noise ratios from AVO, waveform inversion, and semblance based velocity analysis point out that OBH data are very well-suited for providing valuable petrophysical constraints in deep-water environments. The waveform inversion additionally pointed out that considering small offsets and hence the lower slowness range only, provide ambiguous results, whereas inversion of the entire slownesses range lead to significant reduction of ambiguity. Although tuning effects have been neglected during AVO analysis, the observed amplitude minimum in the AVO response and the $\tau - p$ domain is certainly related to interface properties, since this observation is made on AVO responses from two independent reflection segments at the bright spot.

The preferred model from these investigations is the reservoir model, where fluids are trapped beneath an impermeable layer (seal). To conclusively determine the origin of bright spots and nature of fluids, geophysical technology application must be combined with regional and local geology studies on specialized follow-up experiments. Geochemical analysis on sediment samples from the seafloor above bright spots and mud diapirs might be considered to determine the source and origin of the fluids. Seismic profiles at ODP site 955 could provide seismic responses associated with confirmed gas accumulations in the subsurface, and an AVO study at ODP site 956 allow to investigate the wide-angle seismic response from the regional marker horizon (high-impedance thin-bed). In this context, a broadband data acquisition using a number of smaller airguns and subsequently denser spatial sampling has to be considered. Investigation of southward distribution of bright spots in the Southern Canary Basin, away from the immediate influence of active volcanism, should provide additional insight.

References

Aki, K., & Richards, P.G. 1980. *Quantitative seismology: Theory and methods*. W.H. Freeman and Co.

Andreassen, K., Hogstad, K., & Berteussen, K.A. 1990. Gas hydrate in the southern Barents Sea, indicated by shallow seismic anomaly. *First Break*, **8**, 235–245.

Andreassen, K., Hart, P.E., & MacKay, M. 1997. Amplitude versus offset modeling of the bottom simulationg reflection associated with submarine gas hydrates. *Marine Geology*, **137**, 25–40.

Barnes, A.E. 1998. The complex seismic trace made simple. *The Leading Edge*, **17(4)**, 473–476.

Biot, M.A. 1956. Theory of propagation of elastic waves in a fluid-saturated porous solid, I. low-frequency range. *J. Acoust. Soc. Am.*, **28**, 168–191.

Canales, J.P., & Danobeitia, J.J. 1998. The Canary Island swell: a coherence analysis of bathmetry and gravity. *Geophys. J. Int.*, **132**, 479–488.

Carracedo, J.C. 1994. The Canary Islands: an example of structural control on the growth of large oceanic-island volcanoes. *J. Volcanol. Geotherm. Res.*, **60**, 225–341.

Castagna, J.P. 1993. AVO analysis - Tutorial and Review. *Pages 3–36 of:* Castagna, J.P, & Backus, M.M. (eds), *Offset-Dependent Reflectivity - Theory and Practice of AVO Analysis*.

Castagna, J.P., Batzle, M.L., & Eastwood, R.L. 1985. Relationship between compressional-wave and shear-wave velocities in clastic silicate rocks. *Geophysics*, **50**, 571–581.

Charvis, P., & Danobeitia, J.J. 1999. Hotspot and Oceanic Crust Interaction. *Journal of Geodynamics*, **28**.

Červeny, V., Molotkov, I.A., & Pšenčik. 1977. *Ray method in seismology*. Univerzita Karlova, Praha.

Collier, J.S., & Singh, S.C. 1997. Detailed structure of the top of the melt body beneath the East Pacific Rise at $9°40'N$ from waveform inversion of seismic reflection data. *J. Geophys. Res.*, **102**, 20287–20304.

Dickens, G.R., Paull, C.K., Wallace, P., & the ODP Leg 164 Scientific Party. 1997. Direct measurements of in situ methane quantities in a large gas-hydrate reservoir. *Nature*, **385**, 426–428.

Dragoset, B. 2000. Introduction to air guns and air-gun arrays. *The Leading Edge*, **19(8)**, 892–897.

Ecker, C., Dvorkin, J., & Nur, A. 1998. Sediments with gas hydrates: Internal structure from seismic AVO. *Geophysics*, **63(5)**, 1659–1669.

Estill, R., & Wrolstad, K. 1993. Interpretive Aspects of AVO - Application to Offshore Gulf Coast Bright-Spot Analysis. *Pages 267–284 of:* Castagna, J.P, & Backus, M.M. (eds), *Offset-Dependent Reflectivity - Theory and Practice of AVO Analysis*.

Flueh, E.R., & Bialas, J. 1996. A digital, high data capacity ocean bottom recorder for seismic investigations. *Int. Underwater Systems Design*, **18(3)**, 18–20.

Funk, T., & Schmincke, H.-U. 1998. Growth and destruction of Gran Canaria deduced from seismic reflection and bathymetry data. *J. Geophys. Res.*, **103**, 15393–15407.

Gajewski, D, & Pšenčik, I. 1990. Vertical Seismic Profile Synthetics by Dynamic Ray Tracing in Laterally Varying Anisotropic Structure. *J. Geophys. Res.*, **95**, 11301–11315.

Gerlach, T.M., & Graeber, E.J. 1985. Volatile budget of Kilauea volcano. *Nature*, **313**, 273–277.

Gold, T. 1999. *The Deep Hot Biosphere*. Copernicus/Springer-Verlag, 175 Fifth Avenue, New York.

Hagen, R. 1991. Underway geophysics. *Pages 77–97 of:* Kroenke, L.w., Berger, W.H., & Janecek, T.R. et al. (eds), *Proceedings of the Ocean Drilling Program, Initial Reports*, vol. 130.

Hales, A.L., & Roberts, J.L. 1974. The Zoeppritz amplitude equations: more errors. *Bull. Seis. Soc. Am.*, **64**, 285.

Hamilton, E.L. 1972. Compressional-wave attenuation in marine sediments. *Geophysics*, **37**, 620–646.

Hamilton, E.L. 1978. Sound velocity-density relations in sea-floor sediments and rocks. *J. Acoust. Soc. Am.*, **63(2)**, 366–377.

Hardage, B.A. 1983. *Vertical Seismic Profiling, Part A: Principles*. Geophysical Press, London.

Heggland, R. 1997. Detection of gas migration from a deep source by the use of exploration 3D seismic data. *Marine Geology*, **137**, 41–47.

Hilterman, F., van Schuyver, C., & Sbar, M. 2000. AVO examples of long-offset data in the Gulf of Mexico. *The Leading Edge*, **19(11)**, 1200–1213.

Hinz, K., Dostmann, H., & Fritsch, F. 1982. The continental margin off Morocco: seismic sequences, structural elements and geological development. *Pages 34–60 of:* von Rad, U., Hinz, K., Sarnthein, M., & Seibold, E. (eds), *Geology of the Northwest African continental margin.* Springer Verlag, Berlin, Heidelberg, New York.

Hoernle, K.A., & Schmincke, H.-U. 1993. The role of partial melting in the 15-Ma geochemical evolution of Gran Canaria: A blob model for the Canary Hotspot. *J. Petrol.*, **34**, 599–626.

Hyndman, R.D., & Davis, E.E. 1992. A mechanism for the formation of methane hydrate and seafloor bottom-simulating reflectors by vertical fluid expulsion. *J. Geophys. Res.*, **97(B5)**, 7025–7041.

Juhlin, C. 1990. Interpretation of the reflections in the Siljan Ring area based on results from the Gravberg-1 borehole. *Tectonophysics*, **173**, 345–360.

Katzman, R., Holbrook, W.S., & Paull, C.K. 1994. Combined vertical-incidence and wide-angle seismic study of a gas hydrate zone, Blake Ridge. *J. Geophys. Res.*, **99**, 17975–17995.

Keary, P., & Brooks, M. 1991. *Geophysical Exploration, 2nd Edition.* Blackwell Science.

Kennett, B.L.N., & Kerry, N.J. 1979. Seismic waves in a stratified half space. *Geophys. J. R. Astron. Soc.*, **57**, 557–583.

Khattri, K., Mithal, R., & Gaur, V. 1979. Pattern space of seismic anomalies associated with hydrocarbon deposits. *Geophysical Prospecting*, **27**, 339–359.

Klitgord, K.D., & Schouten, H. 1986. Plate kinematics of the Central Atlantic. *Pages 351–378 of:* Vogt, P.R., & Tucholke, B.E. (eds), *The Geology of North America, Volume M, The Western North Atlantic region.* Geological Society of America.

Knott, C.G. 1899. Reflexion and refraction of elastic waves with seismological applications. *Phil. Mag.*, **48**, 64–97.

Korenaga, J., Holbrook, W.S., Singh, S.C., & Minshull, T.A. 1997. Natural gas hydrates on the southeast U.S. margin: Constraints from full waveform inversion and travel time inversion of wide-angle seismic data. *J. Geophys. Res.*, **102(NO. B7)**, 15345–15365.

Kormendi, F., & Dietrich, M. 1991. Nonlinear waveform inversion of plane-wave seismograms in stratified elastic media. *Geophysics*, **56**, 664–674.

Krastel, S. 1999. *Growth processes and destructive events during the evolution of volcanic islands: a case study from Gran Canaria.* Ph.D. thesis, University of Kiel, Germany.

Kvenvolden, K. 1993. Gas Hydrates - Geological perspective and global change. *Reviews of Geophysics*, **31(2)**, 173–187.

Kvenvolden, K.A., & Barnard, L.A. 1983. Hydrates of natural gas in continental margins. *Am. Assoc. Pet. Geol., Mem. 34*, 631–641.

Mackay, M.E., Jarrad, R.D., Westbrook, G.K., Hyndman, R.D., & Shipboard Scientific Party of Ocean Drilling Program Leg 146. 1994. Origin of bottom-simulating reflectors: geophysical evidence from the cascadia accretionary prism. *Geology*, **22**, 459–462.

Minshull, T.A., & Singh, S.C. 1993. Shallow Structure of Oceanic Crust in the Western North Atlantic From Seismic Waveform Inversion and Modeling. *J. Geophys. Res.*, **98(B2)**, 1777–1792.

Minshull, T.A., Singh, S.C., & Westbrook, G.K. 1994. Seismic velocity structure at a gas hydrate reflector, offshore western Colombia, from full waveform inversion. *J. Geophys. Res.*, **99(B3)**, 4715–4734.

Minster, J.B., & Jordan, T.H. 1978. Present-day plate motions. *J. Geophys. Res.*, **83(B11)**, 5331–5354.

Murray, C.N., Visintini, L., Bidoglio, G., & Henry, B. 1996. Permanent storage of carbon dioxide in the marine environment: The solid CO_2-penetrator. *Energy Convers. Mgmt.*, **137**, 1067–1072.

Nsoga Mahob, P., Castagna, J.P., & Young, R.A. 1999. Case History: AVO inversion of a Gulf of Mexico bright spot - A case study. *Geophysics*, **64**, 1480–1491.

Oliver, J.E. 1990. COCORP and Fluids in the crust. *Pages 128–139 of: The Role of Fluids in Crustal Processes*. National Academy Press, Washington, D.C.

Ostrander, W.J. 1984. Plane-wave reflection coefficients for gas sands at nonnormal angles of incidence. *Geophysics*, **49(10)**, 1637–1648.

Papenberg, C. 2000. *OBH-Weitwinkelmessungen zur Untersuchung eines Bright Spots im südlichen Kanarischen Becken*. Diplomarbeit, University of Kiel, Germany.

Pecher, I.A., Ranero, C.R., von Huene, R., Minshull, T.A., & Singh, S.C. 1998. The nature and distribution of bottom simulating reflectors at the Costa Rica convergent margin. *Geophys. J. Int.*, **133**, 219–229.

Pecher, Ingo A. 1995. *Seismic studies of bottom simulating reflectors at the convergent margins offshore Peru and Costa Rica*. Ph.D. thesis, University of Kiel, Germany.

Pironon, B., & Champanhet, J.M. 1992. Evaluation of Pliocene bright spots in the Adriatic Sea, Italy - volcanic ash or gas. *First Break*, **10(7)**, 259–273.

Rabbel, W. 1987. *Seismische Erkundung oberflächennaher Störzonen: Strahlenseismische Grundlagen und Feldbeispiele*. Ph.D. thesis, University of Kiel, Germany.

Ranero, C.R., Torne, M., & Banda, E. 1995. Gravity and multichannel seismic reflection constraints on the lithospheric structure of the Canary Swell. *Mar. Geophys. Res.*, **17**, 519–534.

Roden, R., & Sepúlveda, H. 1999. The significance of phase to the interpreter: Practical guidlines for phase interpretation. *The Leading Edge*, **18(9)**, 774–777.

Roeser, H.A. 1982. Magnetic anomalies in the magnetic quiet zone off Morocco. *Pages 351–378 of:* von Rad, U., Hinz, K., Sarnthein, M., & Seibold, E. (eds), *Geology of the Northwest African continental margin*. Springer Verlag, Berlin.

Roest, W.R., Danobeitia, J.J., Verhoef, J., & Collette, B.J. 1992. Magnetic anomalies in the Canary Basin and the Mesozoic evolution of the Central North Atlantic. *Mar. Geophys. Res.*, **14**, 1–24.

Rutherford, S.R., & Williams, R.H. 1989. Amplitude-versus-offset variations in gas sands. *Geophysics*, **54**, 680–688.

Schmincke, H.-U. 1986. *Vulkanismus*. Wissenschaftliche Buchgesellschaft, Darmstadt.

Schmincke, H.-U. 1998. Zeitliche, strukturelle und vulkanische Entwicklung der Kanarischen Inseln, der Selvagens Inseln und des Madeira-Archipels. *Pages 27–69 of:* Bischoff, W. (ed), *Handbuch der Reptilien und Amphibien Europas*. AULA-Verlag, Wiesbaden.

Schmincke, H.-U., & Rihm, R. 1994. *Ozeanvulkan 1993, Cruise No. 24, 15 April - 9 Mai 1993*. Meteor Berichte. Universität Hamburg.

Schmincke, H.-U., & Sumita, M. 1998. Volcanic evolution of Gran Canaria reconstructed from apron sediments: Synthesis of VICAP project drilling. *Pages 443–469 of:* Weaver, P.P.E., Schmincke, H.-U., Firth, J.V., & Duffield, W. (eds), *Proc. ODP Sci. Results*. College Station, TX.

Schmincke, H.-U., Weaver, P.P.E., Firth, J., & Shipboard Scientific Party. 1995. *Proceedings of the Ocean Drilling Program, Initial Reports*. Vol. 157. College Station, TX.

Schmincke, H.U., Klügel, A., Hansteen, T.H., Hoernle, K., & van den Bogaard, P. 1998. Samples from the Jurassic ocean crust beneath Gran Canaria, La Palma and Lanzarote (Canary Islands). *Earth and Planetary Science Letters*, **163**, 343–360.

Schön, J.H. 1996. *Physical properties of rocks. Fundamentals and principles of petrophysics*. Pergamon press, Oxford.

Sengbush, R.L. 1983. *Seismic Exploration Methods*. IHRDC, Publishers, Boston.

Sheriff, R.E. 1974. *Seismic detection of hydrocarbons - the underlying physical principles*. preprint.

Sheriff, R.E. 1991. *Encyclopedic dictionary of exploration geophysics, 3rd Ed.* Soc. Expl. Geophys.

Sheriff, R.E., & Geldart, L.P. 1982. *Exploration Seismology*. Cambridge University Press.

Shipley, T.H., Houston, M.H., Buffler, R.T., Shaub, F.J., McMillen, K.J., Ladd, J.W., & Worzel, J.L. 1979. Seismic reflection evidence for the widespread occurence of possible gas-hydrate horizons on continental slopes and rises. *AAPG Bull.*, **63**, 2204–2213.

Shuey, R.T. 1985. A simplification of the Zoeppritz equations. *Geophysics*, **50**, 609–614.

Silver, E., Kastner, M., Fisher, A., Morris, J., McIntosh, K., & Saffer, D. 2000. Fluid flow paths in the Middle American Trench and Costa Rica margin. *Geology*, **28(8)**, 679–682.

Singh, S.C., Minshull T.A. Spence G.D. 1993. Velocity Structure of a Gas Hydrate Reflector. *Science*, **260**, 204–210.

Singh, S.C., & Minshull, T.A. 1994. Velocity structure of a gas hydrate reflector at Ocean Drilling Program site 889 from a global seismic waveform inversion. *J. Geophys. Res.*, **99**, 24221–24233.

Singh, S.C., West, G.F., & Chapman, C.H. 1989. On plane-wave decomposition: Alias removal. *Geophysics*, **54(10)**, 1339–1343.

Singh, S.C., Kent, G.M., Collier, J.S., Harding, A.J., & Orcutt, J.A. 1998. Melt to mush variations in crustal magma properties along the ridge crest at the southern East Pacific Rise. *Nature*, **394**, 874–878.

Taner, M.T., & Sheriff, R.E. 1977. Application of amplitude, frequency, and other attributes to stratigraphic and hydrocarbon determination. *Pages 301–327 of:* Payton, C.E. (ed), *Applications to hydrocarbon exploration.* AAPG Memoir 26: Tulsa, Am. Assn. Petroleum Geologists.

Tarantola, A, & Valette, B. 1982. Generalized nonlinear inverse problems solved using the least-squares criterion. *Rev. Geophys. Space Phys.*, **20**, 219–232.

Tari, G., Molnar, J., & Ashton, P. 2000. salt tectonics in the Atlantic margin of Morocco. *The Leading Edge*, **19(10)**, 1074–1078.

Telford, W.M., Geldart, L.P., & Sheriff, R.E. 1990. *Applied geophysics - Second Edition.* Cambridge University Press.

Theilen, F., & Müller, C. 1999. *Report on Cruise 251/99 of R/V "POSEIDON".* Cruise Report. University of Kiel.

Theilen, F., & Riedel, M. 1997. *Report on Cruise 236/97 of R/V "POSEIDON".* Cruise Report. University of Kiel.

Warner, M. 1990. Absolute reflection coefficients from deep seismic reflections. *Tectonophysics*, **173**, 15–23.

Watts, A.B., & Masson, D.G. 1995. A giant landslide on the north flank of Tenerife, Canary Islands. *J. Geophys. Res.*, **100**, 24487–24498.

Watts, A.B., Peirce, C., Collier, J., & Henstock, T. 1993. *R.R.S. Charles Darwin CD82 cruise report.* Cruise Report.

Weddeling, P. 1996. *Flexure of the lithosphere due to the Canary Islands and its influence on the sediment stratigraphy of the adjacent west Saharan margin.* Ph.D. thesis, University of Kiel, Germany.

Wefer, G., Schulz, H.D., Schott, F., & Hirschleber, H.B. 1992. *Atlantik 91 - Expedition, Reise Nr. 16, 27. März - 8. Juli 1991.* Meteor Berichte. Universität Hamburg.

Wilson, J.T. 1963. A possible origin of the Hawaiian islands. *Can. J. Phys.,* **41**, 863–870.

Wissmann, G. 1979. Cape Bojador Slope, an example for potential pitfalls in seismic interpretation without stratigraphy and implication of outer margin drilling. *Pages 531–539 of:* von Rad, U., & Ryan, W.B.F. (eds), *Init. Rep. Deep Sea Drill. Proj.* Geological Society of America.

Ye, S., Canales, J.P., Rihm, R., Danobeitia, J.J., & Gallart, J. 1999. A crustal transect through the northern and northeastern part of the volcanic edifice of Gran Canaria, Canary Islands. *J. Geodynam.,* **28**, 3–26.

Yilmaz, Ö. 1987. *Seismic data processing.* Society of Exploration Geophysicists, Tulsa, OK.

Zoeppritz, K. 1919. Erdbebenwellen VIIIB, On the reflection and propagation of seismic waves. *Göttinger Nachrichten,* **I**, 66–84.

Acknowledgement

Appendix A

List of abbreviations

AMG	Ateliers Mécaniques de Saint-Gaudens
AVO	amplitude variation with offset
BSR	bottom simulating reflection
CDP	common depthpoint
CMP	common midpoint
COCORP	Consortium for Continental Reflection Profiling
DSV	Digital Sound Velocimeter
HVZ	high-velocity zone
LVZ	low-velocity zone
MCS	multichannel seismic
MORB	mid-ocean ridge basalts
mbsf	meters below seafloor
mbsl	meters below sealevel
NMO	normal moveout
OBH	ocean bottom hydrophone
ODP	Ocean Drilling Program
RMS	root mean square
TWT	two-way traveltime
V.E.	vertical exaggeration
VICAP	Volcanic Island Clastic Apron Project
VSP	vertical seismic profiling

Appendix B
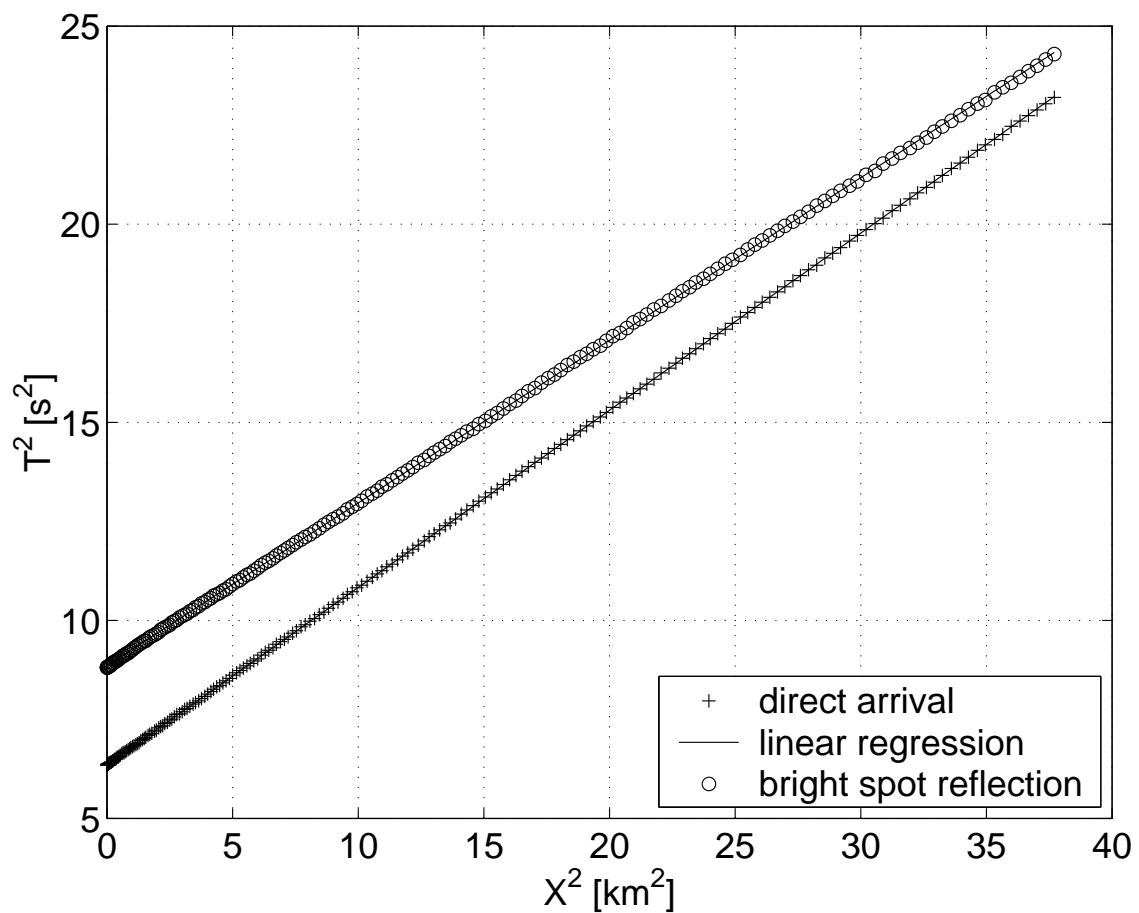
$X^2 - T^2$ velocity model

Figure B.1: T^2 versus X^2 plot for both seafloor and bright spot reflection to determine stacking velocity and reflector depth. Markers are measured data and solid lines are best fit from linear regression.
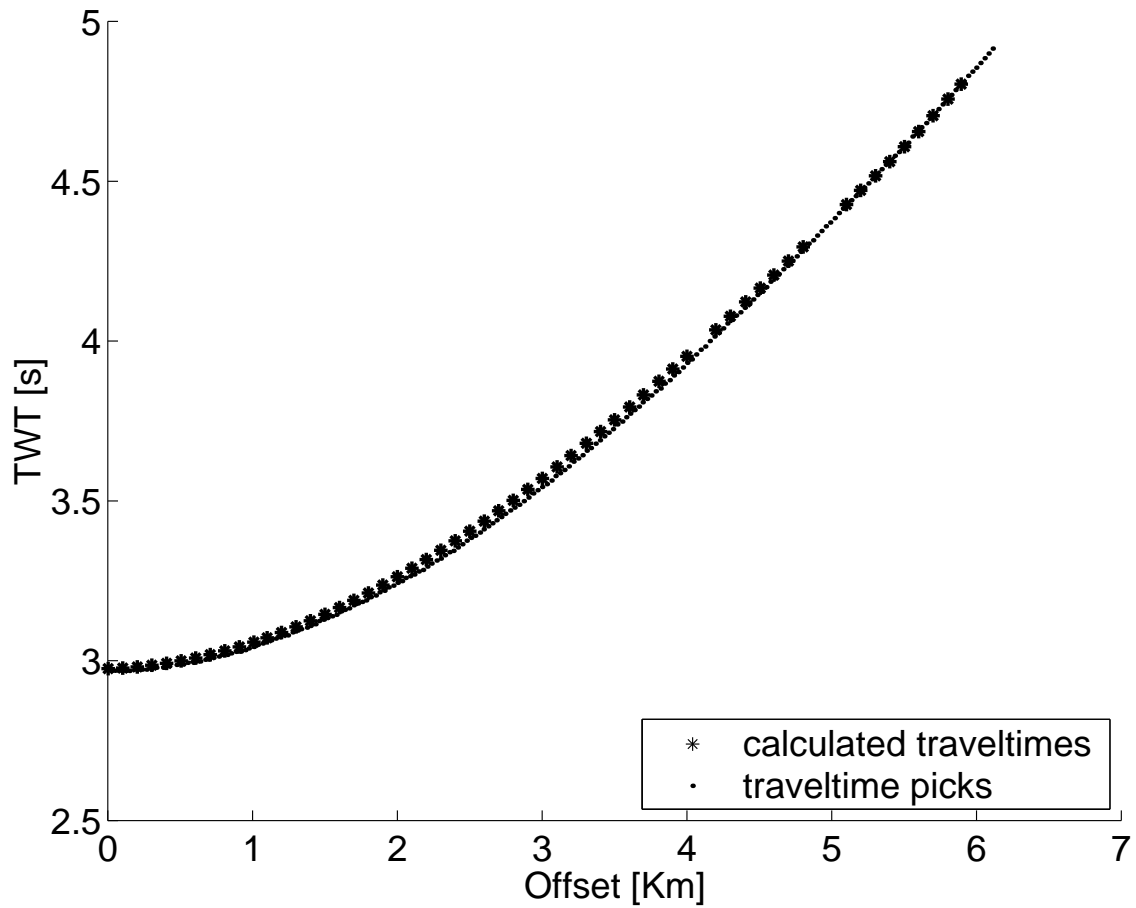
Figure B.2: *Traveltime curve for bright spot reflection in OBH record 03, line14. Calculated traveltimes, based on the velocity model derived from $X^2 - T^2$ method, agree well with observed traveltimes.*

Appendix C

Coefficients of the Shuey approximation

The terms A_0 and B_0 in Shueys (1985) approximation (eq. 4.1) to the Knott and Zoepprit equations are given by:

$$A_0 = B_0 - 2(1 - B_0)\left(\frac{1 - 2\sigma}{1 - \sigma}\right) \qquad (C.1)$$

$$B_0 = \frac{\frac{\Delta V_P}{V_{Pa}}}{\frac{\Delta V_P}{\Delta V_{Pa}} + \frac{\Delta \rho}{\Delta \rho_a}} \qquad (C.2)$$

EIDESSTATTLICHE ERKLÄRUNG

Hiermit erkläre ich an Eides statt, daß die vorliegende Abhandlung, abgesehen von der Beratung durch meine akedemischen Lehrer, nach Inhalt und Form meine eigene Arbeit darstellt und weder ganz noch zum Teil einer anderen Stelle im Rahmen eines Prüfungsverfahrens vorgelegen hat.

_____

Christian Müller

LEBENSLAUF

Name:	Christian Müller
Geboren:	18.01.1972 in Rendsburg
Staatsangehörigkeit:	Deutsch
Familienstand:	Verheiratet mit Kirsten Müller, geb. Ridder
Wohnort:	Bredowstr. 2
	24119 Kronshagen

1978 - 1986:	Grundschule (Ejderskolen, Rendsburg)
1986 - 1988:	Realschule (Hjort-Lorenzen-Skolen, Schleswig)
	Realschulabschluß 1988
1988 - 1991:	Gymnasium (Duborg-Skolen, Flensburg)
	Abitur 1991
1991 - 1992:	Grundwehrdienst (5. Schnellbootgeschwader, Olpenitz)
1992 - 1997:	Geophysikstudium an der Universität Kiel
	Diplomarbeitsthema: "Das Georadarverfahren zur Bestimmung von Wassersalinitaeten und Wassersaettigungen"
	Diplom 1997
seit 1998:	Wissenschaftlicher Angestellter am Institut für Geowissenschaften der Universität Kiel